The Solid Particle Erosion of Polycrystalline Diamond at High and Low Temperatures

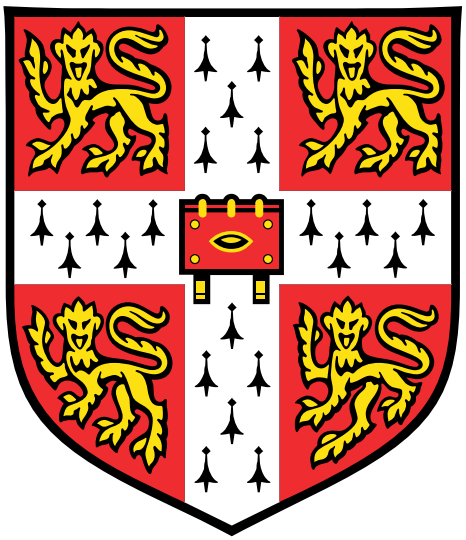

Arthur James Henderson

Department of Physics

University of Cambridge

This dissertation is submitted for the degree of

Doctor of Philosophy

Robinson College

September 2019

Declaration

I hereby declare that this thesis is the result of my own work and includes nothing which is the outcome of work done in collaboration except as declared in the Preface and specified in the text.

It is not substantially the same as any that I have submitted, or, is being concurrently submitted for a degree or diploma or other qualification at the University of Cambridge or any other University or similar institution except as declared in the Preface and specified in the text. I further state that no substantial part of my dissertation has already been submitted, or, is being concurrently submitted for any such degree, diploma or other qualification at the University of Cambridge or any other University or similar institution except as declared in the Preface and specified in the text.

I can confirm that the word limit of 60,000 words set by the Degree Committee for the Faculty of Physics and Chemistry has not been exceeded.

Arthur James Henderson

September 2019

Abstract

The Solid Particle Erosion of Polycrystalline Diamond at High and Low Temperatures

Arthur James Henderson

Polycrystalline diamond (PCD) is formed by sintering together micron sized diamond grits at high temperatures and pressures in the presence of a metal catalyst, usually cobalt. Combining the hardness of diamond with the toughness of a polycrystalline microstructure, a material is produced with properties very suited to drilling applications due to its high abrasion resistance. Throughout the research presented in this thesis, solid particle erosion (SPE) has been used to simulate wear in freestanding PCD discs. The objective was to investigate how PCD responded to SPE over a range of conditions and at both ambient and high temperatures. Experiments were performed on three monomodal grades of PCD with grain sizes ranging from 2 μm to 30 μm. The erosion rates of three erodents, SiO_2, Al_2O_3 and SiC were compared and SiC was chosen as the principle erodent as higher erosion rates could be achieved. The response of erosion rate with velocity was measured for the three PCD grades and, when modelled as a power law, the spread of the exponents indicated that there were different material removal mechanisms taking place as the grain size changed. Increasing the grain size was found to decrease erosion resistance and reducing the cobalt binder content was found to significantly decrease erosion resistance. Erosion at oblique angles demonstrated that the mechanism was purely brittle, and analysis of the eroded surfaces under SEM showed that both microchipping and Hertzian cone cracks could be seen, with cone cracks significantly more prevalent in the finest grain sized material. A set of multimodal PCD compacts were

sintered at a range of temperatures and pressures and their wear rates were tested using SPE. It was found that, over the range studied, increasing the sintering pressure and decreasing the sintering temperature both increased wear resistance. The effects of temperature on the wear of PCD are highly relevant due to the frictional heating that can occur during drilling. The effect of thermal history was studied by eroding PCD discs at ambient temperature after a range of vacuum heat treatments at temperatures up to 800 °C. A further test was performed comparing the effects of heat treatment in air to those in vacuum at 700 °C, finding much more severe surface degradation when the treatment was performed in air. A description of how the SPE apparatus has been adapted to allow erosion with high temperatures (up to 650 °C) in-situ is given, together with the results obtained using the apparatus. It was found that the erosion rate for all grades initially decreases with temperature, down to a minimum at around 200 °C, before increasing again at between 450 °C to 500 °C, or higher for PCD with a reduced binder phase. A further test was performed to help understand the reasons for the change in erosion rate with temperature by eroding samples that had previously been eroded at high temperatures, at ambient temperature. A modification was made to the high temperature SPE apparatus to allow erosion at temperatures below ambient temperature by cooling using liquid nitrogen. To the best of the author's knowledge, low temperature erosion has never before been performed in this way, and the response of PCD to erosion at temperatures down to −100 °C was measured. The research yields insight into the response of PCD with temperature taking care to distinguish those thermal effects that alter the surface at temperatures above 450 °C to those that alter the bulk microstructure above 700 °C. Eroded surface fractography demonstrates the mechanisms for material removal during erosion and helps to explain the changes in erosion rates as the conditions are varied.

Acknowledgements

The research presented in this thesis was performed in the Surfaces, Microstructure and Fracture (SMF) group of the Cavendish Laboratory, University of Cambridge, between October 2015 and September 2019, under the supervision of Dr Andrew Jardine. I would like to thank Dr. Jardine for his support and supervision throughout my time as a postgraduate student at the Cavendish.

I am exceptionally grateful to Drs. Jim Pickles & Richard Bodkin of Element Six, as well as the entire Element Six road planing team. I would like to thank Element Six for supporting the research presented here financially. Jim was responsible for creating the project and Richard supervised and guided my efforts in a direction that might be useful to those who use PCD beyond just the laboratory.

Dr. David Williamson was instrumental in introducing me to the SMF group and in convincing me to stay for four more years, for which I am very grateful. He also provided the initial inspiration for the cold erosion experiments, and invaluable expertise towards the execution of the experiments themselves.

A small set of experiments were performed at the National Physical Laboratory, for which I would like to thank Dr. Mark Gee for the opportunity and Tony Fry for looking after me during my visit.

I would like to thank all of my fellow members of the SMF group for making me feel welcome during my time here: Drs. Chris Braithwaite, Nick Taylor, Stephen Walley, Lewis Lea and James Perry; and Sue Gymer, Neil Hamilton, Sara French, Sarah Ward, Ryan Potter,

James Edgeley, Thomas Cowie, Olivia Morley, Mike O'Donnell and Matthew Maisey. A particular mention must be made to those in the 'top office', where all of the ups and downs of postgraduate study were shared.

I would like to thank the staff of the Cavendish for their support during my research, especially those in the workshops who manufactured various apparatus and taught me skills that I will retain well beyond my time here.

Outside of the lab, I would like to thank those with whom I spent most of my time for keeping me both sane and entertained, including the ever supportive housemate Chris Valentine, the Cambridge Sailing Team past and present, and the CUBS.

Finally, I am grateful to my family for their continuous support. I would like to thank my parents for always encouraging me to pursue that which interests me the most, for always being on the end of the phone, and for sounding enthusiastic when I discussed the latest developments in the lab.

Table of contents

Chapter 1

Introduction

Polycrystalline diamond (PCD) is one of a class of 'superhard' materials widely employed for their high abrasion resistance. It is formed by sintering together micron sized diamond grits at high temperatures and pressures in the presence of a metal catalyst, or binder, usually cobalt [1], to form a continuous network of randomly orientated diamond grains connected by diamond bridges. Combining the hardness of diamond with the toughness of a polycrystalline microstructure, a material is produced with properties highly suited to abrasive drilling applications [2, 3].

Diamond was first synthesized in a controlled manner in 1955 by researchers at General Electric [4]. Although it immediately found an application as a loose abrasive, just as natural diamond had before it, the use of single crystal diamond for machining and drilling is limited by the highly brittle nature of the material, as, due to the lack of energy absorption mechanisms such as dislocation motion, it can fracture in tension under relatively small forces. In 1970, diamond grains were combined in a high pressure and high temperature environment for the first time to form a polycrystalline material [5, 6]. Since then, PCD has been manufactured for uses in drilling in the form of a thin 1 mm to 2 mm layer on top of a tungsten carbide-cobalt (WC-Co) substrate, known as a polycrystalline diamond compact (PDC), an example of which is pictured in fig. 1.1. PDCs have, since their invention,

come to replace WC-Co ‘roller cone’ bits as the most common material used in oil and gas exploration drilling [7].

Fig. 1.1 An Element Six PCD compact. The 2 mm thick black PCD layer is integrally sintered to a tungsten carbide substrate. A range of diameters are available up to 70 mm, although 10 mm to 16 mm is standard for drilling applications.

During cutting and machining using PCD tools, frictional heating causes the wear face to experience high temperatures. However, PCD is susceptible to intense thermal degradation due to the presence within the microstructure of the cobalt binding catalyst. The catalyst is introduced to reduce the pressures and temperatures required to sinter PCD. However, although carbon can dissolve in it to facilitate the conversion between the sp^2 and sp^3 states during manufacture, the catalyst can also catalyse the sp^3 to sp^2 transition at high temperatures in application [8]. This ‘graphitization’ rapidly reduces the effectiveness of the drill bit as diamond is converted to the less hard graphitic form. Cobalt also has a significantly larger thermal expansion coefficient than diamond, so internal stresses are changed on heating of the compact [9], which can lead to an increased probability of fracture. It is possible to reduce the content of the binder phase by a process which is commercially sensitive. The resultant material is known as reduced binder phase PCD (RBPCD).

It is difficult to apply standard wear tests to PCD due to its high abrasion resistance. For example, a simple pin on disc test produced no wear flat or measurable loss of material when PCD was tested [10]. Fracture tests are possible, although care must be taken to ensure that

the correct property is measured as the sample grips or holder will inevitably be less hard than the sample. Thus, the initial reaction of the system may be the response of the sample holder plastically deforming at the contact points, as opposed to the reaction of the PCD itself to the stimulus, and so the two must be decoupled. A disadvantage of fracture tests is their stochastic nature, and hence the requirement to test a large number of samples to produce a reliable result, which is less desirable when working with a material that can be difficult and expensive to produce, such as PCD. There is also not necessarily a correlation between fracture and wear, and occasionally the opposite is true whereby increasing the resistance to one may increase susceptibility to the other [11].

During the research presented here, solid particle erosion (SPE) has been used to simulate wear. SPE is a method of damaging a surface by repeated impact of abrasive particles. Initially used to test wear of components in relation to moving sand (either wind-driven sand, or jet planes moving through sandstorms) [12], erosion has now become a standard wear test available to researchers when investigating materials. A major advantage that SPE has over other tests is the ability to produce controlled but measurable amounts of wear in highly wear resistant brittle materials without requiring large quantities of substrate to wear against or running into the hazard of complete fracture of a sample. Erosion can also return a wear rate from a single sample with a low error, as the damage from over 10^5 small impacts is integrated together during the measurement.

Motivation

New uses for PCD are being researched to exploit its extreme properties in areas ranging from biomedical devices [13] to sensor applications [14]. The largest use of PCD by some margin remains in tooling.

Frictional heating during drilling causes the wear face to increase in temperature and may change the wear mechanisms present. Chemical changes on the surface or in the bulk of the

tool can affect the mechanical properties, however to what extent the response of the material changes with temperature is not well understood. To date, the majority of studies performed on the thermomechanical properties of PCD either study macroscopic fractures, or study the response in unrealistic environments, such as in a vacuum. An improved understanding of the temperature response of PCD can help manufacturers design and build more hard wearing or thermally resistant tools, and help operators of machinery that uses PCD tooling to better understand the limitations of their equipment.

An example of one of the novel ways to take advantage of the very low wear rate of PCD is in the process for removing the the top layer of asphalt on roads, known as road planing. The currently preferred method of road planing involves mounting a number of WC-Co picks on a large cylindrical drum, which rotates at high speed and mills away the asphalt. Fig. 1.2 shows an example of a road milling pick in the standard shape, but with a PCD tip at the cutting edge, which has been designed to replace the current WC-Co picks. A better understanding of the processes that occur during the wear of PCD will enable new picks to be designed with improved lifetimes. The consequences for the operator would include a reduction in the downtime needed to replace individual picks, and the added downstream advantage of a more consistently milled road surface.

However, testing a large quantity of PCD samples in the field is simply not practicable for a number of reasons. The conditions in the field are not repeatable, road surfaces can contain varying constituents and can exhibit a range of hardnesses depending on the ambient temperature. The incredibly low wear rate of PCD would require excessively lengthy tests, which would be costly and necessitate the use of specialist road milling equipment. As previously discussed, knowledge about the precise temperature at which the wear of PCD is accelerated due to chemical changes is desired, but is difficult to measure in application. Any thermocouple at the wear face would be immediately abraded away, but any distance between

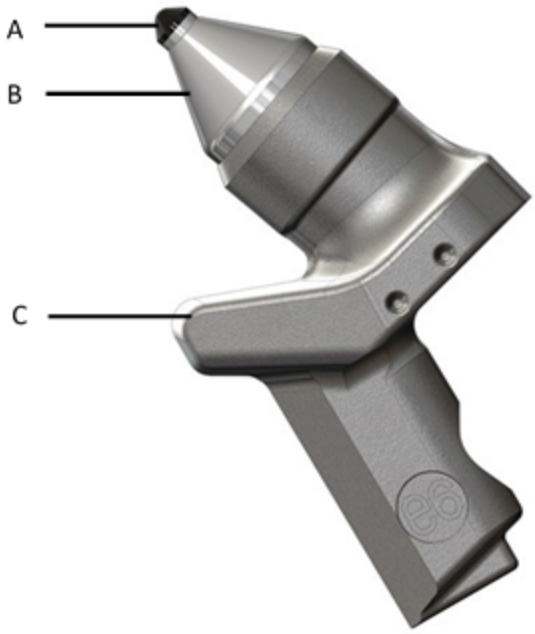

Fig. 1.2 An Element Six road milling pick. A rounded PCD layer (A) has been sintered to a WC-Co base (B) which is brazed onto a steel holder (C).

the wear face and a thermocouple would increase the error in the measured temperature, and decrease the integrity of the PCD bit.

Although SPE is not the wear test most similar to the road planing application, which would focus more significantly on abrasion over erosion, it has been chosen to simulate wear as it is the best suited to gain the maximum information about PCD with the resources available. The repeatability of SPE enables accurate results using a limited number of samples. The wear rates achieved by erosion are high enough to be accurately measurable using a reasonable quantity of erodent on a reasonable timescale. High temperature erosion provides reliable and accurate data for the temperatures at which wear is accelerated due to chemical processes. A further discussion of the suitability of SPE for simulating wear including some of the limitations is presented in Section 3.2.7.

Continuous incremental improvement of tooling and diversification of markets is commercially desirable, and research including this project is often sponsored by those wishing to explore this route, however PCD is itself an interesting system worthy of study. It contains

a biphasal microstructure which can be modified before, during and after manufacture in a large number of ways, and is an extreme material with properties that no others can match. Research into PCD seeks to create materials with unique combinations of hardness and toughness which no other known material could obtain.

Research Objectives

The aim of this research is to improve the understanding of the response of PCD to various mechanical and thermal stimuli by subjecting PCD to SPE under a range of conditions. The wear rates and mechanisms will be studied and the different erosion regimes will be compared. While ultimately the goal is to prolong the lifetime of PCD drill bits and road picks in the field, the focus will be on the material and its response, rather than tuning tests to be similar to any potential applications.

The temperatures reached during drilling are up to 700 °C, above which it is known that PCD decomposes and becomes near-useless as an abrasive [8]. A PCD compact can also undergo a heat cycle during brazing to a tool component, the temperature of which can, for short times, reach above 700 °C. Although a number of tests will be performed at room temperature as it is easiest to demonstrate the material response in ambient conditions, the aim will be to understand how heat treatments (varying time, temperature and atmosphere) affect the properties of PCD, and to perform erosion tests with high temperatures in-situ.

During the course of the research, it was found that the apparatus for performing erosion at high temperatures could be modified to test at lower than ambient temperatures. Cryogenic drilling is a technique practised in certain applications [15], and the material response of PCD below 0 °C is under-documented. Once this opportunity became available, a new objective became to perform a set of experiments at temperatures lower than ambient as a way to both demonstrate a novel technique, cold erosion, and to further understand the response of PCD in a less well understood region.

The factors that are thought to affect the wear rate of PCD include the sintering temperature, pressure and time, the consistency, quantity and structure of the binding phase that remains in the material, the diamond grain size distribution and the macroscopic surface stress state arising from the backing substrate. The goal here is not to measure the consequences of altering the complete range of all of these parameters, as that, combined with the variables that can be altered during an erosion test, would take so long as to be infeasible, so the experiments with one exception focus on just three standard research grades of PCD and on varying parameters in isolation.

Thesis Overview

To summarise, PCD has a unique combination of hardness and toughness which make it suitable for abrasive drilling applications where low wear rates are desired. Improved wear rates are of commercial interest as PCD tools will become more economical and be able to replace conventional drilling materials in previously unconsidered applications.

Chapter 2 presents a detailed look at the manufacture and properties of PCD. The manufacture process of PCD gives some insight into the reasons why it has such extreme wear resistance. Then, a summary of the literature on PCD is given, including typical wear mechanisms and its response to high temperatures.

In Chapter 3, an introduction to brittle fracture is outlined. There is a discussion of how these fractures combine under the repeated impacts experienced during erosion to cause material removal. An overview of the ongoing research of SPE of diamond and the very small amount of prior erosion of PCD is given. The apparatus used to perform SPE is described along with the methods for calibrating it, and the details of erodents that were used during the project.

Chapter 4 contains a number of erosion tests and studies of how various erosion parameters affect erosion rates. A detailed SEM study of the damaged surfaces was performed which

aimed to give an understanding into how material is removed from PCD during the erosion process. From this, a mass loss mechanism is suggested which explains how the trends in erosion rates across different conditions occur.

In Chapter 5, the erosion conditions are now held constant, and the response of PCD to different preparation methods under equivalent conditions is studied. The effects of sintering temperature and pressure are tested, followed by a study of how the erosion rate of PCD changes when samples have undergone a prior heat treatment. This latter test is the first look at the effects of temperature on microstructure, and then how it affects wear, and both treatments in vacuum and in air are considered.

Next, the focus moves on to performing erosion at high temperatures. The apparatus used to enable high temperature SPE and its calibration procedures are described in Chapter 6, followed by the results obtained in Chapter 7. A secondary test was performed where the samples were re-eroded at room temperature after they had undergone hot erosion to give further insight into how the mass loss mechanism changes with temperature.

Chapter 8 contains the final experiment which was performed on PCD at temperatures below ambient. The desire to erode at low temperatures came from the knowledge that cold erosion had not been performed previously and from comparison to the high temperature results presented in the previous chapter.

Finally, Chapter 9 collects the results of the thesis together and combines them to give an overview of how the SPE of PCD has helped understand the thermomechanical wear processes present under the conditions studied. The conclusions are summarised and potential openings for future research are discussed.

Chapter 2

An Introduction to Polycrystalline Diamond

Due to the use of PCD as an industrial abrasive, there has been a large quantity of research undertaken in order to optimise its properties. A survey of the scientific literature has been performed and those parts most relevant to the research performed in later chapters are presented here. The chapter will be divided into 4 sections covering:

1. The properties of diamond and how the microstructure of diamond can be manipulated in high pressure high temperature environments.

2. The manufacture of PCD from diamond grains. The microstructure and unique properties of PCD are a consequence of the non-trivial manufacture process which is explained. The possible post-processing options including the reduction of the binder phase are discussed.

3. The mechanical and thermal properties of PCD. A survey of the tests that researchers have performed on PCD yields an indication of the properties under wear and fracture conditions at a range of temperatures.

4. The particular PCD grades that will be tested during this research and the specific sample preparation that has been performed on them. A description of the samples tested in this thesis is important if the results presented in later chapters are to be compared to any further experiments performed at a later date.

2.1 The properties of Diamond

Before discussing the physical properties of PCD, it is important to understand the properties of single crystal diamond as it is the primary material from which PCD is made. Diamond is a lattice of sp^3 bonded carbon atoms in a tetrahedral shape, generally with a face centered cubic unit cell [16]. It is the stable form of carbon only at high pressures [17]. However, due to the large activation energy required to transition between diamond and the sp^2 bonded carbon in graphite, diamond is metastable at room temperature and pressure.

Diamond types are classified by their crystal structure (cubic or hexagonal) and then by the quantity and composition of the impurities contained within the structure. The presence of defects gives colour to diamond: yellow diamonds contain nitrogen; pink ones contain dislocations; green contain nitrogen-vacancy-nitrogen centres; blue contain boron and brown diamonds are natural diamonds which were originally another colour [18, 19]. PCD is manufactured from synthetic cubic type 1b diamond, so called due to its high nitrogen content (greater than 1 ppm) primarily in single substitutional sites [20], as it is the easiest to produce in significant quantities. The diamond is made by introducing graphite flakes and diamond seed crystals into a high temperature high pressure apparatus, a schematic of which is given in fig. 2.1. In the diamond stable region of the phase diagram shown in fig. 2.2, sp^2 graphite dissolves into the molten metal catalyst and re-precipitates out on the surface of the seed crystals as sp^3 diamond. The limitation on the size of the diamonds that can be produced by this HPHT method is the volume that can be held at the required conditions, and the slow growth rate at large crystal sizes. Controlled growth of large single crystals is

difficult as precise thermal gradients are hard to maintain over long timescales at the high temperatures and pressures required for diamond sintering.

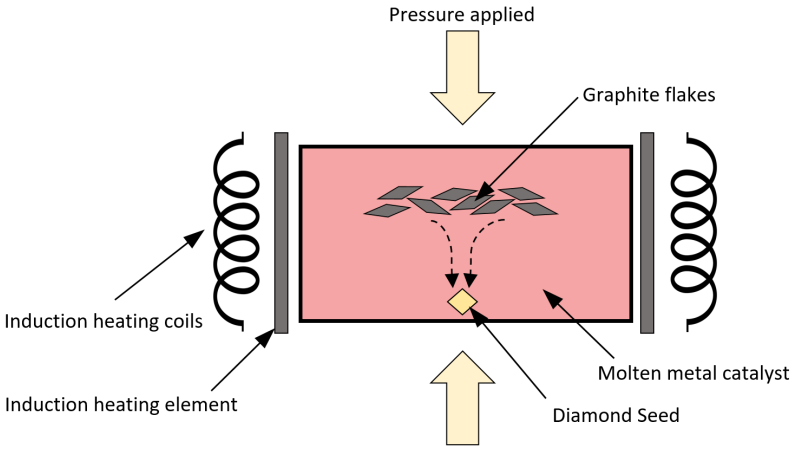

Fig. 2.1 A schematic for the manufacture of small diamonds from graphite under high pressures and temperatures. The pressure is contained laterally by a sequence of pre-loaded steel belts. A seed crystal is required as spontaneous nucleation of diamond has a high energy barrier.

The origin of the extreme properties of diamond is the rigidity of the lattice [16]. The short (0.154 nm [23]) and stiff covalent bonds and the tetrahedral structure creates this rigidity, with the result that single crystal diamond lies at the extreme end of the scale of many material properties, although the properties can be highly anisotropic. Quoted Poisson's ratios vary from 0.05 to 0.3 [24], diamond has the highest Young's Modulus of any bulk material (an isotropic aggregate of 1050 GPa) [25, 26] and a very high elastic wave speed (11.6 $\mathrm{km\,s^{-1}}$ to 17.5 $\mathrm{km\,s^{-1}}$) [24]. It also has a high thermal conductivity (up to 2000 $\mathrm{W\,m^{-1}\,K^{-1}}$ [27]) which is useful in abrasive applications as it helps to transfer the thermal energy generated by friction away from the cutting edge quickly, resulting in a lower cutting face temperatures and reduced chances of thermal degradation.

Due to the high anisotropy, fractures tend to propagate on the preferred (111) cleavage planes [18, 28] even though cleaving along the (111) plane requires only about 10% less energy than other nearby planes, e.g. (332) [28, 29]. It is thought that the dominance of the

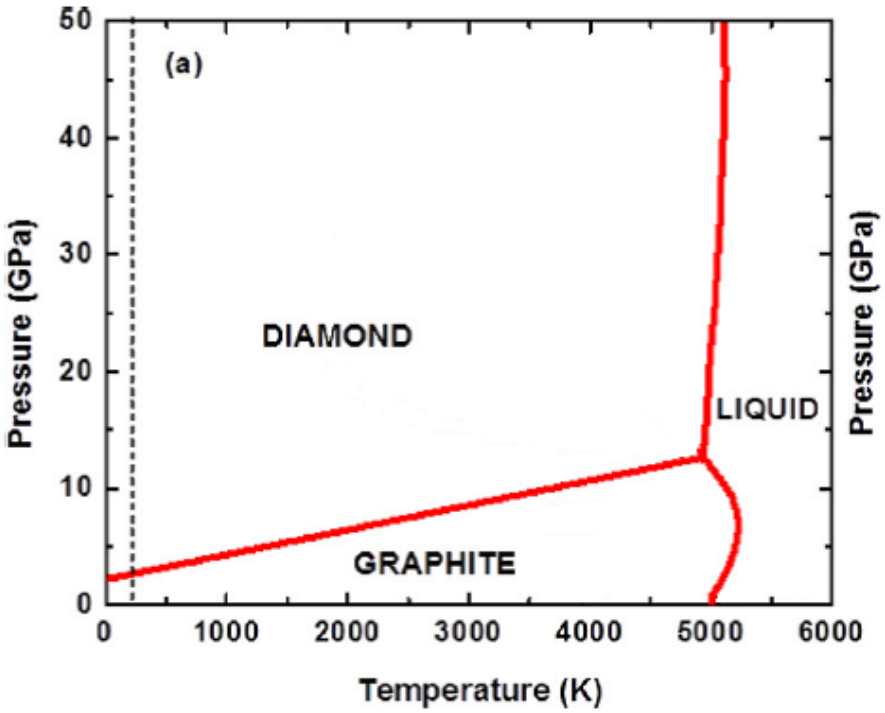

Fig. 2.2 A 2015 phase diagram for carbon adapted from [21, 22]. The solid line between the graphite and diamond phases is the Berman-Simon line [17], bounding the region for diamond stability if there were no energy barrier between the phases.

(111) plane is due to the ability of the crystal to stretch away from the <111> direction due to less restrictive bond bending [28].

At elevated temperatures, diamond becomes increasingly ductile with a brittle-ductile transition temperature between 750 °C to 850 °C depending on the nitrogen content and the applied strain rate [30]. As these temperatures are above the expected temperature range of any mechanical tests that will be performed during this research, it can be assumed that the diamond within PCD will fracture in a brittle fashion.

2.2 The Manufacture of PCD

2.2.1 The High Pressure High Temperature Process

Understanding the manufacturing process for PCD is important to explain the origin of the microstructure and the subsequent properties of PCD. Adjusting the source material and sintering conditions can have a downstream affect on the wear behaviour of PCD by affecting the microstructure.

The microdiamonds produced as described in the previous section are crushed and separated by size. The grain size distribution of the PCD is then selected by choosing which size diamond feed particles are used. Their size can range from 2 µm to 150 µm [16]. PCDs can be monomodal, with the initial diamonds all of the same size, or more commonly in application they are multimodal, with a distribution of grain sizes. In multimodal PCDs, the smaller grains can fill in the gaps between the larger grains and, due to the higher packing density, increase the proportion of the resulting PCD that is diamond. Multi layered PCDs are possible, with regions of fine grains and separate regions of coarser grains where desired [31].

The seed diamonds are then placed below a tungsten carbide cylinder containing a cobalt binder, as in fig. 2.3(a), and the entire assembly is compressed to a pressure of around 5 GPa or higher. Initially the diamond grains slide past each other and rotate. As the pressure is increased further, the pressures at the contact points between the grains become very high and

the particles are crushed. The initial particle size distribution is modified, creating smaller micron and sub-micron sized particles [32].

Next, the temperature is increased following the path shown on the phase diagram in fig. 2.4. Above 750 °C, the type 1b diamond goes through the brittle-ductile transition temperature and dislocations become mobile [30]. The point contacts between the diamonds become enlarged and flattened as the individual diamond particles become highly plastically deformed, as in fig. 2.3(b). A series of hot indentation experiments by Brookes *et al* [33] showed that deformation occurs throughout the entirety of the grains on a scale much larger than the contact points. Confirmation of this plastic deformation is given by Yu *et al* [34]. As such, the grains of diamond contain, in comparison to the typically dislocation free single crystals, a high density of interlocking dislocations and could be described as 'work hardened'.

As the temperature reaches around 1321 °C, the cobalt in the adjacent WC-Co binder melts (fig. 2.3(c)). The immediate layer of diamond at the WC/diamond interface dissolves into the cobalt which then seeps into the diamond layer. Now, the conditions for diamond sintering are present and carbon atoms are able to diffuse through the cobalt catalyst. Carbon atoms can dissolve into and recrystallize out of the cobalt as new diamond bridges, in between the larger grains [35]. The driving forces for this recrystallization include: higher surface energy to volume finer particles dissolving and larger grains growing; sharp edges and steps dissolving and perfect faces growing; highly plastically deformed crystals dissolving and perfect crystal structures precipitating; non-diamond carbon dissolving and diamond precipitating; and the existence of pressure and temperature gradients in the press leading to areas which favour diamond dissolving or growing [32].

The pressure and temperature is held until the diamond bridges have formed. On cooling through the cobalt/carbon eutectic point at 1321 °C, the cobalt freezes and the microstructure becomes set. Macroscopically however, there is a difference between the thermal expansion

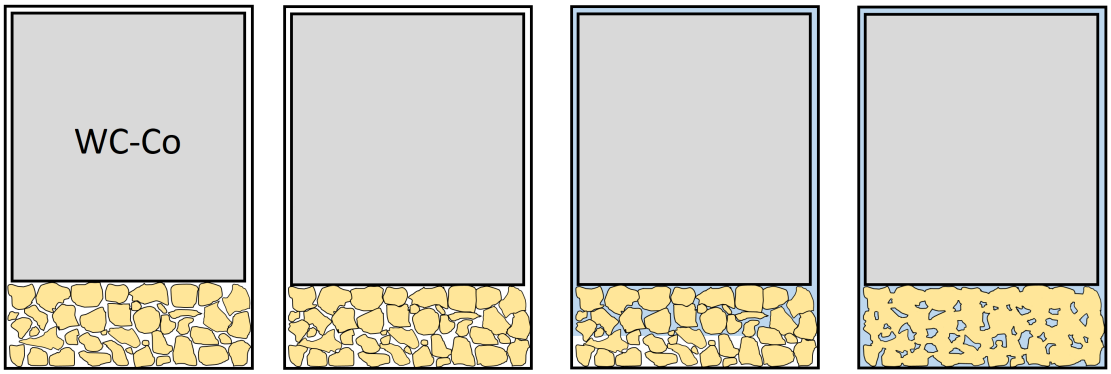

Fig. 2.3 The manufacture process for PCD. In step (a), the diamond grains are placed underneath a WC-Co cylinder and crushed. As the temperature is increased in (b), the diamond becomes ductile and dislocations pass through the grains. Point contacts become flat faces. On a further temperature increase (c), the cobalt melts and passes through the diamond grains, catalysing the sintering process and forming PCD (d).

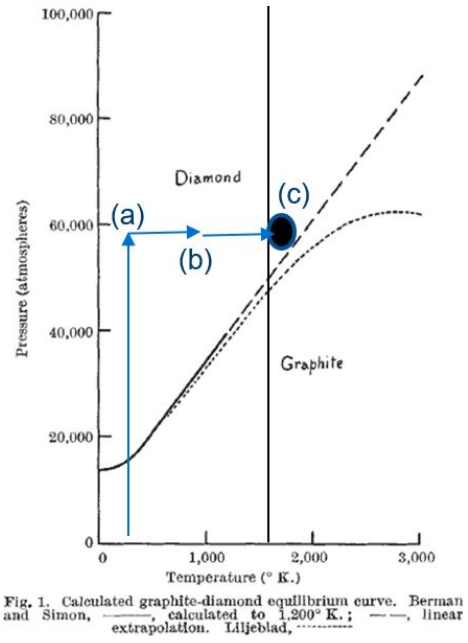

Fig. 2.4 A carbon phase diagram from Berman & Simon [17] showing the path through phase space that the diamond takes during the stages of manufacture pictured in fig. 2.3. The cobalt melt line at 1321 °C is shown with the simplifying assumption that it is pressure-independent.

coefficients and Young's moduli of PCD and WC. As the pressure is removed, the lower Young's modulus of WC means that the WC will expand a larger amount than the PCD. Conversely, on cooling the coefficient of thermal expansion of PCD is lower than that of WC, so the WC contracts more than the PCD. The larger of these two effects is the thermal contraction, and so the macroscopic shape of the PCD compact results in the PCD layer under radial compression and the WC under radial tension. The residual stresses can be altered by changing the interface shape as will be discussed in Section 2.2.4.

The resulting microstructure, viewed under optical and electron microscopy, can be seen from the images of a polished section of PCD in fig. 2.5. The large diamond grains are clearly evident and the majority of them are the same size as the initial diamond feed. Between the large areas of diamond, the bridges between the grains are visible although some of them contain entrapped cobalt. Smaller regions of diamond, much smaller than the grain size, are present which could be either small grains fractured during sintering or diamond bridges. By weight, roughly 90% of the microstructure is diamond and 10% is cobalt. It cannot be discerned from these images but it has been previously shown (e.g. Liu *et al* [36]) that the majority of the cobalt pools are interconnected, such that most of the cobalt lies within one continuous network which interlocks the diamond skeleton.

2.2.2 Defects

The properties of the diamond within the grains is fundamentally different to the diamond in the bridges between them, and to pure single crystal diamonds, which will be shown to be relevant to the fracture properties of PCD. The diamond in the grains has been deformed at a temperature higher than its brittle-ductile transition temperature and so has been work hardened throughout [33]. The crystal structure has a high density of both defects and dislocations making it tougher than single crystal diamond, as there are an increased number of energy barriers due to obstacles that a propagating fracture must overcome. Contrastingly, the diamond in the bridges between the grains has been precipitated out from the binder

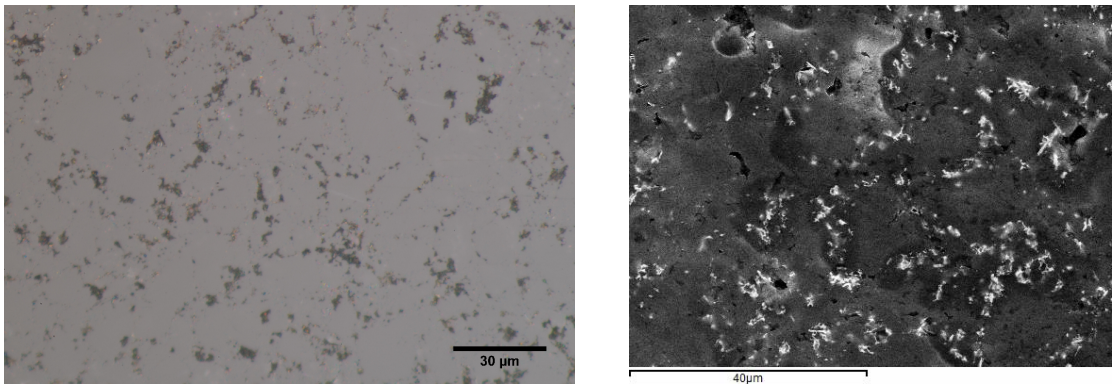

(a) Optical Microscope (b) Backscattered SEM

Fig. 2.5 Images of the polished surface of a monomodal grade of PCD with an initial grain size of 30 µm. The contrast between the cobalt and the diamond is inverted between the images and the greater interaction area of the electrons compared to photons reveals a larger proportion of the surface cobalt than the optical image.

phase in the press, and so is expected to have a lower density of dislocations but in order to account for the mismatch in crystal orientation between the grains must contain a number of twinning planes.

2.2.3 Reduction of the Binder Phase

A proportion of the cobalt binder within the microstructure can be removed from a PCD tool by a post-manufacture process [37]. The front face of the tool is exposed to a highly concentrated acid which is heated to near its boiling point [38]. The metal binder dissolves in the acid leaving a network of pores between the diamond grains. The process is time consuming and expensive, taking of the order of days to complete [38]. Some pools of binder will be disconnected from the binder network and thus will remain after the process, but this effect is thought to be small [36].

The resultant RBPCD is expected to have improved wear resistance at high temperature for two reasons. Firstly, the catalyst for the sp^3 to sp^2 transition in carbon is no longer present, reducing graphitization. Secondly, removing the cobalt has the added benefit of increasing the thermal conductivity of the PCD [9], which helps to draw heat away from the work face, reducing the maximum temperature attained and so reducing thermally induced damage.

It is also possible to create PCD compacts with alternative binders, or with no binding phase at all. The latter are known as thermally stable polycrystallines (TSPs) for their increased thermal resistance [39], however they require extreme pressures and temperatures to form, making them expensive. Their applications are typically restricted to specialist roles such as semiconductor heat sinks [9].

2.2.4 Surface Stress State

The residual stresses present in a PCD compact can be altered by changing the shape of the interface between the PCD and the WC-Co. Generally, compressive stresses are preferred near a cutting edge in order to increase the energy barrier for crack nucleation and propagation, prolonging the lifetime of a tool bit. A number of different values are reported for the maximum compressive stress on the surface of a sample and they are highly dependent on the location on the sample and the method of preparation. For example, a 1.3 GPa compressive stress has been reported by Catledge *et al* [40] for a curved PCD layer with a rounded interface, whereas Mcnamara *et al* found that a flat PCD disc that had been removed from its substrate contained up to 1.2 GPa of tensile stress [41].

The size of residual stresses can be measured by measuring the shift in the Raman peak as the length of the carbon-carbon bond responds to the external forces [42]. As the effect on the peak shift is typically small, the stresses measured can have high errors and so although studies using Raman can be relied on for overall trends, a high weighting should not be placed on single readings.

Numerical predictions by Kanyanta *et al* [43] found that the maximum tensile stresses present after sintering using a flat cylindrical geometry were 500 MPa, whereas the maximum compressive stresses were 150 MPa. They also advise that specific sintering pressures and temperatures can be used, combined with longer cooling times in order to prevent high stress transients which can be up to 3 times larger than the residual stresses.

McNamara *et al* [41] studied the effects of quenching samples in oil from 600 °C to room temperature on their residual stresses. The authors found by measuring the location of the Raman peak that there could be very large discrepancies in local stress state. A difference of 2 GPa was found between two adjacent sites 2 mm apart. They found that, due to its high coefficient of thermal expansion, the cobalt binder shrunk more during the post-sintering cooling down to room temperature than the diamond skeleton, leaving the binder under tension and the diamond network under compression. Reducing the content of the cobalt binder reduces these residual stresses, increasing tension and decreasing compressive stresses throughout the sample. The effect was more pronounced in the coarse grained microstructure as a larger proportion of the cobalt could be removed due to the lower likelihood of closed pores on sintering. Further, the authors also found that the residual stresses were more likely to be compressive in the centre of the PCD, and tensile near the edges. A quench from 600 °C tended to increase tensile stresses, which are not desirable in a final product and correlates well with the desired cooling curve found by Kanyanta [44] to minimize residual stresses.

Feng Chen *et al* [45] modelled the system and found that the highest residual stresses are to be found at the interface between the PCD and WC-Co layers which is demonstrated in fig. 2.6, which can help to explain why macroscopic cracks can be found to propagate away from here during milling tests [46].

Focusing on how the residual stresses can affect wear rates, Fan *et al* [47] directly measured the effect of changing the WC-Co/PCD interface during a comparative abrasion test. Surveying a range of interface structures, the authors found that an undulating interface with a recessed ring - so that the PCD envelops the center of the interface with WC-Co, lost the least mass during the abrasion test. However, only a very small amount of mass was lost (0.11 mg), which resulted in a correspondingly high error and does not reveal how PCD would respond after significantly more wear.

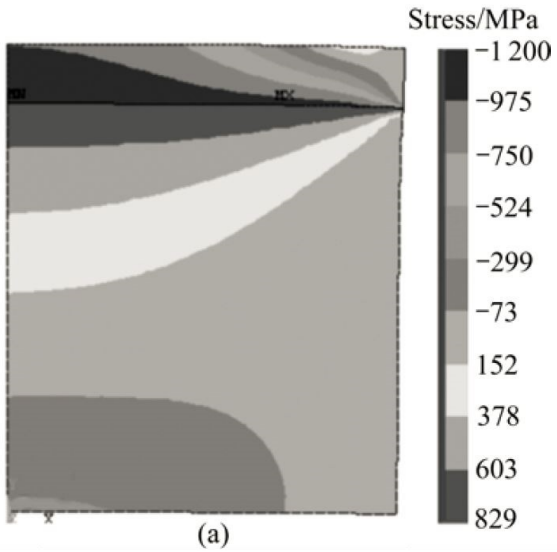

Fig. 2.6 Radial stress distribution in a PCD compact, from [45]. The centre of the compact is on the left of the image, with the outside edge to the right. The thin PCD layer which is under compression is on top, with the larger WC-Co under tension underneath.

Krawitz *et al* [48] measured the residual stresses using the more accurate method of neutron diffraction and found values of up to 500 MPa of compressive stress, primarily hoop stress, in cylindrical PCD compacts. Compressive stress decreased as the substrate to table thickness ratio decreased towards 1, which is not unexpected given the decreased volume of WC-Co. Pagget *et al* took this work further [49], and showed that the sintering processes could be manipulated to positively alter the residual stresses in a PCD compact.

A large quantity of research has been performed studying the residual stresses of PCD compacts, which is indicative of the opportunities to improve the performance of PCD tools. When designing experiments to be performed later in this thesis, or when comparing the results of any mechanical testing between authors, the consequences of sample manufacture and residual stresses must be taken into account. There are very many different ways to change the PCD/WC-Co interface and it is an active area of research for many PCD producing companies due to the potential for improving tool performance.

2.2.5 Summary

The PCD manufacture process creates a network of randomly orientated, work hardened grains connected by relatively dislocation-free diamond bridges. Twin planes exist within the bridges to account for the mismatch in crystal orientations. There are separate binder pools containing high carbon cobalt, most of which are connected to each other. The cobalt is "locked in" to the high temperature f.c.c. phase during cooling [40] despite the h.c.p. phase being more energetically favourable below temperatures of 422 °C [35].

Grades of PCD can differ by initial diamond grain size and shape distribution, the conditions sintered under, the type and content of the binding phase, the local stress state due to the macroscopic sintering environment and geometry, and the thermal history of the sample. Properties can be selected to suit the application, and a discussion of how these factors affect mechanical and thermal properties is presented in the next Section.

2.3 Mechanical and Thermal properties of PCD

The properties of PCD are most often tested at ambient temperature, and so by far the majority of studies investigate the mechanical properties without accounting for the effects of temperature. Here, we are interested in the properties over a range of temperatures, but due to the rarity of temperature-dependent studies the review will be separated into two sections: The ambient temperature mechanical properties; and how temperature affects these mechanical properties.

2.3.1 Mechanical Properties and Fracture

The mechanical properties of PCD can be measured by a variety of methods typical for brittle materials, such as ball on disc and three/four point bend tests, however the high hardness of PCD and its low wear rates can make these experimentally challenging to perform. To help provide an understanding of the response of PCD, it is important to observe in detail

the microscopic changes that occur, for which SEM imaging is the most useful tool. Images allow researchers the focus in on the nucleation and propagation of cracks by identifying their relative locations within the microstructure. The limited size that PCD samples can be manufactured to, and the difficulty in machining samples due to its high hardness, means that standard approaches must often be adapted to enable reliable testing [50]. Less hard materials are likely to plastically deform if in point contact with PCD and so the geometry of the experiment and the measured stresses or strains may be altered and not be indicative of the true stresses or strains present, so extra care is required when performing experiments. Here, the focus will be on both understanding fracture in PCD, and understanding the wear process under a range of conditions.

Brittle Fracture in PCD

The origin of the theory of brittle fracture was Griffith's energy balance criterion [51] established in the early 1920s. Assuming a crack to be in equilibrium, the critical stress for failure, σ_F, is found by making equal the stored elastic energy and the energy required for the generation of two new fracture surfaces,

$$\sigma_F = \sqrt{\frac{2E\gamma}{\pi c_0}} \tag{2.1}$$

where E is the Young's Modulus, γ is the free surface energy per unit area and c_0 is the fracture length.

Irwin [52] and Orowan [53] adapted Griffith's work by allowing for energy dissipation due to plastic flow near the crack tip, by changing the fracture energy from the surface energy to the more general energy release rate, G_c,

$$\sigma_F = \sqrt{\frac{EG_c}{\pi c_0}}. \tag{2.2}$$

Plastic flow is expected within the cobalt regions of PCD, which will increase the toughness as G_c will be greater than 2γ. The toughening role of cobalt makes it seem reasonable to apply Irwin & Orowan's modification in the understanding that the fracture of PCD deviates from that seen in the almost ideally brittle single crystal diamond. In practise, Griffith's formulation is more widely used as the fracture behaviour is typically dominated by that of the diamond skeleton, which constitutes a much higher proportion of the microstructure.

Griffith's formulation can be rearranged to give more insight into a material's fracture behaviour. For any given applied stress σ, there will be some critical flaw of size c, such that if a flaw of that size is present within a material then it becomes energetically favourable for crack propagation and so unstable fracture will occur. The ability to link c to a property of PCD, such as grain size (d) or some length scale of the cobalt pools will provide a better understanding of the way PCD fractures.

A significant body of research into the mechanical properties of PCD was performed by Lammer in 1988 [11]. He found that the primary fracture mode in PCD is transgranular cracking which implies that, given the microstructure, the bridges between the diamond grains are not significantly more susceptible to crack propagation than the diamond grains themselves. A plot of transverse rupture strength against a function of grain size (fig. 2.7) shows that two different regimes are present.

For coarse grades, (region 1), fracture follows the Griffith-Orowan strength relationship,

$$\sigma_F = K_1\sqrt{d}, \tag{2.3}$$

where K_1 is a constant and d is the average grain size, with the implicit assumption that the largest grain size is the most severe flaw leading to failure. The mode of fracture is transgranular and it was found that very often the fracture path did not change direction at the grain boundary, but followed instead the direction of maximum tensile stress regardless of crystal orientation. In single crystal diamond, fracture on the (111) planes is greatly

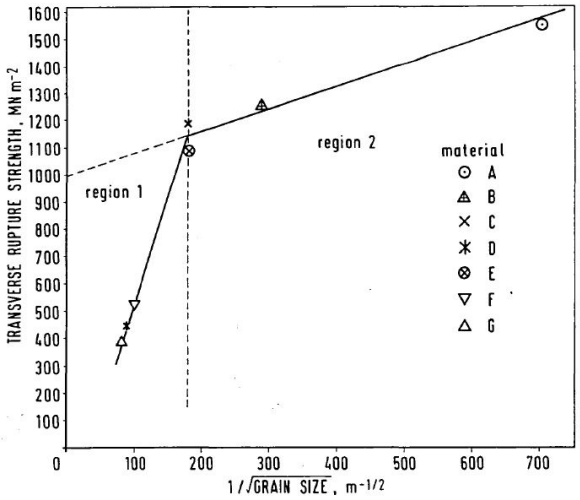

Fig. 2.7 From [11]. The relationship between transverse rupture strength, also referred to as flexural strength and grain size for a range of freestanding PCD discs. The turning point is at $170/\sqrt{\text{m}}$ which corresponds to a 35 µm grain size.

preferred [18, 28], so assuming that most neighbouring diamond grains in PCD will not be similarly orientated, fractures often form on non-ideal planes. For smaller grain sizes (region 2), transverse rupture strength follows the Hall-Petch relationship,

$$\sigma_F = \sigma_0 + K_2\sqrt{d}, \tag{2.4}$$

where σ_0 and K_2 are constants. According to Lammer, the reason for these two regions is the ratio of the critical flaw size to grain size (c/d) (after Rice [54]). There are two different relationships when c/d is either side of 1. For fine grade PCDs, σ_F is controlled by the polycrystalline fracture surface energy, whereas for coarse grades σ_F is controlled by the single crystal fracture energy as the flaw is entirely contained within one grain. In fig. 2.7, the changeover between the two regimes occurs at $d = 35\,\mu\text{m}$.

Recent research in 2015 by McNamara *et al* [55] aimed to evaluate the fracture toughness of PCD as a function of microstructure. The authors adapted the brittle fracture theory of Griffith to fit the polycrystalline nature and biphasal structure of PCD, focusing on the critical length scale and fracture toughness. In disagreement with Lammer's earlier work,

they discuss how the critical distance, c, is not trivial to define as the radius of the notch placed within a PCD structure prior to a fracture test can have different effects depending on both the grain size and whether the binder phase has been reduced. In a second study [56], the Finite Volume method was used to explore how the strength and failure of PCD varied as a function of its microstructure. It was found that the strength of PCD was influenced by the strength of the binder phase, and that the shapes and sizes of the cobalt pools and their positions with respect to the diamond grain to diamond grain bonds governed the onset of failure. Although interesting on a microscopic scale, this small scale two-dimensional $100 \times 100\,\mu\text{m}$ computational study focused specifically on the bridges between diamond grains, while it is known from SEM imaging that cracks can and mostly do propagate directly through grains. Were it to be repeated over a larger volume, a larger survey of cobalt pool shapes would be observed which would be more realistic to real-world fracture applications.

Mechanical Tests on PCD

Early work on the polishing of PCD using a diamond scaife was performed by Hitchiner *et al* [57]. Due to the polycrystalline nature of PCD, the properties were found to be isotropic however it was reported that material was removed at a higher rate than would be expected by averaging over all orientations for single crystal diamond, or even faster than when compared to the most susceptible polishing face and direction in single crystal diamond. The explanation provided by Hitchiner is that the polycrystalline microstructure changed the method of material removal. No grain pullout was observed in the polished surfaces, however the cobalt binder had been removed more aggressively by the scaife, leaving exposed edges of the diamond grains. It is well known that in brittle materials, edges are much more susceptible to chipping [50, 58–60], and the authors hypothesized that preferential fracture at exposed edges was the cause of the higher polishing rate for PCD when compared with single crystal diamond. Reducing the binder phase within the PCD only minimally affected the polishing rate, which is in agreement with their proposed mechanism only if the rate

of cobalt removal is significantly faster than that of diamond removal, and so the edges of diamond grains are rapidly exposed if cobalt is present.

Hitchiner also found interesting results regarding the mechanism of crack opening when polishing PCD in a partial vacuum [57]. Fig. 2.8, which shows the wear rate under reduced pressures, reveals that lower air pressures reduced polishing rates, which was thought to be due to gases being unable to attack open cracks and terminate bonds, resulting in an increased likelihood of bonds re-sealing. Post-fracture bond re-forming is observed in other materials but the highly brittle nature of diamond and the lack of plastic deformation near the crack tip improves the chances of bonds re-aligning as external forces are removed.

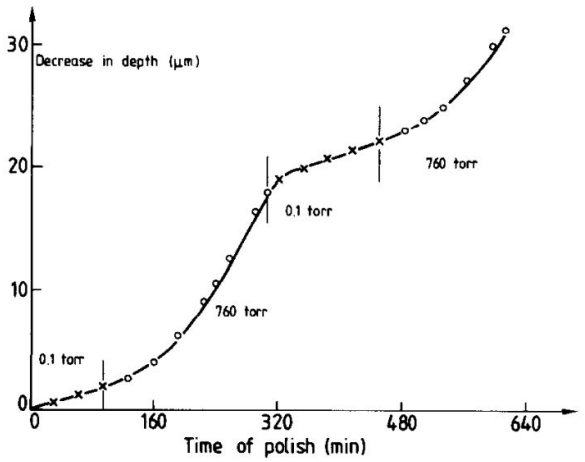

Fig. 2.8 The polishing rate of a 25 μm grain sized PCD surface on a diamond scaife under a range of pressures, after Hitchiner *et al* [57]. Lower pressures are seen to reduce the polishing rate.

A summary of a number of standard tests on PCD and how they can be minaturized and adapted to work with the limited specimen geometries is given by Morrell *et al* [50]. Throughout their work, the need for specialist testing equipment is clear. It was found that PCD is not susceptible to fatigue, even after undergoing $2x10^6$ cycles at 90% of the fracture force, which indicates that the diamond network deforms elastically until the point of fracture.

The fracture toughness of PCD was found by Lammer, shown in fig. 2.9, to increase with grain size up to a maximum at 30 µm before decreasing towards the single crystal value for larger grain sizes. Typical PCDs used in drilling applications have a maximum grain size of 30 µm or less, over which range finer grains are used to promote wear resistance whilst larger grains are used to increase the toughness and prevent large scale cracking through the compact.

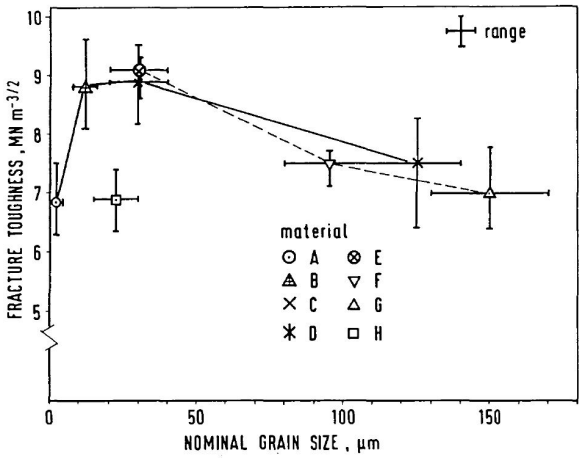

Fig. 2.9 From [11]. The relationship between fracture toughness and grain size for freestanding PCD discs obtained by loading in diametrical compression. The fracture toughness shows a peak in the region of 30 µm.

The modulus of elasticity of PCD, displayed in fig. 2.10, was found to increase with grain size but decrease with increasing cobalt content. It is not surprising that altering the microstructure can have such profound effects on the properties as the length scales involved in the grain size distribution are greater than an order of magnitude. Increasing the cobalt content decreases the proportion of the PCD which is diamond, and, as has previously been discussed above, the mechanical and fracture properties are dominated by the diamond network. The elastic properties of PCD have also been measured by D'Evelyn and Zgonc [61] using dynamic resonance, and they found that the measured values of E, G, and v lay in the ranges 915 GPa to 990 GPa, 415 GPa to 450 GPa, and $0.10 - 0.11$ respectively. However,

only 4 samples were used, and their grain sizes were not declared, so comparison to Lammer's results is not possible.

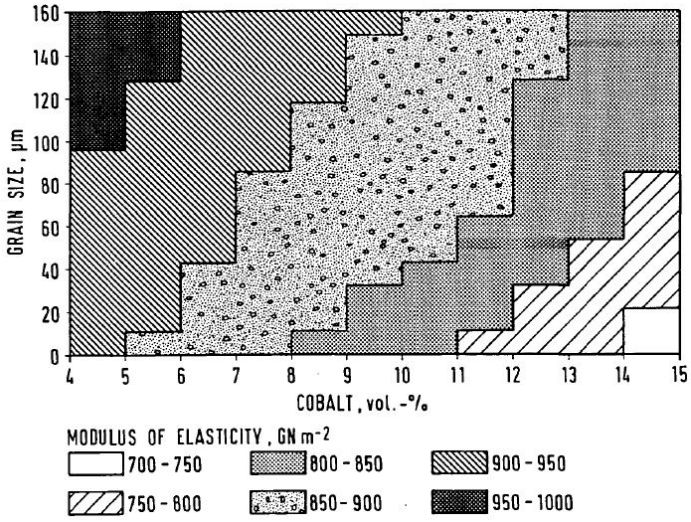

Fig. 2.10 From [11]. The modulus of elasticity varies with both grain size and cobalt content.

In order to take a closer look at the fracture of PCD, Marro *et al* [62] observed fractures caused by repeated indentation with spherical WC impactor. It was found that the damage was microstructurally dependent, and, in agreement with Lammer, the diamond primarily fractured transgranularly with no preference for the bridges between grains. From SEM images of the fractures (fig. 2.11), the cracks could be seen to terminate in cobalt pools, showing that cobalt plays a toughening role within the microstructure and increases resistance to cracks.

On a sub-micron scale, the cracks are not necessarily straight (fig. 2.12). See-saw teeth-like aspects are present on scales much smaller than a micron. The authors do not give an explanation for the shapes of these cracks, however it could be hypothesized that the crack propagates along preferential (111) planes but only for very short distances due to the desire to propagate in the direction of maximal tensile stress and due to the constraints present from matching fracture planes with those in neighbouring grains.

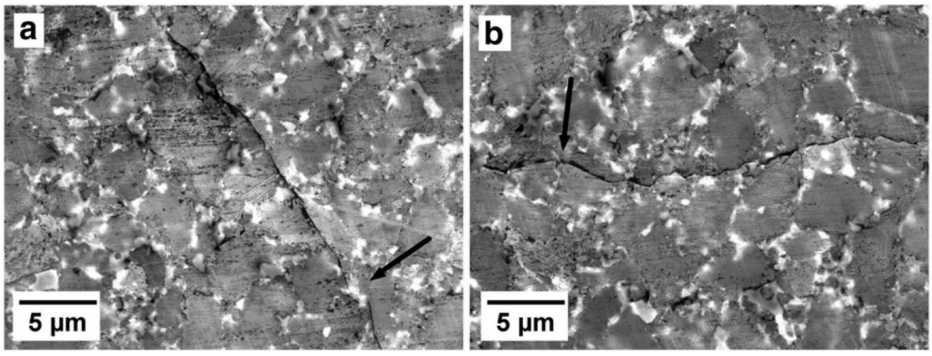

Fig. 2.11 Taken from [62]. Cracks through a 4 µm grain sized PCD after a single indentation showing (a) both straight-like propagation through adjacent diamond particles and local toughening due to interaction with binder (arrow) and (b) local crack deflection when moving from one grain to another.

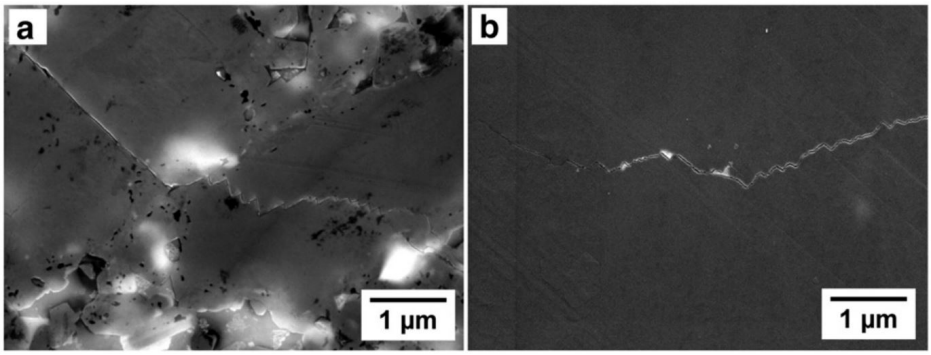

Fig. 2.12 Taken from [62]. Cracks after cyclic loading showing saw-teeth like fractures within transgranular cracks.

A second study by a similar set of authors [63] focused further on the mechanical properties and how the microstructure affected fracture and wear. By indenting PCD discs to create flaws and then fracturing them by ball on three ball tests it was found that the finer grade PCD (4 µm feed size) had the highest strength, but showed pronounced fracture resistance decay, meaning that it would fracture more easily if initial flaws were present. Coarser (20 µm feed size) and multimodal grades of PCD were more tolerant to contact damage, and so their fracture strength showed only slight changes as cracks/flaws were introduced. In comparison to Lammer, this observation also indirectly points out that coarser PCD grades exhibit higher intrinsic fracture toughnesses than fine ones. Relatively high errors were reported due to the stochiastic nature of brittle fracture in the ball vs 3 ball test, and there was no consideration for the residual stresses that may be present and how these may vary between discs or after flaws were introduced by indentation.

How Sintering Conditions Affect Structure

A study by Zhang *et al* [64] sintered a number of bi-layered PCD compacts at 5.2 GPa and a temperatures ranging from 1350 °C to 1500 °C during a 15 min heating cycle and subjected them to chemical analysis, a Knoop hardness test and a wear test. The larger grain size of 10 µm was placed as a thin layer near the WC-Co substrate, while the majority of the PCD was made from 1 µm grains. A small graphite peak was found in the XRD spectrum of the sample sintered at the highest temperature, 1500 °C whilst the sample that experienced 1300 °C did not sinter, as the temperature was below that of the WC-Co eutectic temperature and cobalt did not infiltrate the diamond powder. The Knoop hardness of the PCDs increased with sintering temperature, which the authors believed to be due to increased diamond to diamond bonding between grains. The wear resistance, measured by grinding against a silicon carbide substrate (fig.2.13), was found to increase with sintering temperature up to 1450 °C, before decreasing at 1500 °C. As the samples were sintered for comparatively short times, only 15 min, a higher temperature drives faster diffusion and a more complete sinter

of the interconnected diamond skeleton. At temperatures that are too high, which vary with location within the PCD layer, graphite becomes the preferred bonding state over diamond and so the resultant PCD is less structurally sound and is more susceptible to wear.

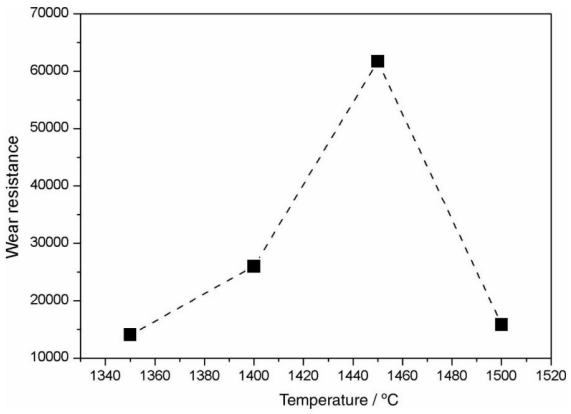

Fig. 2.13 Taken from [64]. Wear resistance, measured by grinding against a SiC substrate, of samples sintered at 5.2 GPa for 15 min as a function of sintering temperature.

It is worth noting that sintering temperatures are difficult to measure as a thermocouple cannot be placed within the compact during sintering. Any temperature gradients near the PCD compact will be unknown and as the best temperature measurement that can be achieved is by using a proximal thermocouple, the sintering temperature is associated with high errors.

It has been shown that it is possible to create very large diamond grains, larger than the feed size, when sintering PCD [65, 66]. These are normally detrimental to the performance of a PDC, however McKie *et al* [65] showed that oversaturating the cobalt with carbon suppressed abnormal grain growth. Introducing WC into the PCD microstructure was performed by Belnap *et al* [67] and was seen to increase the fracture toughness.

Wear Tests on PCD

Due to PCD's uses in abrasive drilling, a number of experiments have been performed to test wear in conditions realistic to certain applications.

Early studies were performed by Hibbs & Lee [68] in 1978 where coarse grained (100 µm) PCD compacts were worn against sandstone on a lathe. It was found that the edges would

fail either by crushing of small segments of diamond being gradually chipped away, or large portions of individual crystals would break by brittle fracture. Under higher impact forces fractures could become transgranular. Lin *et al* [46] in 1992 studied PDCs that had been used in both laboratory rock-cutting tests and field operations and identified qualitatively four failure mechanisms shown in fig. 2.14:

1. Smooth wear (fig. 2.14(a)). Drilling homogeneous formations lead to a smooth rake surface similar to those seen in polished surfaces.

2. Microchipping (fig. 2.14(b)). Small flakes of diamond, but larger than the grain size, would chip away with the direction of the plane of fracture being approximately parallel to the direction of the cut.

3. Gross fracture (fig. 2.14(c)). Large quantities of diamond would be removed.

4. Delamination (fig. 2.14(d)). The WC-Co/PCD interface would fail removing the support to the PCD layer.

More recent research by Kanyanta *et al* [44] published in 2014 studied how cracks would grow at the edge of a PDC after repeated indentations onto its edge with a WC-Co anvil at $1\,\mathrm{m\,s^{-1}}$ to $5\,\mathrm{m\,s^{-1}}$. Typical fracture fatigue behaviour was observed with cracks which, when initiated, grew intermittently with each successive impact until failure. It was found that coarse grains were more impact resistant and so it was advised that coarse grained PCD should be used where impact loading is the primary consideration.

Philbin & Gordon [69] studied the wear of PCD during the milling of wood composites. The low wear rate of PCD made identifying the wear mechanisms difficult but the authors found that dislodgement of PCD grains and micro-fracture of the PCD were both present. Chipping of the PCD was more prevalent when milling the more inhomogeneous of two types of wood.

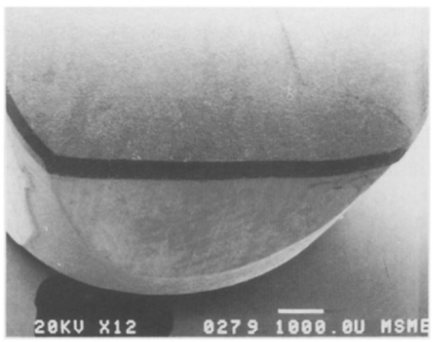

(a) Smooth Wear

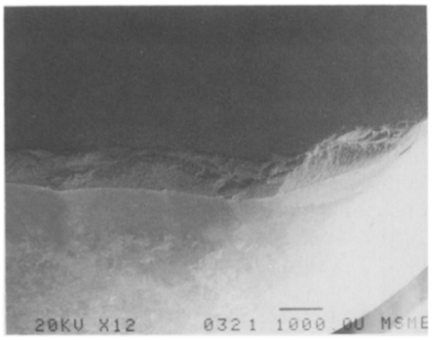

(b) Microchipping

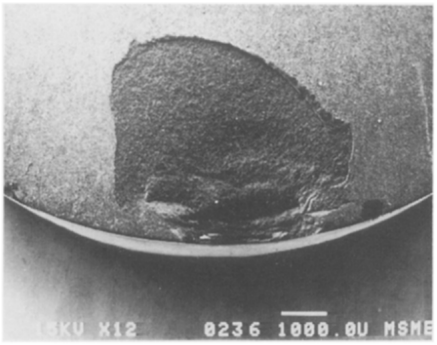

(c) Gross Fracture

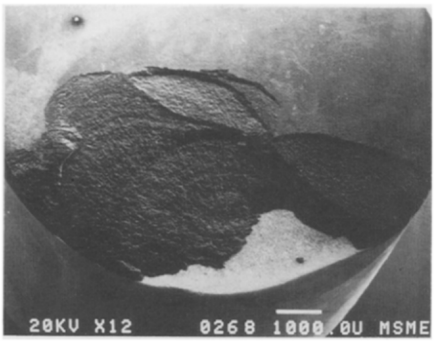

(d) Delamination

Fig. 2.14 Taken from [46]. SEM Micrographs of PDCs after wear tests showing four of the different failure mechanisms that can be present at the cutting edge.

2.3.2 Thermal and Thermomechanical Properties of PCD

The thermal properties of PCD are relevant as frictional heating can increase the temperature of the work face and cause chemical and physical changes which may affect how PCD responds to mechanical stimuli. Thermal properties are particularly relevant in oil well drilling applications, where stick-slip torsional vibrations can produce very high temperatures and accelerate bit failure, by rapidly increasing the cutting speed for short periods of time [70]. The thermal history of a sample may also affect the wear processes and rates in application. Thermal studies should be categorised by the region of the PCD that they inspect - the response varies whether studying the surface or the bulk, as the presence of oxygen in air can affect the chemical changes that occur at the surface.

Jaworska *et al* [8] studied the oxidation and graphitization of PCDs and looked at how these processes varied with different binder phases. They found that although diamond powder was lightly oxidised in air at temperatures over 600 °C, it did not graphitize. The surface of a sample of PCD with a cobalt binder showed signs of graphitization at temperatures over 600 °C. Clearly the presence of cobalt has a significant role in determining how the diamond within PCD responds to thermal stimuli. The hardness of PCD after a short heat treatment was measured with the results are shown in fig. 2.15. It is clear that PCD remained mostly unaffected at temperatures up to 400 °C, but on further heating surface oxidation decreases the hardness towards 700 °C, whereupon surface damage is so extensive that the hardness becomes unmeasurably low. The indication is that surface oxidation increased after 600 °C but the more extreme cobalt-catalysed graphitization, occurred at 700 °C. There is no discussion of how the residual stresses may affect surface hardness as the measurements were taken at room temperature.

Westraadt *et al* [71] studied the thermal instabilities in PCD caused by the presence of the cobalt binder, and showed that during the milling of a Paarl granite block there were no noticeable cracks at bulk cutter temperatures of 400 °C, ‘mosaic cracks’ at 500 °C and

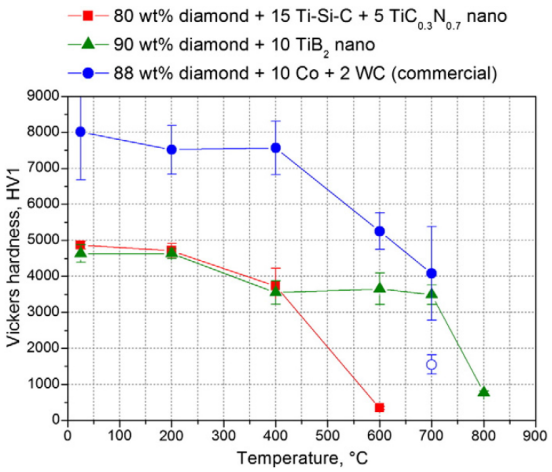

Fig. 2.15 Taken from [8]. The Vickers hardness of PCD as a function of heat treatment temperature. Treatments were performed in air and were 2000 s in duration. The most relevant material to this thesis is the cobalt-binded PCD, shown in blue.

'extensive degradation of the structure due to large scale cracks' in the bulk of the material when it failed at 600 °C. However, the location of the thermocouple was not at the contact face (which would be impossible, as it would wear away), but measured only the bulk temperature. It was found that the temperatures at the cutting face were high enough for the cobalt to catalyse the diamond to graphite transition and it is believed that the sample cracked due to subsurface graphitization and its associated volume increase, which was thought to occur at the higher temperature of 800 °C. Graphitization was confirmed in a further test where PCD was heated to 800 °C for 2 h in an argon environment and $(Co,W)_6C$ was found to precipitate, followed by bulk graphitization. Measuring cutter temperatures using thermocouples is not guaranteed to provide realistic cutting face temperatures and so bulk temperatures are not always indicative of the failure mechanism, which nucleates from the very high temperatures on the surface. It should be noted that surface wear, which will be studied in this thesis, may have a different thermal response to the large scale cracking throughout the PCD layer that is observed by Westraadt.

In a different manner, Petrovic *et al* [72] studied properties of the bulk of PCD by looking at the Young's modulus and flexural strength with both temperature (up to 680 °C) and rate

(fig. 2.16). They found that the Young's modulus did not change significantly between slow ($10^{-4}\,s^{-1}$) and fast ($10^{3}\,s^{-1}$) strain rates, and only decreased by 5% on increasing the temperature from 25 °C to 600 °C, which is consistent with their belief that the Young's Modulus increase is caused by the softening of the binder material. The flexural strength of 6 µm grain sized PCD samples remained unaffected by a heat treatment at 600 °C for 10 min. However, samples which undertook the same heat treatment but were quenched in oil to room temperature showed a decrease in flexural strength which is assigned to the changes in residual stresses that are present. Flexural strength decreased with rate however the errors in the experiment were high due to PCD's brittle response. Here, the bulk properties have been measured and the magnitude of their differences with temperature is much smaller than that of the surface properties seen by Jaworska and Westraadt.

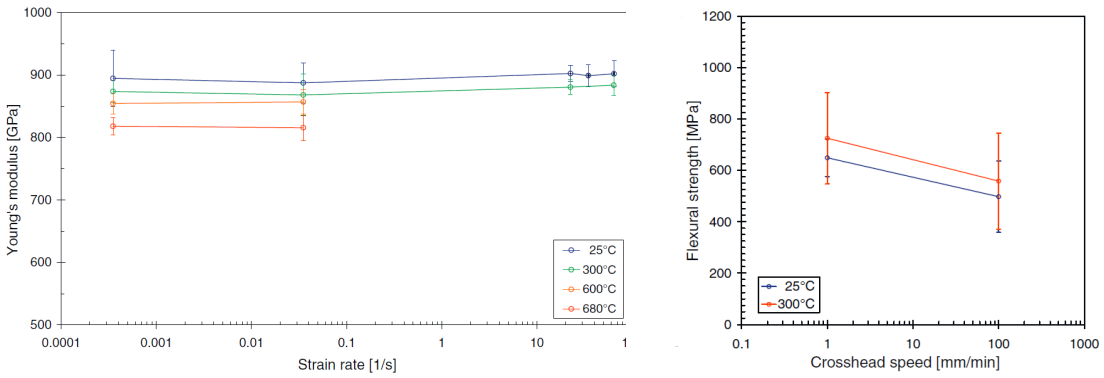

(a) (b)

Fig. 2.16 Taken from [72]. The Young's Modulus and flexural strength have been measured as a function of both strain rate and temperature using a Hopkinson bar and an Instron apparatuses. The Young's Modulus, which is primarily dominated by the response of the diamond, does not vary significantly with strain rate whereas the flexural strength, to which the properties of cobalt are more relevant, does decrease with strain rate although large errors are present.

Beyond the oxidation and graphitization processes described so far, there is also an argument that the difference in thermal expansion coefficients of diamond ($1.2 \times 10^{-6}\,K^{-1}$) and cobalt ($1.2 \times 10^{-5}\,K^{-1}$) [73] induces thermal stresses on heating as the cobalt expands more rapidly with temperature than diamond [55]. As a consequence, it is claimed by Zhan

et al [74] that as the bulk temperature of the diamond reaches above 750 °C that internal stresses from the cobalt expansion lead to severe intergranular cracking and microchipping of the diamond within the PCD structure. However, it is thought that the stresses from any graphitization at these temperatures due to the lower density of graphite (2250 $\mathrm{kg\,m^{-3}}$) than diamond (3515 $\mathrm{kg\,m^{-3}}$) [24], and due to the low Young's modulus of cobalt, will be much more significant than those caused by cobalt expansion. The relative magnitude of the two effects is studied in Chapter 5 Section 5.3.

The Effects of Reducing the Binder Phase on the Mechanical and Thermal Properties

McNamara *et al* [55] found that reducing the cobalt content decreased the toughness of free-standing PCD by 23-24% in a coarse grained PCD, and by 33% in a fine grained one. In the absence of cobalt, the stress concentrates at the edges of the newly exposed regions, thus reducing the critical flaw size to propagate fracture, and decreasing toughness. There is also some evidence for the process by which the binder phase is reduced also damaging the supposedly chemically inert diamond phase, although McNamara *et al* do discuss the possibility that the damage to the diamond is due to a change in residual stresses on removal of the cobalt. The degradation of the strength of PCD after dissolving the cobalt was confirmed by Gigl [75].

During wear tests in which the PCD is expected to be subjected to thermal stimuli, reducing the cobalt content has been shown to reduce the quantity of graphitization and microcracking found on a PCD surface [74], and has been shown to improve wear resistance in highly abrasive conditions [7]. Given that cobalt is known to catalyse graphitization, reducing the quantity of cobalt present in the microstructure is expected to improve PCD's resistance to thermal degradation.

Liu *et al* [36] further observed the decrease of PCD's wear resistance at room temperatures after reducing the binder phase, but an increased resistance at elevated temperatures. The

role of graphitization was confirmed by observing graphite in the XRD trace of worn PCD, but not in a RBPCD sample.

2.4 Preparation of the PCD to be Tested

It has been shown previously in this chapter that PCD can be created with a range of properties, and so the results of any experiment may depend on the manufacture processes that have occurred. PCD can be difficult to obtain, and it is typical for manufacturers to be secretive about their processing methods in order to obtain a competitive advantage. All of the PCD used for experiments in this thesis was supplied by Element Six Ltd. However, the precise details of the manufacture process will not be disclosed as they are kept confidential.

Three monomodal grades of PCD were provided, quantified by the size of the initial diamond feed, with 30 µm for the 'G30' grade, 12 µm for the 'G12' and 2 µm for the 'G2' grade. They all underwent the same standard sintering cycle from fig. 2.3, at a pressure greater than 5 GPa and a temperature greater than 1350 °C.

A PCD table roughly 2.5 mm thick and 16 mm in diameter was sintered with a WC-Co substrate. The WC-Co/PCD interface was flat to minimise any potential residual stresses. As the erosion experiments that will be described in Chapter 3 cause material wear at the surface, and the mass of material worn is measured, each PCD compact was cut by electric discharge machining (EDM) into two 1 mm thick discs (fig. 2.17). The advantages of this procedure included increasing the number of surfaces available to be eroded and reducing the weight of each disc to enable more accurate mass measurements. However, the residual stresses present in the discs are changed by removal of the WC-Co substrate, which must be accounted for when analysing the wear rates. It is expected that the compressive stresses will be removed and the free-standing discs will be relatively stress-free.

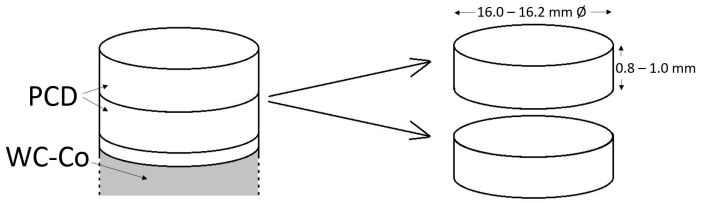

Fig. 2.17 Schematic showing the manufacture of two discs from a single PCD compact shown in fig. 1.1.

The discs were then ground flat and lapped smooth using a diamond grit paste. A limited number of samples were supplied polished and attention will be drawn to the relevance of the polished surface when these are tested.

In any one test, it was important that like-for-like samples were compared. As such, experiments were set up so that discs from the same capsule in any sintering run were eroded together, and then the same surfaces (e.g. the front face of the top disc) on the different discs were used. However, it is known that even PCD compacts sintered very close to each other in an HPHT press may undergo different sintering conditions as both pressure and to a greater extent temperature can vary across small distances, so in any experiment on a single disc there will be some random error introduced from the sintering conditions.

2.5 Summary

The extreme properties of PCD originate from a complicated manufacture process. They have been shown to be measurable via a number of methods typical for brittle materials but with adaptations required in order to account for its high hardness and the limited sample geometries that are available. A large proportion of PCD research focuses on the quasi-static room temperature properties which, although easiest to measure, can deviate from those measured either at temperatures that will be seen in applications, or with the high frequency impacts that PCD tools are subjected to when used industrially.

Fracture of PCD is dominated by the response of the diamond skeleton with both grain size and cobalt content very relevant parameters to both the fracture toughness and strength

of a PCD disc. The thermal properties vary depending on whether the surface or the bulk response is measured, with surface oxidation and bulk graphitization both affecting the response. Reducing the cobalt content reduces the structural integrity of PCD, but can improve the high-temperature performance due to the lack of graphitization.

Chapter 3

Solid Particle Erosion and the Experimental Setup

3.1 Introduction

Solid particle erosion is the dynamic process of removing material from a surface by impacting it with a large number of smaller particles. The particles can be carried by a flow of air, as in this thesis, by a dense fluid as used in slurry erosion, or as a spray initiated from a capsule.

SPE has been chosen as the wear test for this thesis as a small volume of matter can be removed from the surface of a brittle material without the risk of catastrophic failure. Further, each erosion increment integrates the damage from over 10^5 collisions, so although the mass of material lost due to each individual collision may have a high variance, averaging the mass lost over a large number of these impacts results in a precise value for the erosion rate of a single sample, with a very low variance and thus a small error. Erosion rates obtained under different conditions or after alternative sample preparation methods can be compared without encountering the typically stochastic nature of many brittle fracture tests. As such, a large amount of information can be obtained from a limited number of samples, which can be a

problem when investigating materials which are expensive or difficult to produce, such as PCD. Further, the Cavendish Laboratory has a well documented erosion facility which has been in operation since the early 1980s [76], although it has been updated a number of times since then.

There exists an international standard for erosion testing, the ASTM G76 'Standard Test Method for Conducting Erosion Tests by Solid Particle Impingement Using Gas Jets' [77]. This method is not suitable for the erosion of PCD primarily because it employs a 50 µm Al_2O_3 erodent which, when impacted onto PCD, does not produce erosion rates high enough to be measurable on sensible timescales or with reasonable quantities of erodent. Further, the suggested nozzle diameter (1.5 mm) is very small compared to the area that can be investigated and it is less feasible to construct PCD samples in the large size and rectangular shape that is proposed by the standard test. As a consequence, the apparatus described in this chapter is bespoke and has been tuned to facilitate erosion of PCD discs.

3.2 Solid Particle Erosion Background

The applicability of SPE to some situations is straightforward. Aeroplanes and wind turbine blades travel quickly through the air, which on occasion can contain dust particles. High speed impact onto these particles can damage critical components and affect performance [18]. The drive to understand the consequences of sandstorms [78] and volcanic eruptions, such as the 2010 Eyjafjallajökull eruption which closed air traffic over regions of Europe [79], has reignited recent interest in erosion processes [80]. Erosion of pipes carrying particles in suspension is another direct application of SPE that has created demand for testing [81], as has the erosion of steam turbines due to foreign objects, which can reduce efficiencies by up to 10% [82].

During this study, although similarities between the road milling and erosion processes are notable, the focus is on the response of the PCD material, and so a complete erosion

overview is not presented here. Nevertheless, an understanding of the processes that occur during SPE is useful when analysing the results and fractography presented in later chapters, and so it will be discussed here.

During erosion, material is removed by the intersection of cracks extending away from the surface. Here, the principles of brittle fracture will be discussed, then how these fractures combine to produce material loss will be put forward in Section 3.2.4. Indentation fracture can be divided into blunt and sharp indentations, depending on whether there is irreversible deformation at the contact [83]. The relevance of this particular theory is to the images of eroded surfaces which are analysed in Section 4.8.

3.2.1 Blunt indentation - Hertzian Theory

Blunt indentation can be simulated by loading a hard sphere on a flat, thick elastic specimen, which produces the classical Hertzian cone crack, first formalised by Hertz at the end of the 19th century [84]. From fig. 3.1(i), as an indenter is loaded on the surface, the region of greatest tensile stress, and so where cracks are most likely to nucleate, develops just outside the contact zone [85]. The stress field decreases rapidly with depth. Directly underneath the contact zone, the specimen is in compression, preventing tensile cracks from nucleating. In (ii), the tensile stress has increased to the point where a crack nucleates at a favourably located flaw. This crack then grows unstably around the contact circle, forming a ring crack on the surface. On further loading (iii), the ring crack grows incrementally downwards, but it is only energetically favourable to grow a short distance due to diminishing stress concentration with depth. At a critical load, (iv), the ring becomes unstable, and 'pops in' to a cone crack by propagating downwards in the shape of a frustum. It is important to note that this growth is unstable, and so an energy barrier must be overcome to initiate it. As the load is increased again (v), the crack either keeps propagating, now in an incremental, stable fashion, unless the contact circle expands to encompass the ring crack wherein the cone

stops growing. On unloading (vi), the cone crack closes, typically in an irreversible fashion as adsorption and mechanical obstruction of the surfaces prevents bonds from re-forming.

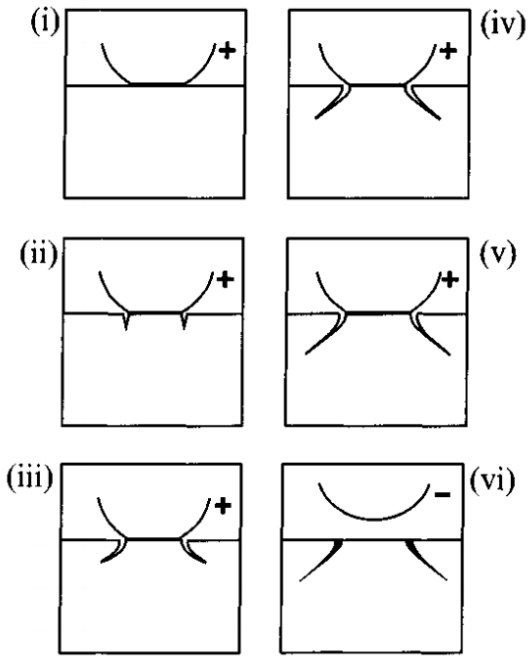

Fig. 3.1 Steps for formation of Hertzian cracks showing loading (+) and unloading (–) of a sphere on an elastic surface, after Lawn [83].

3.2.2 Modifications to Hertzian Theory

If an indenter is dragged along a surface, a series of partial cone cracks form in its wake as the tension behind the contact is increased by the frictional force [86]. There is some debate as to whether the angle between these trailing cracks and the surface increases in the presence of a friction field, as favoured by Lawn, or, as found by Chaudri [87], the cone rotates away from the direction of travel and the angle between the partial cone crack and the surface decreases. During erosion, particles are expected to be spinning and so cracks may form at a range of angles.

Yoffe [85] and Chaudhri both amended Hertz's theory for larger contact circles by adding second order terms to the expansion of the stress state. The results are similar enough to Hertz's theory to not require further discussion here.

3.2.3 Sharp Indentation of a Point Contact

The contact between two materials can become inelastic if the indenter force exceeds some critical level for irreversible deformation prior to the development of a cone fracture. Shear and hydrostatic compression are present in the region immediately below the contact zone, and can have intensities an order of magnitude larger than the tensile stresses [83].

Sharp indentation can be simulated by reducing the indenter size to a single stress singularity, as illustrated in fig. 3.2. The singularity is averted by inducing irreversible, inelastic deformation underneath the indenter until the load can be supported (dark region in figure). As the load increases, in (ii), one or more flaws within the deformation zone become unstable and at a critical load 'pops in' to form subsurface 'radial-median' cracks on tensile planes or cleavage planes. As the load increases (iii), the crack propagates incrementally downwards. On unloading, image (iv), the radial-median cracks close up, but a tensile stress field opens up on the surface. Just prior to the removal of the indenter (v), the residual stress field becomes dominant and a second crack system of sideways spreading, saucer-like lateral cracks propagate away from the base of the deformation zone. The expansion of these cracks continues (vi) until the indenter removal is complete.

It is possible that stages (ii) and (iii) may be suppressed, especially at light loads, and at a higher hardness to Young's modulus ratio, as in diamond, which increases the elastic recovery and thus the extent of radial extension during unloading.

The theory described above is valid for isotropic homogeneous materials, however it is complicated by the presence of a polycrystalline microstructure. In classic ceramics, such as alumina, the grain boundaries can be shown to shield crack propagation [88]. Increasing porosity in alumina induced a transition from a brittle to a quasi-plastic response identifiable with shear-driven defects [89]. Anisotropic compression of a skeleton microstructure, such as that found in the diamond phase of PCD, can produce bending forces in bridges between grains, introducing tension from which cracks are likely to nucleate.

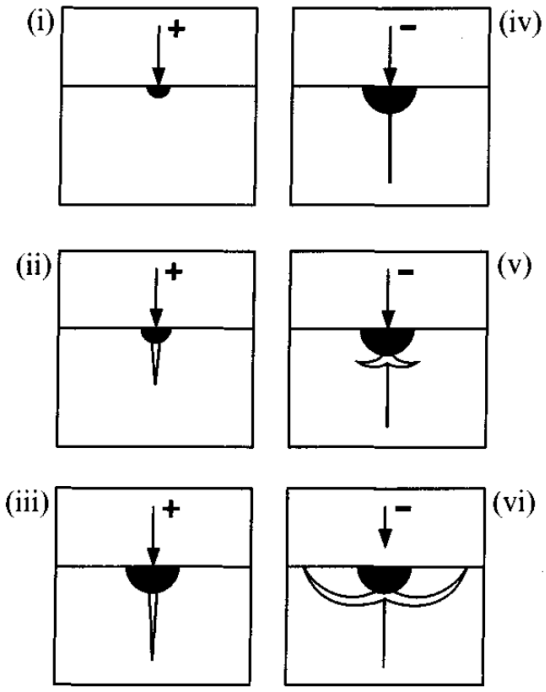

Fig. 3.2 Consequences of a sharp indentation showing loading (+) and unloading (–) stages, after Lawn [83].

Lawn [90] also found that repeated Hertzian contact on brittle homogeneous SiC produced the damage patterns seen in fig. 3.3 which are included because of their similarity to those seen in PCD in Section 4.8.

3.2.4 Repeated Impacts and Material Removal

Material loss during erosion occurs from the intersection of cracks formed in the processes described above. Starting with a virgin half-plane target material, repeated impacts will form a network of cracks and after some incubation time during which the crack population increases from zero, a steady state will occur. Now, the erosion rate will be constant with time as material is removed and new cracks are formed underneath.

There are a large number of theories predicting erosion rates given a set of parameters, including the material properties of both the erodent and the target, and the velocity, size and geometry of the erodent. An extensive review of a set of 28 different erosion theories is given by Meng & Ludema [91] which includes a discussion of the incompleteness of this set.

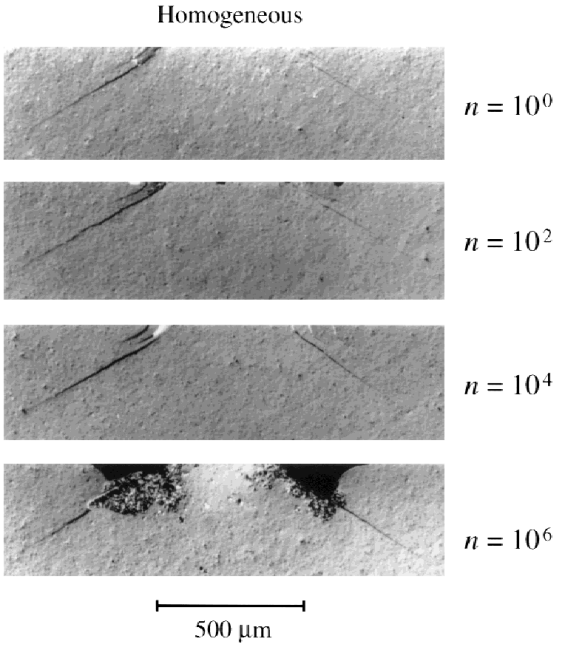

Fig. 3.3 A section view showing the consequences of repeated Hertzian contacts on homogeneous SiC, after Lawn [90].

The authors list 100 potential variables in any wear interaction and from this declare that any single theory that uses any subset of the values must be insufficient to be applicable more generally.

The parameter that is focused on specifically in this thesis is the velocity exponent. All of the theories discussed in Meng & Ludema's paper express the erosion rate (mass or volume lost per unit mass or volume erodent impacted) as proportional to the velocity, v, to some power,

$$\varepsilon = Av^n, \tag{3.1}$$

where n is the velocity exponent and A is a constant independent of velocity, whose value depends on the materials and geometry used during the erosion test. Although the energy of the erodent particle varies as v^2, the quantity of material removed per impact does not necessarily. Theories typically predict velocity exponents for brittle interactions between 2.4 and 3.2 [92], such as the $2\frac{2}{3}$ expected by Johansson [93] and the 2.8 by Wiederhorn &

Hockey [94], although the exponent has been found experimentally to range from 1.2 [18] to 6.5 [95].

The importance of the velocity exponent is that it can be used to compare erosion mechanisms. If the exponent changes between two tests, that is a clear indicator that a different process is becoming relevant to material removal.

It is standard for erosion tests of brittle materials to obtain results with the erodent impacting at normal incidence, however the response of erosion rate with angle can be an interesting parameter to measure. Brittle materials have their highest erosion rates at normal incidence, while ductile materials are susceptible to having material removed by gouging and have their highest erosion rates at lower angles. Fig. 3.4, from Finnie [96], shows this relationship clearly.

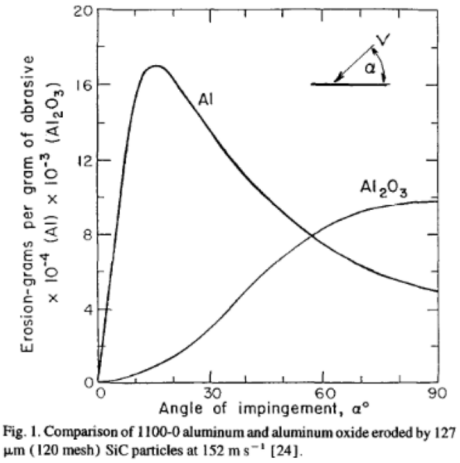

Fig. 1. Comparison of 1100-0 aluminum and aluminum oxide eroded by 127 μm (120 mesh) SiC particles at 152 m s^{-1} [24].

Fig. 3.4 A comparison of how erosion rate changes with angle for brittle (Al_2O_3) and ductile (Al) materials, from Finnie [96].

3.2.5 Limitations of Theoretical Predictions

All of the models presented above use either a perfectly rigid erodent, or in the case of Hertzian analysis, a perfectly elastic spherical erodent. Experimentally, this assumption is challenged by the fracture of the erodent on impact, especially when eroding hard materials such as PCD. As an erodent particle fractures, the manner in which energy is dissipated will

change, but also a number of smaller fragments may continue to travel towards the target and cause further damage.

It is also typical in modelling to ignore the effects of the edges and rear of the sample by assuming the sample is infinitely large. In reality, stress waves can reflect off the rear of a sample and aid in the formation of cracks. It has been shown by Zhang *et al* [97] that cracks caused by erosion can propagate all the way through a sample, causing macroscopic failure. At this stage, new erosion mechanisms, such as edge chipping, may be initiated and so the previous prediction for erosion rate must be altered.

In crystalline brittle materials, the fracture energy typically varies significantly with the plane on which the fracture propagates. The preferential fracture plane, with the lowest fracture surface energy, may not line up with the optimal crack trajectory, and so although Hertzian cone cracks may be round in amorphous materials such as soda-lime glass, they become non-circular in section in materials with preferential fracture planes, such as the (111) in silicon reported by Lawn [83]. Diamond, like silicon, is highly anisotropic and so the orientation of the (111) plane becomes relevant to fracture formation.

Further, PCD has a polycrystalline microstructure and consists of two phases. Although the fracture of the diamond skeleton is thought to be of most importance, the toughening role of the cobalt must also be considered. Erosion models are incomplete even for homogeneous solids, thus adapting one for a two-phase polycrystalline material may have limited success.

3.2.6 Modelling of the Interaction between the Erodent and the Substrate

In order to further understand the erosion process, a number of researchers have investigated and modelled the small scale impact of one or many erodent particles on a surface.

ElTobgy *et al* [98] modelled erosive wear using an elasto-plasto finite element 3D model whilst studying machined metal stacks. Their model was able to simulate local work-hardening in substrate due to repeated impacts, and thus to determine how the erosion rate changed as the surface was subjected to varying erosive behaviour. Although possibly

relevant to the effect of erodent on the cobalt binder, the nearly ideally brittle diamond within PCD is not expected to work harden under erosion.

A more recent finite element model by Wang & Yang [99] was applied to both ductile and brittle materials, and claims to be able to predict results in line with experimental data. Their approach simulates the impact of 100 spherical particles across a meshed region, a significantly greater number than the three or four proposed by ElTobgy *et al* [98], and was able to predict sub-surface cracking during erosion of SiC substrates.

Research by Antonov *et al* [100] measured experimentally the effect of introducing a third set of particles, such as small erodent fragments, between the substrate and the erodent. They showed that the wear rate could increase in brittle materials beyond that predicted by the more simplistic two-body models described previously due to the high local stresses at the smaller contact points. This study gives some depth to the complicated erosion process and shows that modelling idealistic collisions has limitations, and that more complicated finite element models are required to further understand the erosion process.

An understanding of how the erodent might fracture on impact was performed by Hadavi *et al* [101], by recording the impact, fracture and rebound of sub-millimetre SiC particles using a high-speed video camera during erosion, complementing this with a computer model of the fracture of the erodent particle. Their results, further confirmed in a second publication [102], showed that there was a threshold kinetic energy below which no particles would fracture. It is expected that all experiments in this thesis would experience erodent impacts faster than this velocity. A demonstration of the break up of SiC erodent particles on impact, and how a greater number of fragments is created at higher velocities, is shown in fig. 3.5.

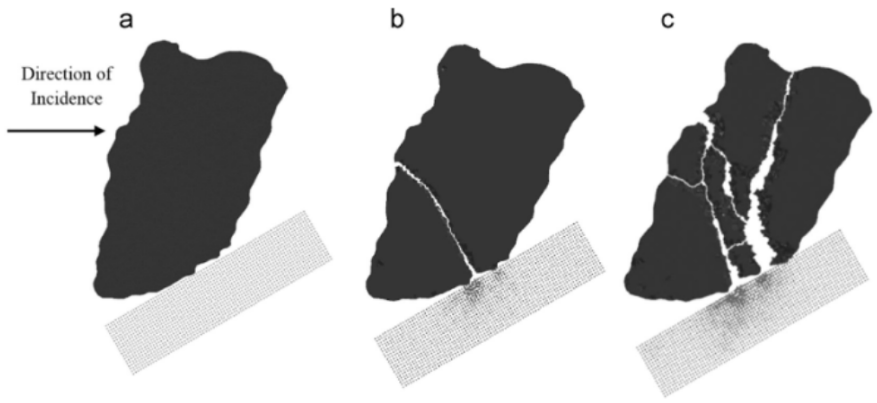

Fig. 3.5 Sequence from a model of an SiC particle impinging on a surface before impact in (a), after impinging at 46 $m\,s^{-1}$ in (b) and after impact at 100 $m\,s^{-1}$ in (c). From Hadavi *et al* [102].

3.2.7 The Use of SPE as a Test to Simulate Wear

The most common form of material degradation observed during drilling applications is abrasive wear, caused by the passage of hard particles over a surface. In this thesis, erosive wear is studied, and so if the results of these SPE experiments are to be considered in the context of any practical application of PCD in drilling, the similarities and differences between the two regimes for brittle materials must be understood.

Abrasive wear can be sub-categorised into two modes, two-body and three-body wear. In two-body abrasive wear, hard asperities or rigidly held grits pass over the surface like a cutting tool [103], whereas in three-body wear the grits can roll or slide over the surface, typically resulting in a reduced rate of material removal [104, 105]. For both modes, Stachowiak & Batchelor [103] provide two mechanisms for abrasive wear in brittle materials, shown in fig. 3.6, with the grain pull-out mechanism more prevalent in materials with weak grain boundaries.

Erosion is expected to occur via the mechanisms described earlier in this chapter, whereby cracks caused by either blunt or sharp loading propagate into the surface and intersect to cause mass loss. Crack development and expansion during erosion can be directly compared to Stachowiak's example of abrasion-caused fracture in fig. 3.6, with the modification that

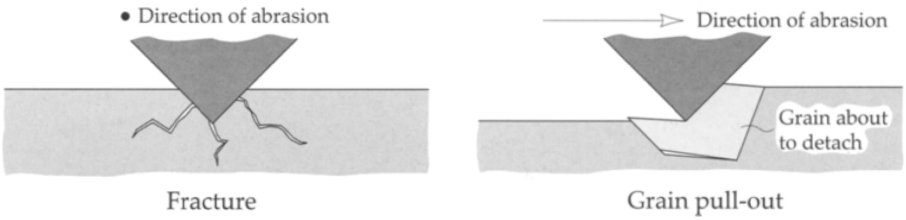

Fig. 3.6 Adapted from [103]. Two mechanisms of abrasive wear in brittle materials.

the timescales involved in the impact of erodent are shorter. It has previously been shown (in fig. 2.16) that the properties of PCD do not depend greatly on strain rate, and so cracks that form through both abrasive and erosive wear are expected to follow similar mechanisms. In addition, the sound-speed in diamond is very fast, over $12\,\mathrm{km\,s^{-1}}$ [19], and so fast-impacting particles will still interact with a large volume of substrate, reducing the potential for highly localised fractures. The second mechanism, grain pull-out (also referred to as pluck-out) is seen during erosion of WC-Co targets [106], however is thought to be less likely in PCD due to the high strength diamond bridges which exist between the grains.

Research by Hutchings [107] aimed to produce wear maps to determine under which conditions erosion and abrasion caused similar or different wear processes. It was shown that discontinuities in the slope of the erosion rate with velocity were a clear indicator that a new mechanism was engaged. No such discontinuity was identified during the erosion of PCD (e.g. Section 4.6), giving confidence that increasing the impact velocity from $40\,\mathrm{m\,s^{-1}}$ to $160\,\mathrm{m\,s^{-1}}$ does not drastically alter the material removal mechanism (further discussed in Section 4.8). Contrasting efforts by Wada [108] showed that the erodent particle material greatly affected both the erosion rate and the mechanism. As such, caution must be exercised when comparing the wear rate between erosion experiments using alternative erodents.

To summarise, there are some clear similarities between the abrasion and erosion regimes, and each can be used to help better understand the other. However, if designing PCD tools for one particular application, although the broader material behaviour including the

response at high temperatures can be characterised well by erosion, tests specific to the desired application must be performed.

3.2.8 Previous SPE on Diamond and PCD

A review containing a number of diamond erosion studies has been written by Walley & Field [12]. The authors describe the long history of diamond's susceptibility to erosion despite it's high hardness, with the first report dating from 1873.

It has previously been found that cracks formed by erosion in single crystal diamond tend to form along preferred crystallographic planes [109] but that Hertzian cone cracks can occur with higher hardness erodents [110]. Some interest in the erosive resistance of CVD diamond films has lead to testing of these, with the most recent research being performed by Wheeler & Wood [111, 112] including impacting with a diamond erodent [113] during which the predominant erosion mechanism was that of fracture by lateral and radial cracks. Davies [114] measured the velocity exponent for both single crystal diamond (1.2 ± 0.7) and a polycrystalline CVD diamond film (3.4 ± 0.4). The contrasting exponents imply that the microstructure is relevant to the erosion mechanism, a concept that will be relevant to PCD erosion which is explored further in Sections 4.6 & 4.8.

A recent erosion study by Ramsay [115] on how nitrogen defects in single crystal diamond affected the physical properties, focused on applying the theoretical erosion rate prediction by Johansson *et al* [93] for brittle materials to the erosion of single crystal diamond. It relied on the predicted erosion rate,

$$\varepsilon = A \frac{E}{H^{1/3} K_{IC}^2} \rho_t \rho_p^{1/3} R v^{8/3}, \tag{3.2}$$

where A is a constant independent of velocity, E, H, K_{IC} and ρ_t are the Young's Modulus, Vickers hardness, fracture toughness and density of the target, and ρ_p, R and v are the density, radius and impact velocity of the impacting erodent, which is assumed to be spherical and

elastic. Johansson obtained this expression for erosion rate by calculating the average spalled volume per impact due to median-radial cracks. Ramsay used the expression above and measured Vickers hardnesses to obtain a comparative study of the fracture toughness of diamond as a function of the nitrogen concentration. He found that, although with large errors, the erosion rate of single crystal diamond was dependent on the concentration of nitrogen in the sample.

The initial erosion test on PCD was performed by Haywood [116] however results were inconclusive due to the very low erosion rate of PCD. Further tests were performed at the Cavendish by Feng & Field [117] and by Kaye & Field [118, 119]. Both tests used a 25 µm SiO_2 erodent impacting at velocities up to $250\,\mathrm{m\,s^{-1}}$.

Feng & Field found that the mechanism of material removal was different to those proposed in the theories above and that it involved firstly the removal of the metal binder, then deposition of silica in the recesses that remained, followed by fracture of the diamond skeleton. The evidence for this was the more rapid removal of cobalt and the deposition of SiO_2 in the regions where cobalt had been removed, as identified by EDX spectroscopy. They also found a similar erosion rate for both single crystal diamond and PCD. They measured the erosion rate of their PCD to be negligible at $70\,\mathrm{m\,s^{-1}}$, $0.05\,\mathrm{mg\,kg^{-1}}$ at $140\,\mathrm{m\,s^{-1}}$, and $0.1\,\mathrm{mg\,kg^{-1}}$ at $200\,\mathrm{m\,s^{-1}}$.

Kaye & Field wished to study PCD under more highly erosive conditions, and so reduced the erodent size from 500 µm to 250 µm and increased the velocity to $(250 \pm 30)\,\mathrm{m\,s^{-1}}$. A typical erosion test lasted over thirteen hours. They found that the erosion rate was very low, $(0.088 \pm 0.003)\,\mathrm{mg\,kg^{-1}}$, and found that the erosion mechanism was the same as previously reported. They also found that the initial erosion rate was higher than the long term rate, which was put down to the surface preparation method, and the rapid removal of exposed cobalt prior to diamond erosion, although value of the mass of exposed cobalt is not sufficient to fully explain this effect. There was some difficulty in obtaining an erosion mechanism

under these conditions, as the average depth eroded across the surface was just 29 µm, hardly greater than one grain size. An example erosion profile is given in fig 3.7.

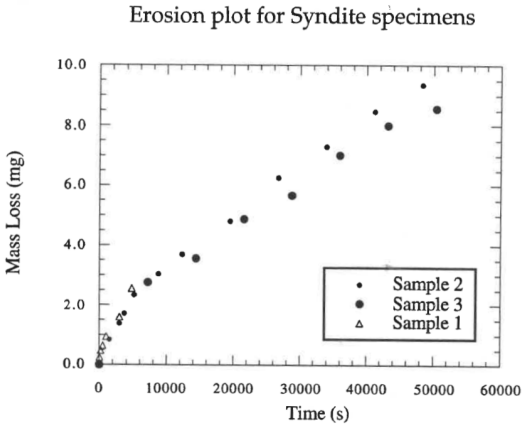

Fig. 3.7 The erosion of PCD with 250 µm SiO_2 impacting at 250 m s^{-1}, from Kaye [119].

Kaye [119] also cites issues with preferred fractures at the edges of his PCD discs, despite an attempt to sink the disc in wax to protect them. This 'edge chipping' was of concern when designing the experiments performed in this thesis and steps were taken to prevent it.

It is debatable to what extent the previous erosion of PCD can be compared to results presented in this thesis as little is known about their test material beyond the grain size and it is expected that the manufacture process of PCD, including pressure and temperature profiles during sintering, will have developed and improved in the 25 years that have passed between the experiments.

3.3 Apparatus and Procedure

The Cavendish erosion apparatus (fig. 3.8) consists of a screw-controlled hopper from which erodent is sucked into a venturi section of a long accelerating tube. The erodent speeds up in the air flow as the tube narrows, finally exiting out of the barrel and impacting on the target (fig. 3.9). The air flow is driven by the laboratory compressed air line at pressures up to 8 bar, with typical flow rates at up to 650 l min^{-1}.

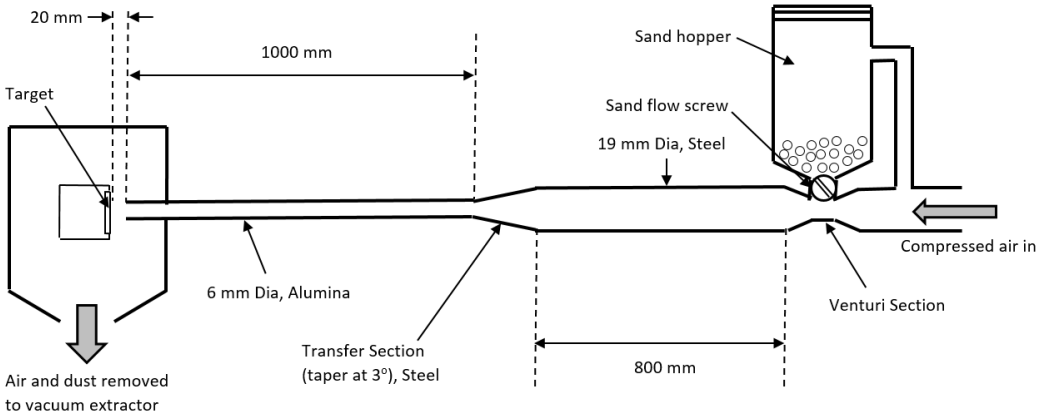

Fig. 3.8 A schematic of the Cavendish Erosion Apparatus. Not to scale. Erodent is dropped into an airflow before being accelerated in a sequence of narrowing barrels and then is impacted on the target.

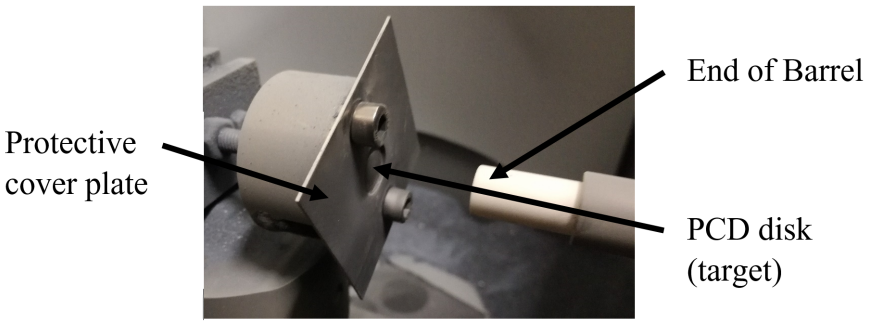

Fig. 3.9 A close up photo of the end of the barrel and the target. A protective plate is in place to prevent chipping of exposed edges of the PCD disc.

The erodent spot size can be altered by changing the barrel diameter, and the erodent velocity is altered by regulating the pressure of the incoming compressed air. The typical stand off distance between the barrel and the target is 20 mm. Edge-chipping has been minimised by adding a 1 mm thick stainless steel protective cover plate. However, as PCD is the material with the highest erosion resistance, direct impact of the erodent onto the cover plate (which would be expected to cause significant damage to it) was avoided by ensuring that the erodent spot size was smaller than the hole in the cover plate. The typical barrel diameter was 6 mm although some experiments required a 4 mm version.

The erodent flux rate is thought by some to be an important parameter in erosive behaviour [76, 120] as erodent-erodent interactions above the surface prevent each collision from being independent. The flux rate was of the order of 1 kg of erodent every 4 min, or just over $4\,\mathrm{g\,s^{-1}}$. A high speed video was taken of the erodent impacting on the surface and very few erodent-erodent interactions were observed. As such, it is thought that the erodent flux rate is not a relevant parameter in this thesis and small variations in the erodent flux rate may be disregarded during the analysis of erosion rates.

During each erosion test, the sample is loaded into the sample holder, the airflow turned on and the erodent feed screw is opened. Once the hopper has emptied of erodent, detected by a thermocouple placed behind the target (which heats up by an average of 4 °C across an experiment), the airflow is stopped. The sample is removed from the chamber, washed in an ultrasonic water bath for 3 minutes, then rinsed with acetone and blown dry. Then the sample is weighed. This forms one 'increment' of erosion, of which 5 to 8 increments construe a complete erosion test run. From these, the first increment is typically disregarded due to the variability in surface preparation methods, and a straight line is fitted to the rest of the points to yield an erosion rate and with an error determined by the least squares fit, as is suggested by Patterson & Levy [121] to diminish the rounding errors obtained by measuring very small mass losses. Patterson & Levy [121] further showed that ultrasonic specimen cleaning can

have an effect on the erosion rate as embedded particles can be removed between erosion increments, so consistency in the procedure will be ensured by washing in an ultrasonic bath for the same length of time between each increment of the same mass of erodent. Due to the low erosion rate of PCD (discussed in Section 4.3) and the large quantity of erodent used in each increment, the steady state conditions will be returned to rapidly after the sample is cleaned, with the expectation that the cleaning will not significantly affect the erosion rate.

Absolute erosion rates themselves can be a difficult property to measure consistently. During an erosion experiment, especially of a material such as PCD with a very low erosion rate which requires highly hostile conditions, all of the components of the apparatus will wear away, which can then change the erosion rate. For example, erodent passing down a barrel will impinge on the side of the barrel and, over time, widen it. For a specific driving pressure (or fixed flow rate of air), the erodent velocity will change (usually slow down), thus reducing the erosion rate. This, and similar factors, must be considered when reporting erosion rates, and noted when comparing between them. As a consequence, absolute erosion rates are generally avoided and typically the relative comparison between different conditions or samples is discussed. Many experiments, such as those in Chapter 5, are run concurrently, so that the first erosion increment is completed on all of the samples before the second is done on the first. Within each increment, the order with which each sample is eroded is randomised. The outcome is highly reliable erosion data for comparing between these samples, but with erosion rates that reduce with time and are more difficult to compare to experiments performed at other times.

3.4 Velocity Calibration

The velocity of the erodent was calibrated using a high speed video camera (Phantom V1610) capable of over 100,000 frames per second. To preserve the camera and lens, the erosion chamber was emptied of the sample holder and the camera was placed outside the

chamber, viewing through a polycarbonate window at the backlit erodent. Fig.3.10 contains three stills from the calibration video, showing how individual erodent particles were tracked over time.

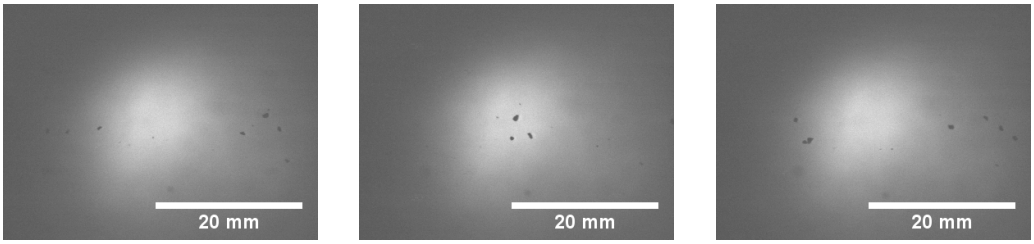

(a) $t = 0\,\mu s$ (b) $t = 250\,\mu s$ (c) $t = 500\,\mu s$

Fig. 3.10 Three stills taken from the high speed video camera. The images were taken 25 frames and 250 µs apart. A group of three erodent particles can be seen to move from right to left.

The camera control software was used to calculate the velocity of individual particles, which were collated and an example velocity histogram for a particular driving pressure is presented in fig. 3.11. As the error in the mean velocity is small (of the order $1\,m\,s^{-1}$) and the spread in velocities is important, the erosion velocity is given as the mean velocity $\pm$ the variance, assuming a Gaussian distribution.

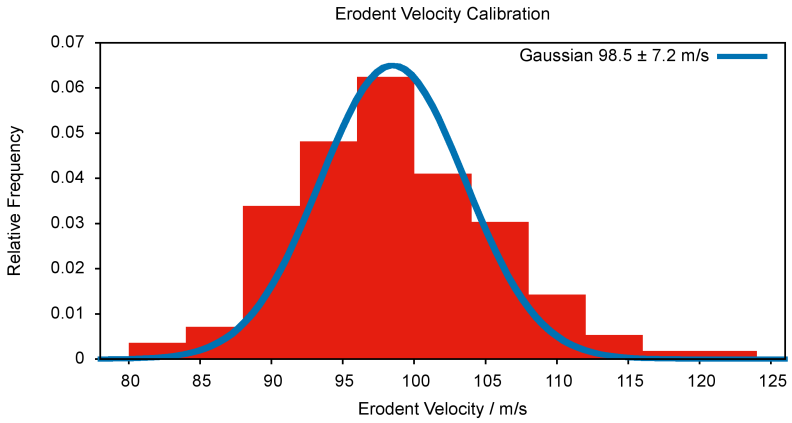

Fig. 3.11 Histogram of erodent velocities as measured by a high speed video camera over a distance of 4 cm of free flight. A Gaussian has been fitted to the data.

The erodent velocity was recalibrated every time that the driving pressure was changed and before each new experiment, or if it was thought that a previous experiment had caused significant barrel wear.

3.5 Erodent Specification

Three materials were used as erodents during the experiments presented in this thesis. A rounded silica sand (SiO_2 conforming to British Standard 1881 131, 'Fraction C') erodent with a mean size of 525 µm was the original erodent and had been used previously during Ramsay's [115] erosion of single crystal diamond. After only very low erosion rates were measured eroding PCD with SiO_2 (Chapter 4, Section 4.3), alternative erodents were sourced. A supplier was found of angular 36 mesh alumina (Al_2O_3) and angular 36 mesh silicon carbide (SiC). SiC was used in the majority of erosion experiments on PCD due to the higher and more easily measurable erosion rates it produced (Section 4.3).

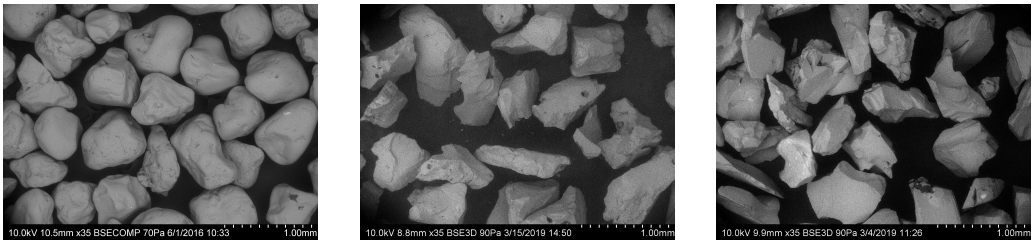

(a) Rounded SiO_2 sand. (b) 36 mesh Al_2O_3. (c) 36 mesh SiC.

Fig. 3.12 Backscattered SEM images of three of the erodents used during this research.

Understanding the properties of the erodent and what happens to it as it impacts PCD at a range of velocities can aid the understanding of the erosion process and help explain the mass loss mechanisms that are present [122]. In fig. 3.13, the three erodents have been imaged before and after impact on PCD at 83 $m\,s^{-1}$. None of the original erodent particles remain unfractured, in contrast with the theories presented in Section 3.2.4.

The SiC erodent has been analysed before and after impact using a Malvern Morphologi G3 particle size analyser, which distributes particles on a glass slide and analyses them using

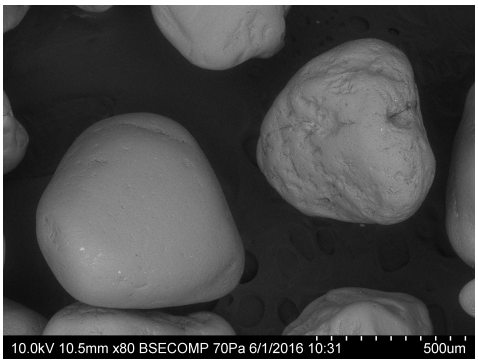

(a) Rounded SiO_2 sand.

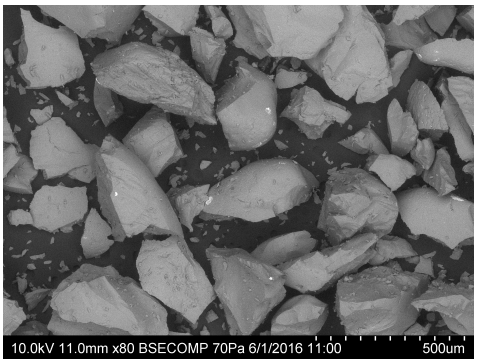

(b) Fractured SiO_2 sand.

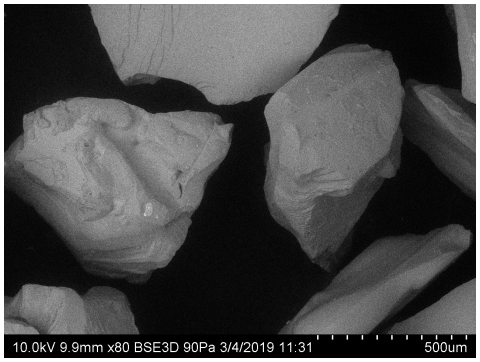

(c) 36 mesh SiC.

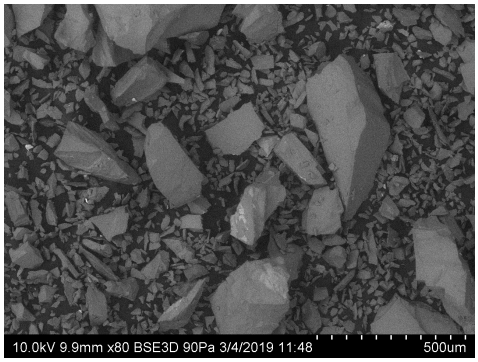

(d) Fractured SiC.

Fig. 3.13 Backscattered SEM images of SiO_2 and SiC erodents after impact onto PCD at $83\,\mathrm{m\,s^{-1}}$.

an optical microscope with image analysis software. Data is shown as the circle equivalent (CE), diameter, which is the diameter of a circle with the same area as the particle. As the particles are non-circular, the CE diameter recorded is larger than any mesh-derived diameter, as the particle can pass through the rectangular mesh perpendicular to it's longest axis. During preparation for imaging, irregular particles are more likely than average to come to rest on the glass slide on a larger face, or one closer to their centre of gravity. Although expected to be a small effect, this will increase the measured sizes of particles above the average in all dimensions.

The focus has been on the 36 mesh silicon carbide purchased from Guyson International Ltd. It has been manufactured by the Acheson process, before being sieved through a mesh of between 36 and 38 gaps per inch, giving a nominal diameter of 525 µm.

The size distribution of the erodent as supplied is shown in fig. 3.14. The number distribution is skewed by the set of smaller particles which are not expected to be noise from the sizing instrument as a background image has been taken and subtracted from the data. They will be from small fractures of the larger particles, and from grains stuck to the larger particles during the sieving process. These smaller particles are not expected to contribute significantly to the erosion rate as they form a negligible fraction of the overall volume, and hence mass, of SiC (fig. 3.14b).

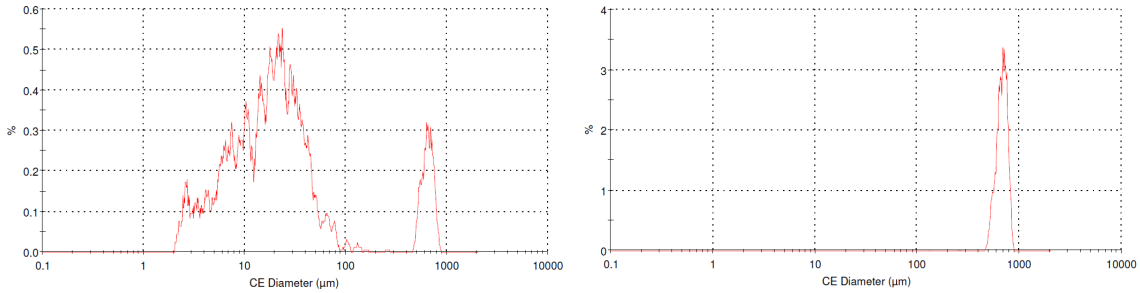

(a) Number Distribution. (b) Volume Distribution.

Fig. 3.14 As supplied 36 mesh SiC analysed by a Malvern Morphologi G3.

On impact, figs. 3.15 & 3.16, the erodent fractures. The brittle shattering of the erodent particles is clearly different to the contact of elastic spheres referred to in Section 3.2.1, and matches closely the distribution measured by Hadavi *et al* [101] for the impact of SiC erodents onto machined metal stacks. The maximum particle size reduces to 200 µm for the impact at 83 m s^{-1} and 100 µm for the impact at 156 m s^{-1}. There is also an increase in very small particles (< 2 µm) when compared to fig. 3.14.

Although this change in SiC size distribution is not surprising, the fact that no original shaped particles remain, and the increased break up of erodent with impact velocity are worth noting. The Morphologi gives further data which can be used to compare the erodent before and after impact. The values for the erodent after impact at 83 m s^{-1} are compared to the as supplied erodent in tab.3.1.

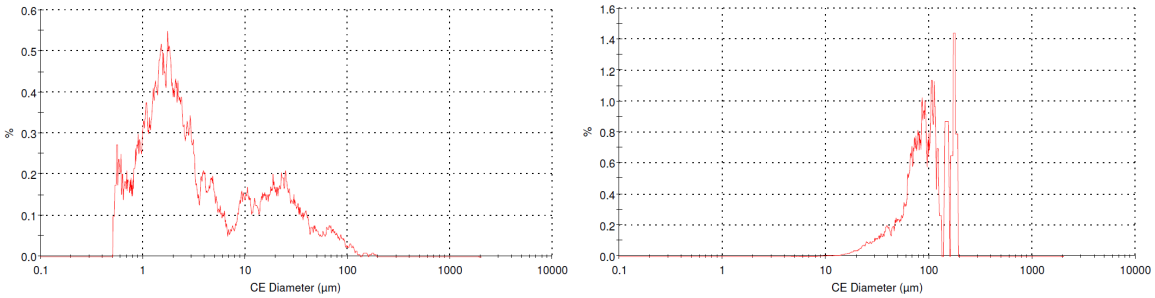

(a) Number Distribution. (b) Volume Distribution.

Fig. 3.15 36 mesh SiC collected from erosion chamber after impact on G2 PCD at 83 $\mathrm{m\,s^{-1}}$ analysed by a Malvern Morphologi G3.

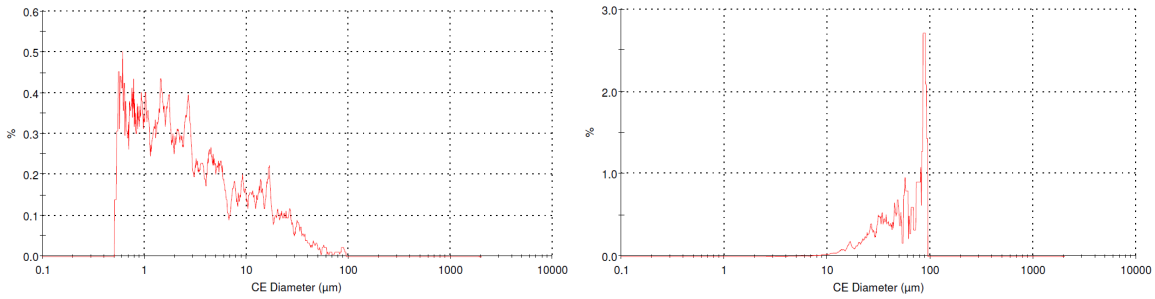

(a) Number Distribution. (b) Volume Distribution.

Fig. 3.16 SiC collected from erosion chamber after impact on G2 PCD at 156 $\mathrm{m\,s^{-1}}$ analysed by a Malvern Morphologi G3.

Not only have the particles become smaller, but also they have become more angular and have a decreased aspect ratio, as could be judged qualitatively from fig. 3.13. The convexity however has not changed and remains high. The decreased circularity is inevitable if flat fracture surfaces cut through an initially (approximately) round particle.

3.6 Summary

SPE is a highly applicable wear test for PCD as a large quantity of information can be obtained from studying a single sample. Repeated impacts onto a surface cause subsurface cracking followed by material removal. The mechanisms for creation of cracks depend on whether the impact can be defined as sharp or blunt, depending on whether there is plastic deformation underneath the contact zone. Any theory that is applied must be adapted to

Parameter	Definition	Unused Erodent	Used Erodent
Circularity	Circumference of equivalent area circle divided by the actual perimeter of the particle	0.854	0.831
Convexity	Convex hull perimeter divided by actual particle perimeter	0.942	0.943
Aspect Ratio	Width divided by length	0.751	0.650

Table 3.1 Properties from Malvern Morphologi G3 Analysis. Small particles less than 20 µm CE diameter have been discounted due to their low volume fraction.

work with PCD, as the biphasal and polycrystalline features ensure that it deviates from any standard set of initial conditions.

Previous erosion on diamond and PCD has been limited. Only few PCD samples have been studied, and rarely has enough PCD been removed from the surface to deviate fully into the bulk of the material. All previous erosion has used a SiO_2 erodent.

The apparatus that was used to perform erosion throughout the research presented here has been described, including the method for velocity calibration. The erodents that are used have been characterised with a focus on the F36 mesh SiC that will be used for the majority of erosion experiments. All of the erodents were found to fracture on impact, but at higher erodent velocities the erodent was found to fracture into smaller pieces.

Chapter 4

Solid Particle Erosion of PCD

4.1 Introduction

The data presented in this chapter represents the majority of experiments performed during the current course of study. All the experiments here were preformed using the apparatus described in chapter 3 and were conducted at ambient temperature.

The chapter begins with a comparison of erodents, and how they affect the erosion rate, before giving a justification of the use of SiC for further experiments on PCD. The focus then shifts to how varying the erodent velocity and angle can be used to understand the processes that occur during erosion of the different grades of PCD. An extensive SEM study was performed in order to identify the material removal mechanism and to investigate how this changed with grain size of PCD. Once the mechanisms by which fractures propagate and material is removed during erosion of PCD are understood, the erosion process can be used to learn more about changing PCD to increase wear resistance, which is introduced in Chapter 5.

4.2 Preliminary Results with a Silica Sand Erodent

Historically, the original erodent used in SPE experiments was silica sand, SiO_2 [12]. The relevance to real-world applications, such as wind turbine blades in desert environments and aeroplanes moving through sandstorms, as well as damage to buildings and structures by wind-carried sand has motivated past erosion research [123]. SiO_2 has also recently been used by Ramsay [115] for studies of the erosion rate of single crystal diamond using the same set of apparatus described in this thesis. A comparison to the erosion rate of PCD under the same conditions will be made here.

Initial erosion experiments were conducted by impacting SiO_2 at normal incidence onto polished surfaces of PCD with a 30 µm grain size. The erosion profiles are given in fig. 4.1, and show that on impact at low speed, at $(84 \pm 6)\,\mathrm{m\,s^{-1}}$, under the same conditions that Ramsay [115] measured an erosion rates of order $0.1\,\mathrm{mg\,kg^{-1}}$ on single crystal diamond, there is initially 0.3 mg of mass removed during the first 5 kg of erodent used, followed by a levelling off of the erosion rate, after which very little material is removed from the PCD surface. This short term 'transient' response was not observed with single crystal diamond and so the presence of exposed cobalt on the polished surface, which will be significantly softer and easier to remove, is thought to cause the more rapid initial mass loss.

A second sample was eroded at twice the impact velocity. A similar initial response is seen, followed by longer term erosion at a very low rate ($0.04\,\mathrm{mg\,kg^{-1}}$), as shown in fig. 4.1(b). During the second stage, diamond starts to be removed in small amounts, which can be shown by calculating that a mass loss of 1 mg over an erosion area 6 mm in diameter removes material to an average depth of 10 µm, around a third of the grain size. The relatively high erosion rate during the initial erosion phase is consistent with what has been previously observed by Feng [117] and Kaye [118] and an estimation here of the expected quantity of cobalt exposed on the surface of a polished sample with a 30 µm grain size indicates that it is around 0.3 mg.

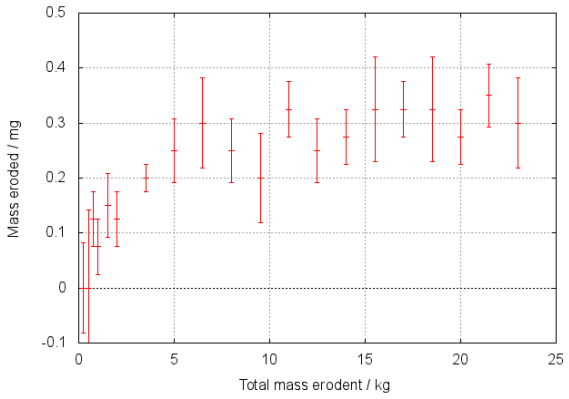

(a) SiO_2 erodent impacting at $(84 \pm 6)\,\mathrm{m\,s^{-1}}$.

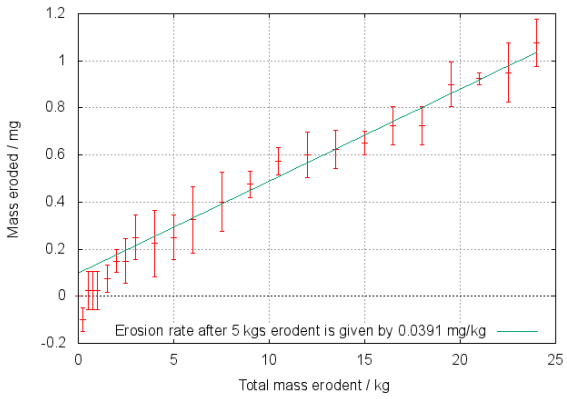

(b) SiO_2 erodent impacting at $(163 \pm 12)\,\mathrm{m\,s^{-1}}$.

Fig. 4.1 Erosion profiles for two G30 PCD discs over an erosion area 6 mm in diameter. The response is composed of an initially rapid 'transient' phase followed by a longer term 'steady state' phase.

A SEM image of the surface eroded at the lower velocity in fig. 4.2 shows that the large diamond grains have mostly remained unaffected by the impacting erodent. However, where previously there were exposed cobalt pools on the surface, these have been eroded away and a thin layer of SiO_2 has been deposited in the recesses. If diamond has been removed, it has been from the exposed areas at the edges of the grains as the larger regions of diamond have not been damaged. Silica can also be found smeared on top of the surface in places, indicating that the cleaning process that occurs before weighing does not remove all of the erodent from the PCD, which explains why during the very first erosion increments, the mass of the sample can stay the same, or even increase.

Images of the erodent before and after impact presented in Chapter 3, fig. 3.13, show that it fractures as it hits, and forms a large number of finer shards. As the radius of the original sand particle (265 µm) is too large to remove cobalt from the gaps between diamond grains, these sharp fines must perform a role in the material removal process, either during secondary impacts or after embedding within the recesses on the surface.

To summarise, preliminary experiments with a SiO_2 erodent produced similar erosion results to those in the literature, and demonstrated that PCD was more resistant to erosion than single crystal diamond under the same conditions. The depth of erosion was very small,

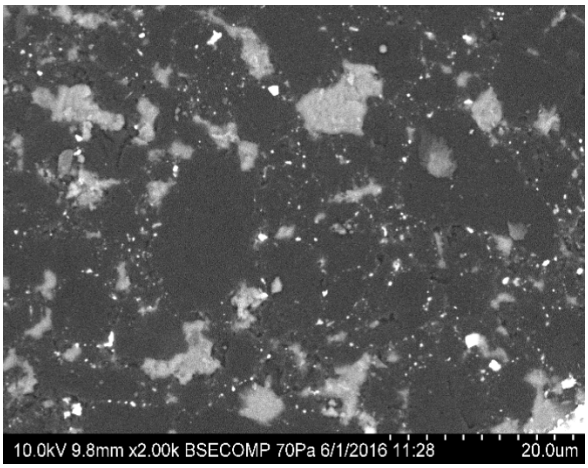

Fig. 4.2 A secondary electron SEM image of the surface eroded in fig. 4.1(a). EDX analysis confirmed that the dark areas are diamond, the white is cobalt, and the grey regions are composed of crushed and compressed SiO_2, which are more clearly visible in Section 4.8. There is less cobalt present than on a comparable pristine surface, examples of which are given in fig. 2.5.

10 µm or less, and only minimal amounts of material were removed from the surface while using large quantities of the SiO_2 erodent.

4.3 Alumina and Silicon Carbide Erodents

Although the use of SiO_2 as an erodent did successfully wear the PCD surface, a large quantity of sand was required and only very small mass losses were measured. In order to meaningfully compare the wear of PCD discs whilst varying the erosion conditions and PCD preparation methods, an impractical and uneconomical quantity of SiO_2 would be required.

It is known from erosion theory presented in Chapter 3 that increasing the size, hardness, density and angularity of an erodent will increase the erosion rate. To ensure that the erodent feed system did not jam, an issue found by Ramsay [115], a similar sized erodent was required. The physical properties of the erodents can be changed by using alternative materials, and the increasingly hard Al_2O_3 and SiC were chosen. Both erodents had angular, non-rounded edges due to their preparation methods.

The three erodents, which are characterised in Section 3.5, were then impacted onto WC-Co discs cut from the rear of a PCD compact. The erosion rates are compared in fig. 4.3(a). Of note is the 2.5-3 orders of magnitude higher erosion rate in WC-Co than PCD, which makes the trends in erosion rates very clear. Changing the erodent material and thus increasing the hardness from that of SiO_2 to Al_2O_3 and then to SiC increases the erosion rate of WC-Co in the ratio 1:25:94. For PCD, the same sample that had previously been eroded with SiO_2 in fig. 4.1 was then eroded further with the other two erodents in fig. 4.3(b), with the erosion rates in the ratio 1:5.3:50.

When SiC is used as the erodent on PCD, only 1/50th of the material is required to cause the same mass loss when compared with SiO_2. As a large number of experiments will be performed, SiC was chosen as the default erodent. Over 500 kg was used during the experiments presented in this thesis, which would have required 25 tonnes of SiO_2 for the same mass loss, with environmental, economic and practical reasons justifying the decision switch away from the more commonly used erodent. Caution must be employed when comparing the results of these erosion tests with previous experiments on PCD or other materials which use the more standard erodents, or when interpreting these results for any application which may involve the interaction between PCD and other softer materials.

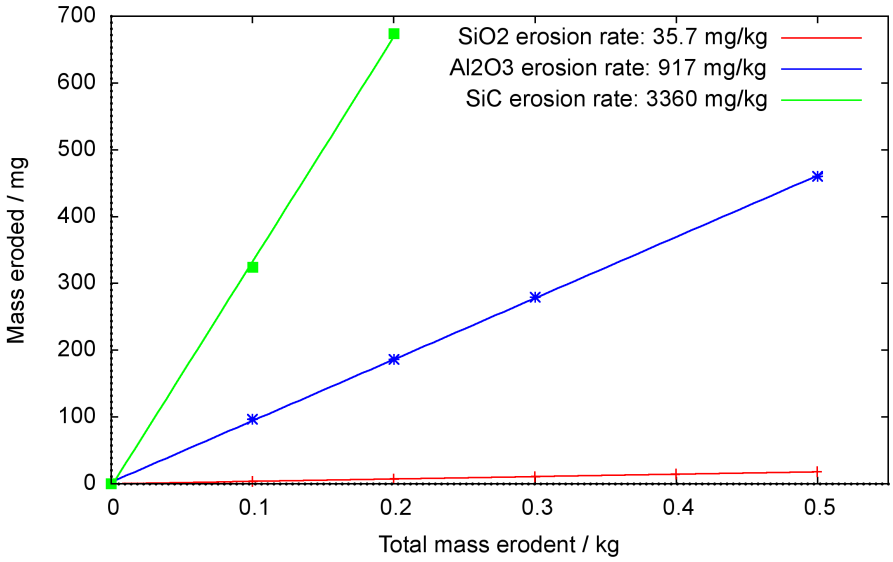

(a) Impacts onto WC-Co.

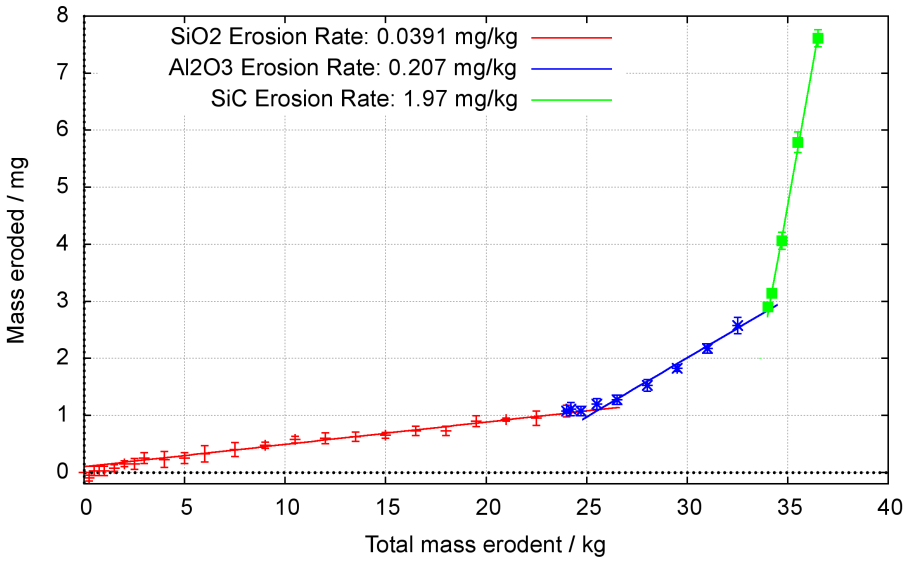

(b) Impacts onto G30 PCD.

Fig. 4.3 A comparison of the response to erosion of WC-Co and PCD discs with the three different erodents - a 525 µm sized rounded SiO_2 sand, and F36 mesh angular Al_2O_3 and SiC. All of the erodents were travelling at as close to 160 $m\,s^{-1}$ on exit of the barrel as was feasible.

4.4 Room Temperature Erosion of PCD

An example of a standard erosion measurement on a sample of G30 PCD which had been lapped flat before being eroded with F36 mesh SiC is given in fig. 4.4, which shows a linear erosion rate other than for the first increment. The unpolished surface does not contain exposed cobalt in the same manner as those eroded in fig. 4.1 as the lapping process preferentially removes cobalt, and in fact the mass lost over the first increment is lower than the long term erosion rate. Generally, the state of the surface post-lapping is variable. Often there may be a thin layer of slurry from the surface preparation processes that has dried onto the sample, or alternatively there may be a network of small cracks or scratches caused by the lapping process. Not all of the SiC deposited on the surface during erosion is removed during the cleaning process which occur after each erosion step (as will be confirmed by SEM images in Section 4.8), and so it is possible that the mass of the sample may be artificially increased by a thin layer of SiC on the surface. Due to the uncertainties involved in the initial erosion increment, the first data point is dropped from further analysis and is not accounted for when calculating the erosion rate.

For a given set of conditions, the erosion rate and its error are calculated by least squares regression using the steady state erosion increments. Typically between five and eight 1 kg increments are performed depending on whether enough material has been removed to obtain a rate with a low error. Due to the limitation on the number of PCD samples, very few repeats were performed, and so although the random error in the measured erosion rate is displayed alongside any result, the true error is likely to be higher because of the different susceptibility of samples sintered at the same time but at slightly different temperatures to wear processes.

Wear of the apparatus, especially the barrel, can alter the erosion rate with time (as previously discussed in Chapter 4, Section 3.3). However, over the course of one erosion run of 8 increments seen here, the erosion rate does not noticeably change with time even despite the high erodent velocity. Thus, there is confidence that the erosion rate can be

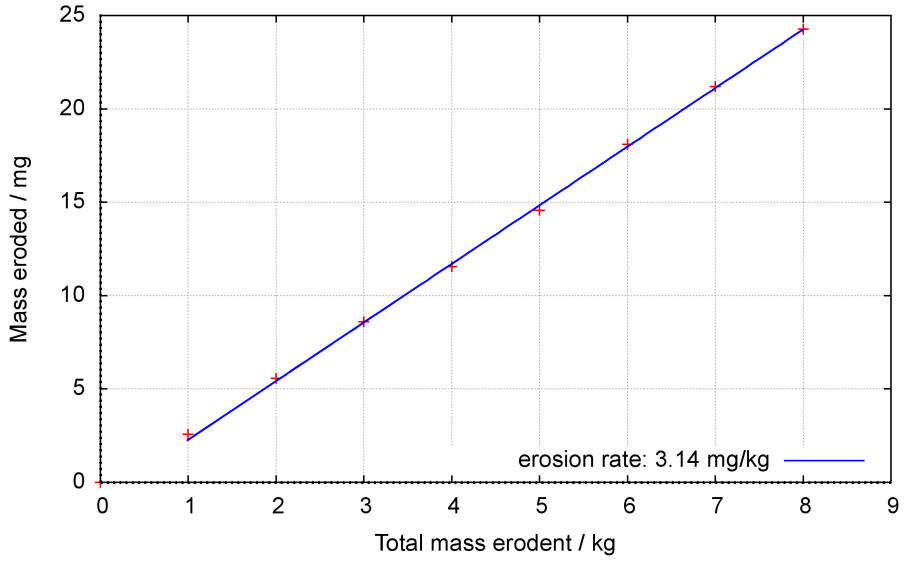

Fig. 4.4 The mass loss of G30 PCD under erosion of F36 mesh SiC at $(155 \pm 9)\,\mathrm{m\,s^{-1}}$ over an area 6 mm in diameter. The erosion rate is given by $(3.14 \pm 0.03)\,\mathrm{mg\,kg^{-1}}$.

meaningfully measured with a low error for a particular stated velocity as long as the velocity is recalibrated between erosion runs.

4.5 The Effect of Grain Size and Reducing the Binder Phase on Erosion Rate

One disc from each of the three grades, G30, G12 & G2, and their RBPCD counterparts, were eroded under the same conditions at a velocity of $95\,\mathrm{m\,s^{-1}}$. Fig. 4.5 shows the long term erosion rates of each grade. The erosion rate was found to decrease with decreasing grain size.

How wear varies with grain size is a matter of some debate, with the wear mechanism playing a key part in the trends that are measured. It has been found by Li *et al* [124] that finer grained PCD wears more quickly when machining Ti6Al4V stacks, whereas Weinert *et al* [125] found that wear of PCD when milling similar materials was independent of grain size. Intra-granular wear mechanisms like those suggested by Lin *et al* [46] indicate that

decreasing grain size should improve wear resistance, for sub-grain sized fractures. Miess & Rai [126] observed that wear resistance of PCD when tested against blocks of granite sharply decreased with grain size increases.

Here, the smaller grain sized material is more erosion resistant and further discussion of the trend is presented alongside SEM images of the surface in Section 4.8.

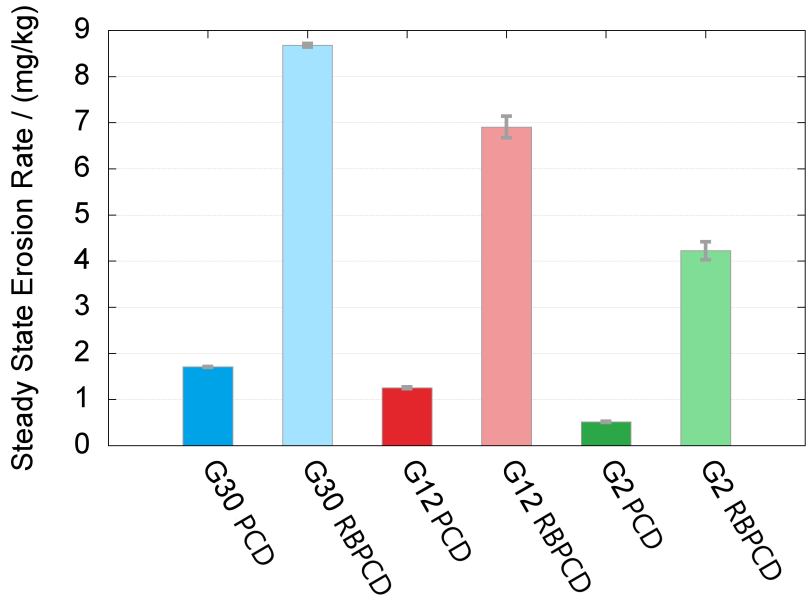

Fig. 4.5 A comparison of the erosion rates of three monomodal grades of PCD and their RBPCD counterparts. The rates were measured for one sample of each type and the error arises from the least squares fit of the erosion rate across 8 increments, or 5 for the RBPCD samples.

It is worth comparing the expected contact area during the interaction of an impacting erodent particle with the surface, assuming a perfectly elastic collision of a sphere on a half-plane. From Hertz's indentation theory [84], the radius of the contact area, a, is given by,

$$a \approx \sqrt[3]{\frac{3RF}{2E}}. \tag{4.1}$$

Inserting appropriate values for the Young's modulus of SiC, E, the radius of curvature of the erodent, R, and the force, F, assuming an elastic rebound and a constant impulse with time, the radius of the contact area, a, is estimated to be 5 µm. The radius of curvature of the erodent will vary due to the angular nature of the erodent particles, and while the most likely impact is on a protruding fine-radiused area, impacts of large-radiused faces are also possible. Due to the brittle fracture of the erodent, which is expected to occur before the maximum contact radius is reached, it is likely that the value for the contact radius will be an over-estimate which limits the validity of this approximation. When compared to the size of the grains within the PCD, the estimated contact radius is far smaller than the 30 µm coarse grains but of a similar order to the finer 2 µm grains. Applying this to the conditions experienced during erosion, an erodent particle impacting a coarse grained PCD is likely to impact only one grain, whereas on impact of a fine grained PCD, many grains may be simultaneously impacted. The interaction area is more likely to contain a region of cobalt in the gaps between the fine grains, which can absorb the energy of the impact and contribute towards a decrease in the overall erosion rate.

Reducing the binder phase has a severe negative effect on the erosion resistance of PCD across all three grades, by a factor of 4.9 in the G30, 5.31 in the G12 and 8.4 in the G2. The removal of cobalt alters the response of PCD to erosion in two ways. Firstly, there is no-longer as much cobalt present in the microstructure to absorb the energy of the impacts. Elastic waves will not be dissipated at the boundaries between the cobalt and the diamond, and the vulnerable edges of diamond grains on the surface become more greatly exposed. Secondly, the residual stresses present in the microstructure are changed. It was found in Section 2.2.4 of the literature survey that, due to the difference in thermal expansion coefficients of diamond and cobalt on cooling from the sintering temperature, removing the cobalt shifts the residual stresses such that the diamond network experiences reduced compressive and greater tensile stresses. The energy barrier to crack nucleation

and propagation thus becomes smaller, increasing the likelihood that an impacting erodent particle will cause fracture and so material removal.

The difference in the ratios between the RBPCD and PCD erosion rates with grain size indicates that reducing the binder content more greatly affects the finer grain sized samples. The larger surface area between cobalt and diamond present in these samples is thought to be the principle reason. However, it is typically more difficult to reduce the binder content in smaller grain sized PCDs due to the increased number of isolated pools and the longer diffusion time that will be required to remove cobalt from narrower capillaries within the diamond skeleton. The mechanism of erosion and how it changes between grades (introduced later in Section 4.8) may also be responsible. The samples tested here have evidently undergone large microstructural changes as judged by the significant change in erosion rates, especially the G2 grade, and the erosion rate remained constant with depth, so incomplete reduction of the binder phase has not been an issue over the depth of erosion studied here.

4.6 The Velocity Exponent

Identifying the relationship between erosion rate and erodent velocity, modelled by the exponent relationship $\varepsilon = Av^n$ introduced in Chapter 3, Section 3.2.4, is a widely performed standard erosion test and will help give information about the wear behaviour of PCD. It will also allow the different grades to be compared and give some insight into whether the erosion mechanism changes across the range of grain sizes studied.

Six PCD discs from each of the three monomodal grades (G2, G12 and G30) were eroded at velocities between $45\,\mathrm{m\,s^{-1}}$ to $160\,\mathrm{m\,s^{-1}}$. Fig. 4.6 shows the response of erosion rate with velocity, with the fitted exponents recorded in table 4.1.

The lowest possible velocity is limited by the lowest flow rate that can repeatably be measured by the laboratory air line, although for the G2 grade a faster velocity was used

PCD Grade	Velocity Exponent
G30	1.13 ± 0.03
G12	1.18 ± 0.03
G2	1.70 ± 0.01

Table 4.1 The velocity exponents and their error calculated from tests on 6 samples of each grade over the velocity range $45\,\mathrm{m\,s^{-1}}$ to $160\,\mathrm{m\,s^{-1}}$ shown in fig. 4.6.

to ensure that the erosion rate was high enough to be measured without a large error. The limitation on the fastest velocity is from the maximum pressure and flow rate that can be obtained from the laboratory compressed air line used to drive the airflow.

The similarity between the exponents of the G12 and G30 grades indicates that similar material removal mechanisms are present, whereas the much higher exponent for the G2 grade suggests that an alternative mechanism may be present. All three exponents are lower than the expected value of $2\frac{2}{3}$ derived theoretically for homogeneous brittle materials, indicating that none of the theoretical models for a brittle material completely describe the complex erodent-PCD interaction.

The most obvious limitation of the Hertzian model is that it includes the assumption that the impactor is an elastic sphere. The angular silicon carbide erodent is non-spherical and is known from images of the fragments (fig. 3.13) to fracture on impact. Further, crack propagation in the PCD is complicated by its biphasal polycrystalline microstructure, whereby the fracture planes in neighbouring grains do not necessarily align, and the cobalt can take on a toughening role and help arrest cracks.

The exponents measured here are within the range of 1.2 ± 0.7 measured by Davies [127] for the impact of silica sand onto single crystal diamond but contrast with the 3.4 ± 0.4 Davies found for erosion of polycrystalline CVD diamond, which does not contain cobalt or bridges between the diamond grains. Although an alternative erodent is used here, the variations in velocity exponent give an indication that the microstructure is important to the mechanism of material removal that this chapter is building towards.

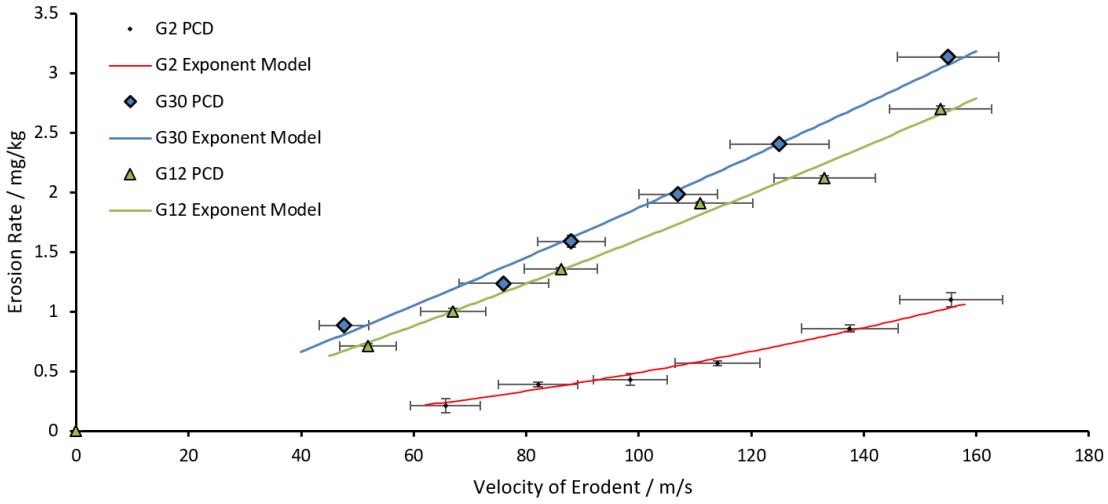

(a)

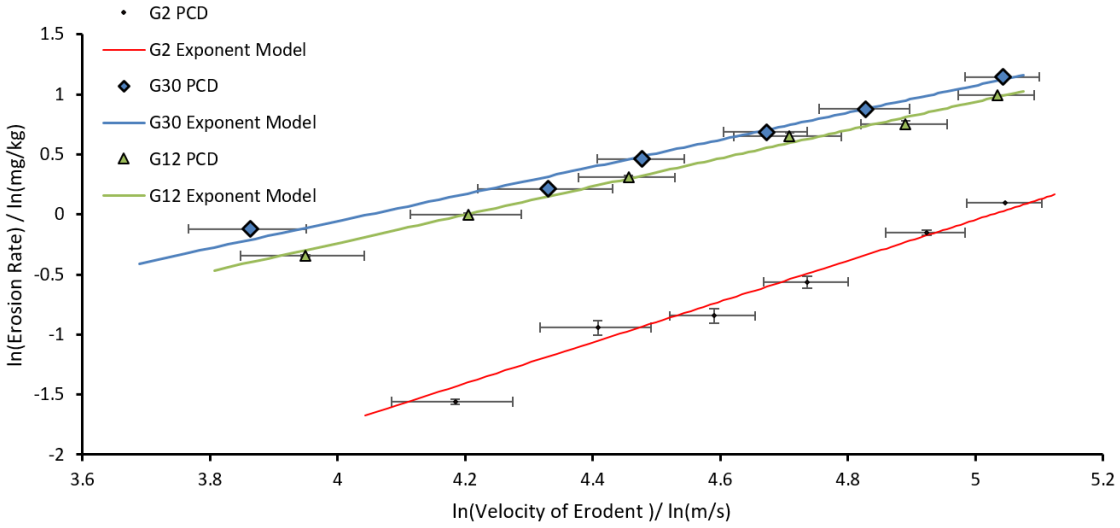

(b)

Fig. 4.6 The response of freestanding PCD discs to altering the velocity of the erodent shown with the raw data (a) and after taking logarithms to identify the exponent (b). The x-error bars represent the spread in erodent velocities, as opposed to the error in the mean velocity which is known to be $< 1\,\mathrm{m\,s^{-1}}$. The y-error bars show the variance of erosion rate over a number of increments on a single sample and so do not account for the variations between individual samples which have undergone the same preparation methods.

4.7 The Effect of Impingement Angle

An experiment was performed to investigate the effect on the erosion rate of changing the angle of impact of the erodent as it strikes the PCD samples. The erosion spot size for normal incidence was reduced to 4 mm in diameter by reducing the width of the barrel to the same size, and the barrel-sample standoff distance was reduced to 15 mm. These modifications were required in order to ensure that as the target is rotated to enable erosion at an angle, all of the erodent still impacts the flat face of the disc and the edges, which are susceptible to higher rates of erosion, remain untouched.

The sample holder was capable of rotating whilst keeping the centre of the disc in line with the centre of the erodent beam. As the erodent exits the barrel, it does not necessarily all proceed in a straight line, and angles of up to 10° away from the axis of the barrel were measured using the high speed video camera during velocity calibration. However, the distribution of the angles was sharply peaked around 0°, in line with the axis of the barrel, so the majority of impacts can be assumed to be at the angle between the barrel and the surface of the sample.

Five G30 samples were eroded at angles between 30° and 90° and the results presented in fig. 4.7 show an increase in erosion rate with angle up to 90°.

A model for the normalised erosion rate ε_0 of

$$\varepsilon_0 = sin(\theta)^{n_2} \tag{4.2}$$

where θ is the angle of erosion was chosen and a fit of least squares found a value of $n_2 = 2.20 \pm 0.07$ for the exponent. The trend shown in fig. 4.7 is typical for the erosion of a brittle material [128], with the highest erosion rate found at normal incidence. The value for n_2 is reasonable given that the energy that the erodent imparts into a surface will reduce as the angle decreases, and so fewer cracks will form resulting in a reduced erosion rate. Mass

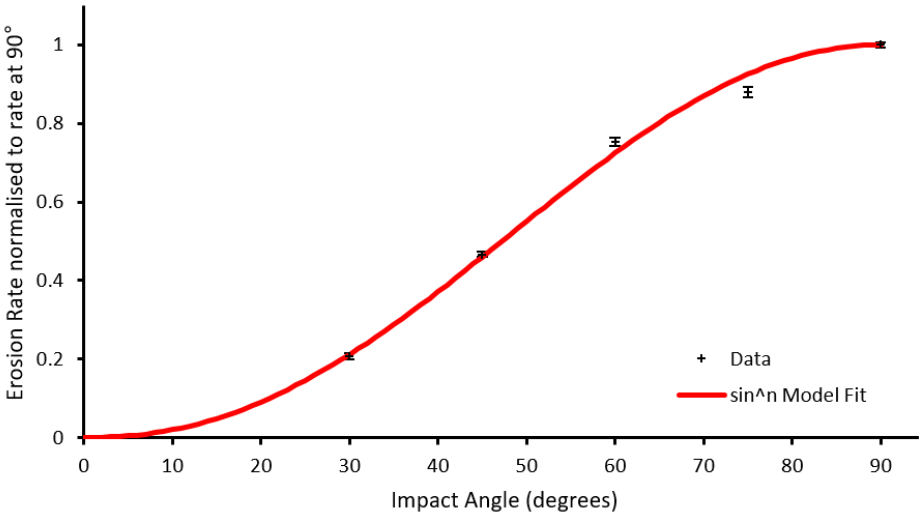

Fig. 4.7 The response of five freestanding G30 PCD discs to altering the angle of the erodent. Y-error bars show the variance of erosion rate over a number of increments on a single sample. The model is a least-squares fit of $y = sin(x)^n$ where $n = 2.20 \pm 0.07$.

loss mechanisms which increase the erosion rate with angle, such as ploughing and gouging, are more prevalent in ductile materials, are not expected to be present here [95].

The eroded surfaces were analysed with a Talysurf probe, capable of scanning across a line on the surface and recording the height at each point to the nearest 1 µm. A needle, tipped with a 50 µm diameter tungsten carbide hemisphere, is placed in contact with the surface, and its deflection is measured as the sample is moved linearly underneath it.

The depth trace for the sample eroded at normal impact is shown in fig. 4.8. Although there is some error in the alignment of the surface, noticeable by the difference in height and slope of the uneroded surface either side of the erosion crater, the Talysurf has been able to show the eroded profile in some detail. The crater is symmetrical in shape due to the symmetry of the normal erodent beam, and its width of 4.4 mm is slightly larger at its deepest points than the 4 mm diameter of the barrel. The potential spreading out of the erodent as it leaves the barrel accounts for some of this increased width.

The shape of the erosion crater, with a flat plateau in the centre surrounded by a ring which is further recessed, is a known phenomenon in erosion [129, 130], although is one

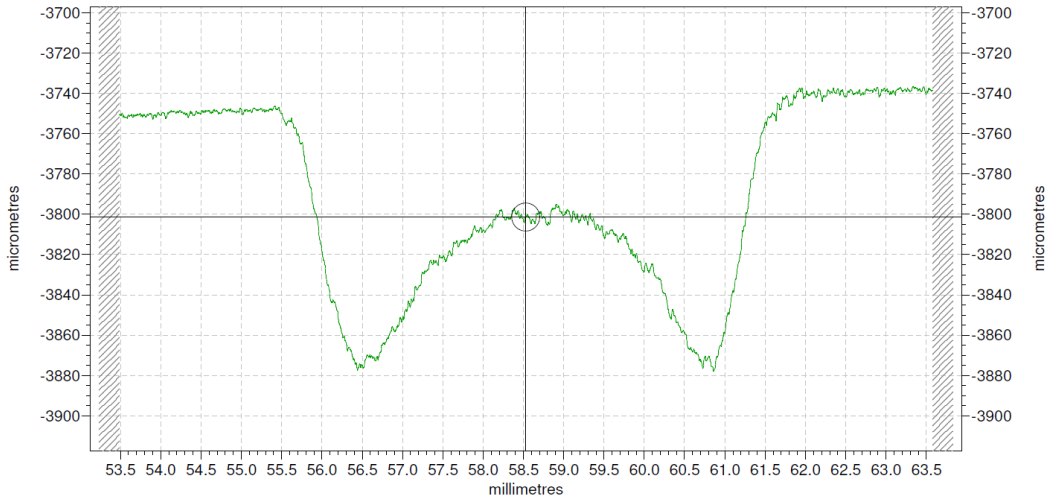

Fig. 4.8 Talysurf trace across a sample eroded with a 4 mm barrel at normal incidence recorded with a 50 µm diameter tip. Note that the x & y axis are scaled so as to accentuate the differences in height.

more often seen in ductile materials. Two reasons for the shape are given. The first is a consequence of the erosion process being more complicated than a single interaction between the erodent and the surface. As a SiC particle impacts the surface, it fractures and the fragments are emitted in a range of directions. Particles that travel nearly horizontally to the surface will impact the side of the erosion crater. As the ring at the edge of the erosion spot becomes lower than the central plateau, particles that impact on an angle become more likely to rebound towards the bottom of the crater, further increasing material removal in this region. The second proposed reason is that the particles at the edge of the erodent beam will have a higher velocity on impact than those in the centre [131]. No evidence of this was found during the velocity calibration, and no similar crater shapes were observed during the erosion of softer targets such as 316 stainless steel or WC-Co, and so it can be assumed to a first approximation that the spread of velocities in the beam is constant across it. The procedure that forms the crater-shape is mostly self-limiting as, once the ring reaches a certain depth, it will become difficult to remove erodent from the ring which will form a barrier to further fracture. The erosion rate still remains constant with time (e.g. fig. 4.4) despite the non-normal impacts that the surface will be subjected to, as the maximum angle

away from normal in the surface studied in fig. 4.8 is only 3.4°, which is shown in fig. 4.7 to be small enough to not make a measurable difference.

The Talysurf trace on the central plateau does show some roughness but the maximum measured peak to peak height is not greater than 10 µm. The large radius of the contact sphere means that a true trace of the surface will not be measured if the recesses are steep enough that the measurement needle does not make contact with the bottom of the valleys on the surface. As such, it is difficult to discern using this particular measurement technique whether the surface roughness is on a length scale comparable to that of the grain size.

A second trace of a sample impacted at an angle of 30° is shown in fig. 4.9. A similar erosion pit shape is seen to before, with a recessed ring around a central plateau, however the ring is asymmetrical due to the angle that the erodent has impacted the surface. The oblique impact has increased the proportion of SiC that has gone on to hit the edge of the pit that is further from the barrel. The area over which erosion has occurred is larger, due to the rotation of the sample, and its size is roughly twice that of the normal impact, which is to be expected for an impact angle of 30°.

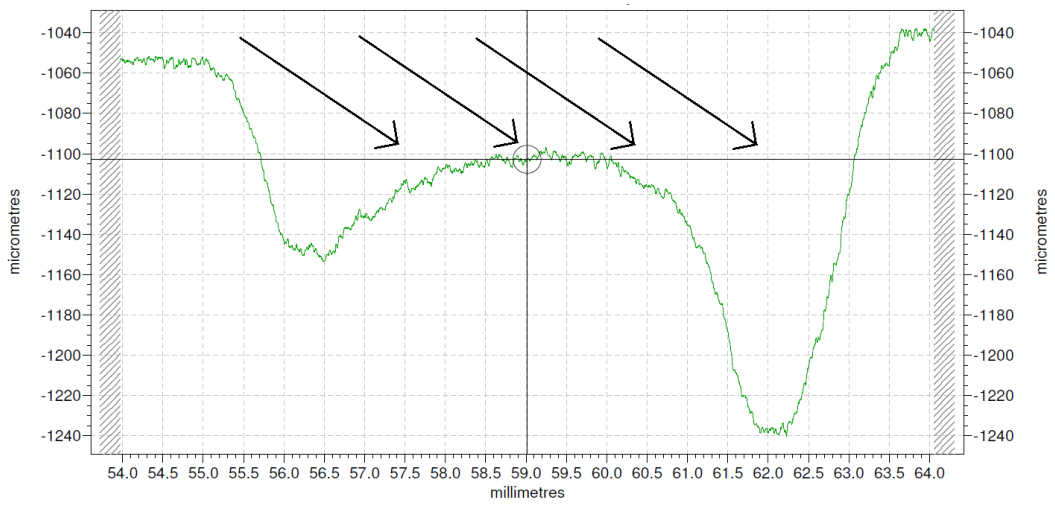

Fig. 4.9 Talysurf trace across a sample eroded with a 4 mm barrel at 30° incidence recorded with a 50 µm diameter tip. The direction of the incoming erodent is in the plane of the trace and is indicated by the direction of the arrows, which are not to scale.

Overall, angled erosion of G30 PCD showed the typical response expected for a brittle material, with the highest erosion rates found when the erodent impacted at normal incidence. Surface profilometry has shown that erosion scars are not flat across their width, with a flat central plateau surrounded by a deeper ring at the edges where secondary phase erosion processes accelerate the wear rate.

4.8 Erosion Mechanism

In the previous two sections, the erosion rate has been measured whilst varying both velocity and angle. The three grades showed different responses to changes in erodent velocity. In this Section, in order to explain why different PCDs respond differently to erosion, a series of SEM images have been taken of eroded surfaces in order to determine the method by which mass is lost.

The Effects of an Ultrasonic Cleaning Treatment

In order to further understand one of the steps the erosion process, and to ensure that the surface that is being studied is comparable between images, images were taken of an eroded G30 PCD both before (fig. 4.10) and after (fig. 4.11) a three minute rinse in an ultrasonic water bath. Before weighing after each erosion increment, the samples are washed in this way, rinsed in acetone and blown dry with compressed air, in order to ensure that the weight intervals are measured repeatably.

It can be seen by comparing the unwashed and washed images that there is a larger amount of SiC present on the surface of the unwashed PCD. During erosion, a layer of SiC is both added to the surface as erodent impacts and adheres but is also removed by further SiC impacts. The thin SiC layer, occasionally described as a ‘tribofilm’, is mostly removed by the washing procedure however will be present during the erosion process and in small parts in recesses on the eroded surface when imaged.

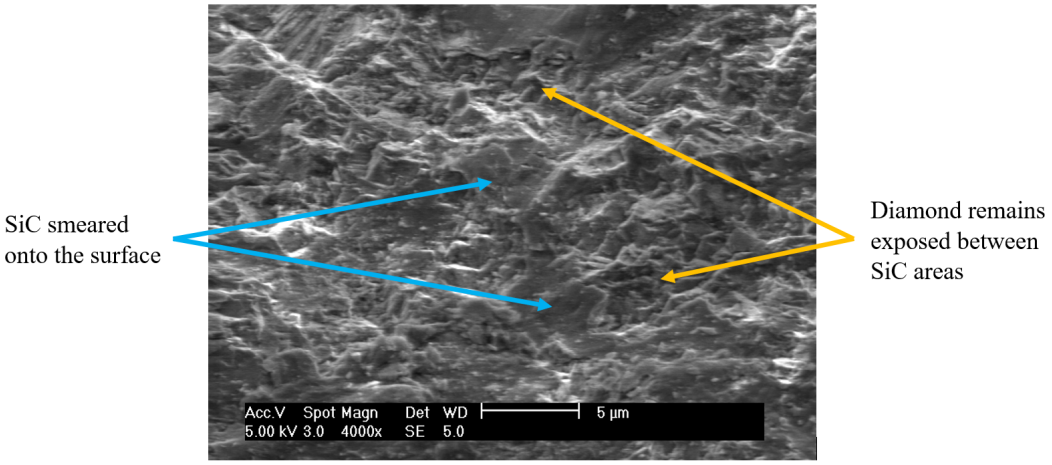

Fig. 4.10 SEM image of G30 PCD taken at an angle of 45°, as removed from the erosion chamber before the ultrasonic rinse. SiC can be seen to coat regions on the surface, concealing the PCD underneath.

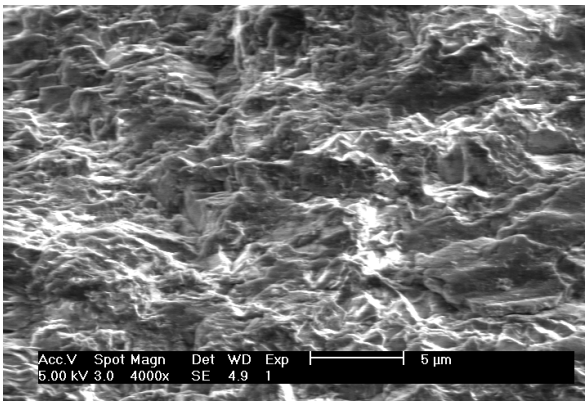

Fig. 4.11 SEM image of G30 PCD taken at an angle of 45°, washed in an ultrasonic bath for 3 minutes before being rinsed in acetone and blown dry. Little to no SiC can be seen on the surface.

Stepwise Erosion from a Polished Surface

In order to establish the method of material removal during erosion, a sequence of SEM images were taken of the same area on the surface of an initially polished sample of PCD at intervals during the erosion process. The technique of step-wise erosion has previously been performed on WC-Co hardmetals by Gant & Gee [132] where it was found that the erosion process involved firstly the removal of the softer cobalt binder followed by pullout of the then unbonded WC grains. It is expected that pullout of the diamond grains in PCD will be significantly more difficult as they are connected together by diamond bridges. However, Kaye [119] proposed that the fracture of these bridges was the mechanism by which mass was lost from the diamond skeleton in PCD.

Fig. 4.12 shows how the surface of G30 PCD changes during the initial erosion steps. Between the first and the second images, an erosion increment of 0.5 g of F36 mesh SiC, in contrast with the usual increment of 1 kg, was performed. Despite a very small number of impacts, there are clear signs of cobalt removal where it has been extruded out from between the grains. The dimensions of the cobalt pools are small, of the order 1 µm to 5 µm, and so for cobalt to be removed either a direct hit with the sharp end of an erodent particle is required, or secondary impacts of finer erodent particles that have fractured off larger pieces during the initial impacts must cause cobalt extrusion. It seems likely that secondary impacts from finer SiC particles are causing the cobalt extrusion.

By the third image, another 1.5 g of erodent has impacted the sample and even at this early stage in the erosion process small amounts of diamond have been removed from the exposed edges which surround where the cobalt pool used to be. Fractures smaller than 1×1 µm are seen in a jagged shape, indicating that a number of small fractures have caused material removal. The prevalence of fracture near exposed edges is well documented in both CVD diamond [127] and in single crystals [60] so it should not be surprising that preferential

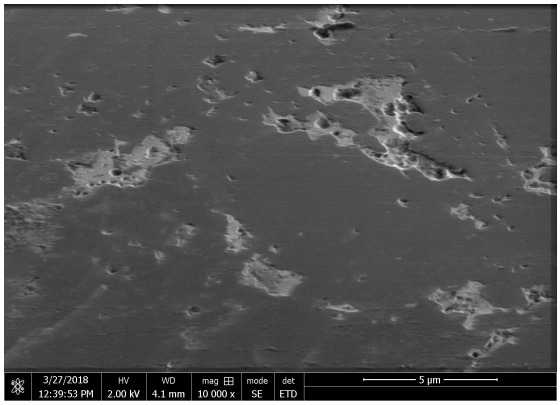

(a) A polished surface of G30 PCD at 10000x magnification and an angle of 52°.

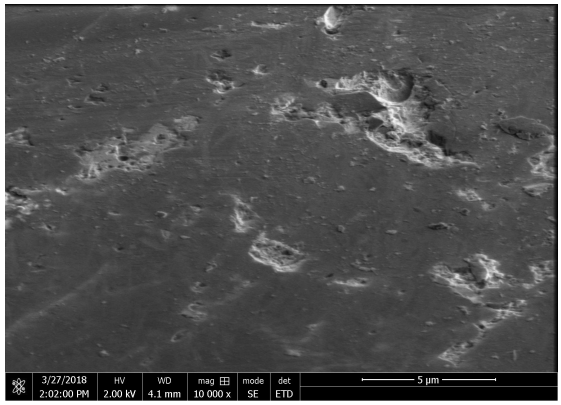

(b) The same surface after impact with $0.79\,\mathrm{g\,cm^{-2}}$ of 525 µm SiC particles.

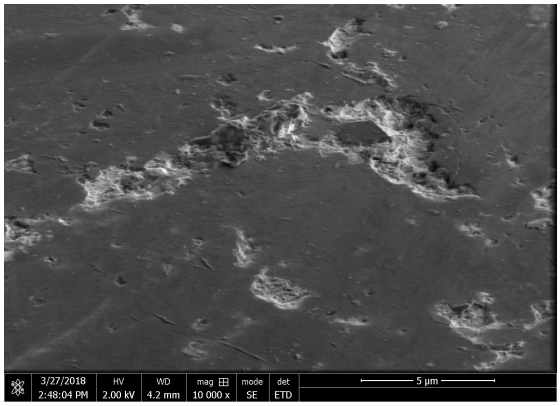

(c) After impact with a total of $2.36\,\mathrm{g\,cm^{-2}}$ of 525 µm SiC particles.

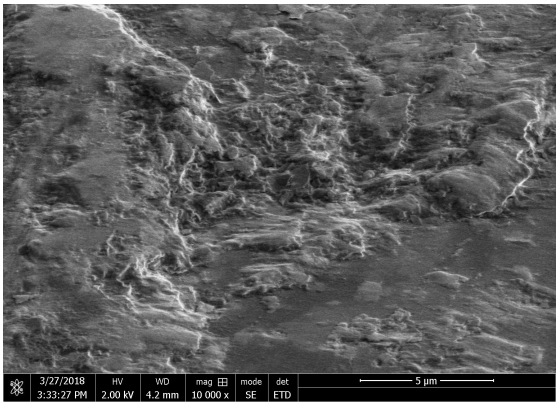

(d) After impact with a total of $14.93\,\mathrm{g\,cm^{-2}}$ of 525 µm SiC particles.

Fig. 4.12 SEM Micrographs of an initially polished surface of G30 PCD taken at intervals throughout the erosion process. The erodent impacted at $(83 \pm 6)\,\mathrm{m\,s^{-1}}$. The sample was tilted to 45° in the SEM to help show the topography. Regions of cobalt show up as lighter colours, with diamond the darkest. SiC introduced in images (b)-(d) has a medium contrast.

material removal occurs here. Some SiC has not been removed by the ultrasonic rinse and is seen to stick to the surface.

On further erosion, in fig. 4.12(d), there is significantly more SiC adhesion to the surface than on an eroded surface (fig. 4.11). The major difference between the near-polished and the as-eroded surfaces is the surface roughness. The flat diamond grains seem to help SiC adhesion resulting in build up of a surface coating. The surface coating also makes relocation of the images in the SEM more difficult preventing further tests. Even despite the SiC build up, it can be seen that erosion is enlarging the pit where originally there was a small cobalt pool and removing diamond where there were originally exposed edges whilst leaving the polished flat centres of grains undamaged.

Erosion from a Previously Eroded Surface

As the polished surface tended to become obscured by SiC deposition, but it was known that eroded surfaces suffered less from this issue, stepwise erosion was performed from a previously eroded surface. Despite laser engravings around the edge of the PCD disc, designed to aid with re-location of the same area in the SEM, finding the same features repeatably in the field of view proved to be challenging as even after just a small amount of erosion, the surface became barely recognisable.

To facilitate re-location at the same area in the microscope, a square well, $30 \times 30\,\mu m$ in section and $30\,\mu m$ deep, was milled into the surface with a focused ion beam (FiB). Even at low magnification, the well could be easily located and used as a reference from which local features could be identified and re-imaged. The sides of the well represented regions where preferential erosion could occur, due to the exposed edges, so features were observed far enough away from the well such that the well did not affect the region of study.

The pair of images shown in fig. 4.13 shows the surface of G30 PCD after a very small quantity (1 g) of erodent had impacted at a moderate speed. Within the orange circle, a chip of $1 \times 1\,\mu m$ in profile size has been removed from a protrusion during the erosion increment.

This chip is an example of preferential material removal at an edge and on a protrusion above the surface, which is more likely to be hit by impacting erodent. The recess designated by the blue arrow has remained unchanged by the erosion increment, however the region immediately above it becomes unrecognisable as a $5 \times 5\,\mu m$ sized region has been fractured and removed. Within the green ring, it was confirmed by EDX spectroscopy that a region of SiC had been deposited on the surface, explaining the large change in contrast between the images.

Stepwise erosion of G30 PCD has showed that the principle mechanism of mass loss is the formation of small chips and microfractures with preferential erosion occurring at exposed edges or protrusions. It also shows that, in a similar manner to Gant & Gee's research on WC-Co [132], typical erosion processes such as the formation of Hertzian cone cracks and the creation of radial cracks are not responsible for mass loss in this grade of PCD. The difficulty of surface relocation after erosion increments helps support the proposed material removal mechanism as a large number of small fracture events will change the shape of the features on the surface very quickly, making comparisons after any larger erodent increments difficult.

Grain Size Effects on the Eroded Surface

Previously in this chapter, erosion mechanism studies have focused on the G30 grade due to the more easily measurable erosion rate, however it is thought from the comparison of velocity exponents that the G2 grade may wear by a different mechanism. The three monomodal grades (G2, G12 & G30) were each eroded at $(84 \pm 4)\,m\,s^{-1}$, $(132 \pm 8)\,m\,s^{-1}$ and $(160 \pm 10)\,m\,s^{-1}$ and their surfaces were imaged in the SEM so that they could be qualitatively compared, shown in fig. 4.14.

At the lowest velocity, HCCs (introduced in the discussion of erosion in Section 3.2.1) are visible on the surface of the G2 sample. They are small, typically less than $150\,\mu m$ diameter, and run for less than 120° of arc. On the G12 and G30 surfaces impacted at the

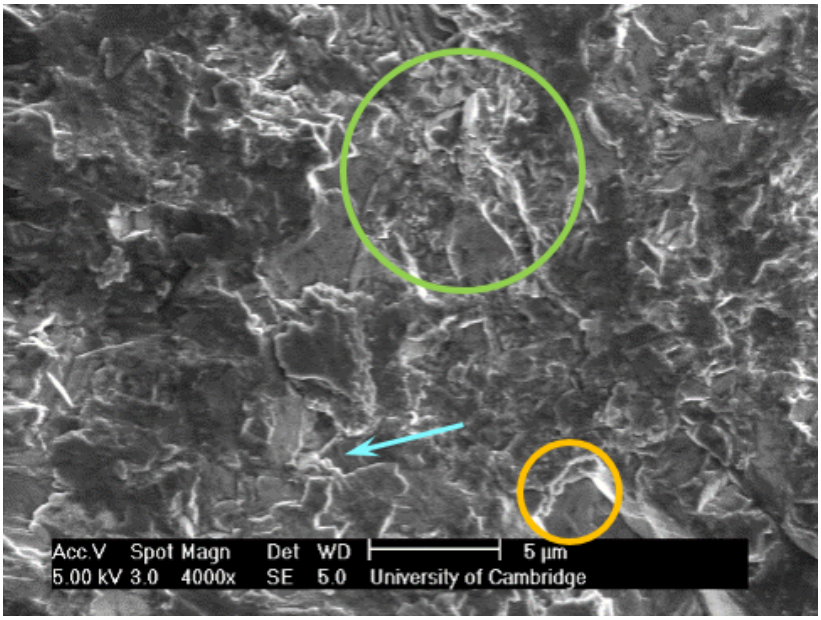

(a)

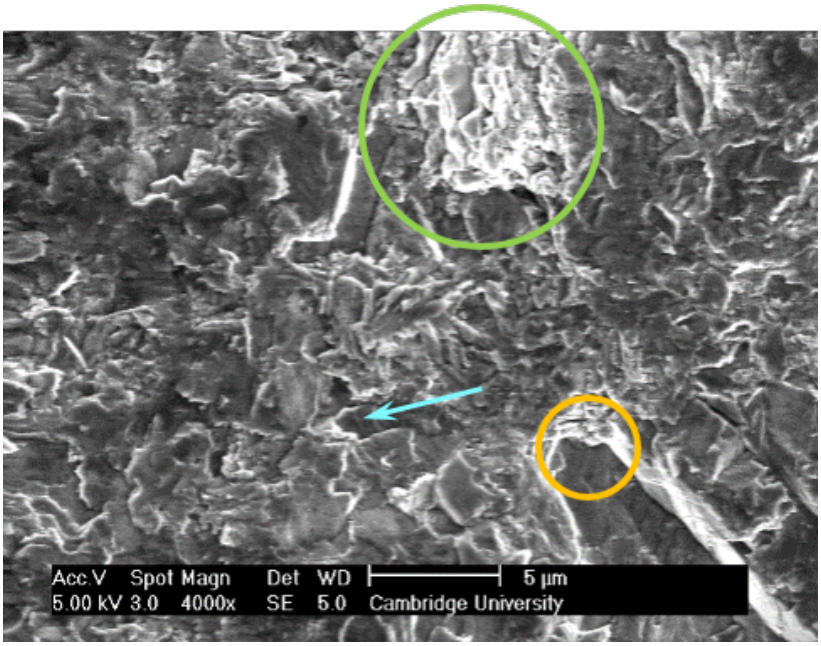

(b)

Fig. 4.13 SEM images of the same surface of G30 PCD, relocated using a proximal FiB-milled well, taken at normal incidence both before (a) and after (b) a 1 g increment of erosion at $(98 \pm 7)\,\mathrm{m\,s^{-1}}$. Features have been marked and are discussed in the text.

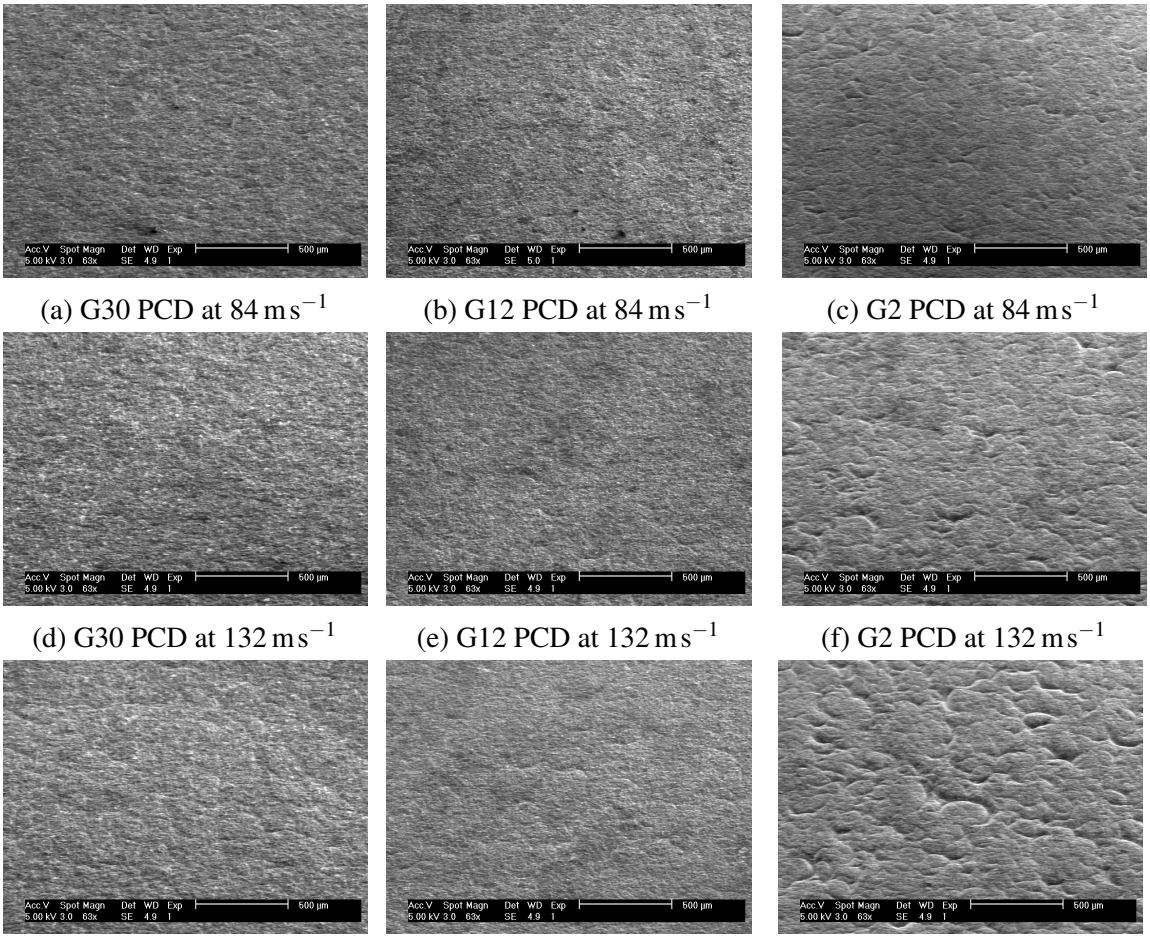

(a) G30 PCD at 84 m s^{-1} (b) G12 PCD at 84 m s^{-1} (c) G2 PCD at 84 m s^{-1}

(d) G30 PCD at 132 m s^{-1} (e) G12 PCD at 132 m s^{-1} (f) G2 PCD at 132 m s^{-1}

(g) G30 PCD at 160 m s^{-1} (h) G12 PCD at 160 m s^{-1} (i) G2 PCD at 160 m s^{-1}

Fig. 4.14 A series of SEM images taken at the same angle (45°) and scale showing the relative distributions of Hertzian Cone Cracks on each grade after erosion at a range of velocities.

same velocity, the same curving features, with deep (5 µm or larger) recesses in the surface are not seen. Further, when disregarding the HCC features, the surface roughness varies between the images, with the G30 the roughest and the G2 the smoothest.

As the erodent velocity increases, the diameter and arc angle of the HCCs on the G2 surface increases. The cracks become more pronounced, and more dense. In the G12 grade, a few HCCs can be seen at $160\,\mathrm{m\,s^{-1}}$, but less clearly than any of the G2 surfaces. The G30 surface appears to have a higher roughness than at lower speeds, and there is some evidence that HCCs are present however they are not deep and are difficult to see or measure above the noise of the surface roughness.

Eroded Surfaces in Section

To analyse the crack patterns further, one sample of each grade after erosion at $160\,\mathrm{m\,s^{-1}}$, was sectioned by milling a well using a FiB and imaging at an angle in an SEM. A layer of platinum was deposited on the eroded face to preserve the top surface on milling. The high strength of the sp^3 carbon-carbon bonds in diamond and the comparatively weakly metallic bonded cobalt results in regions of PCD with different resistances to ion-beam milling. As a consequence, a phenomenon known as 'curtaining' occurs [133], which is indicated on the SEM images, whereby vertical striations are introduced onto the surface. Although efforts have been made to minimise curtaining artefacts by repeated polishing of the PCD section, some remain present in the images.

A section through a HCC located on the surface of a G2 PCD sample after erosion at $(160 \pm 10)\,\mathrm{m\,s^{-1}}$ is shown in fig. 4.15. The crack extended deeper into the material than the 25 µm depth of the FiB-milled well and was mostly straight and over 1 µm wide, which indicates that it is not changing direction to preferentially pass through grain boundaries or bridges. The HCC is filled with debris from the milling procedure which explains its colour, and is similar to that seen by Lawn during repeated impacts onto SiC shown in fig. 3.3. The large HCC arises from a large number of impacts causing incremental crack opening. The

fracture passes through a number of cobalt pools as it propagates, which will help absorb the energy of impacts.

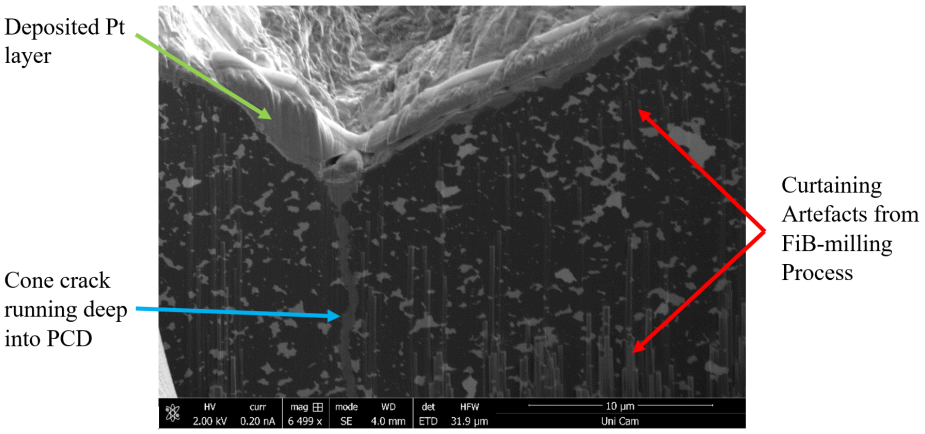

Fig. 4.15 FiB-milled SEM image of a section of G2 PCD eroded at 160 m s^{-1}. The wide HCC runs deep into the material, further than the 25 µm mill depth. It is filled with amorphous milling residue, hence the colour.

The crack seen in the G12 sample (fig. 4.16) is significantly thinner than found in the G2 grade and propagates less far into the surface. The role of cobalt in the fracture process is clear as the crack diverts in one cobalt pool, bifurcates in a second and terminates in a third. The varying crack trajectory combined with the action of the cobalt and the vast number of impacts during erosion indicates that HCC extension could occur by sequential 'jumps' between cobalt pools, which are shorter and thus easier to initiate in the smaller grain sized G2 sample, explaining the higher prevalence of HCCs.

Increased magnification images of the PCD closest to the surface for all three grain sizes are given in figs. 4.17, 4.18 & 4.19. Consistently between all three grades, there are regions of up to 3 µm in length over which small fractures, of up to 2 µm propagate down into the bulk of the PCD. The estimated value for the contact radius (from Equation 4.1) of 5 µm is very similar to the horizontal scale of these fractures. It is difficult to determine whether these fractures are more prevalent at grain boundaries or within diamond grains as the two phases of diamond are indistinguishable under SEM.

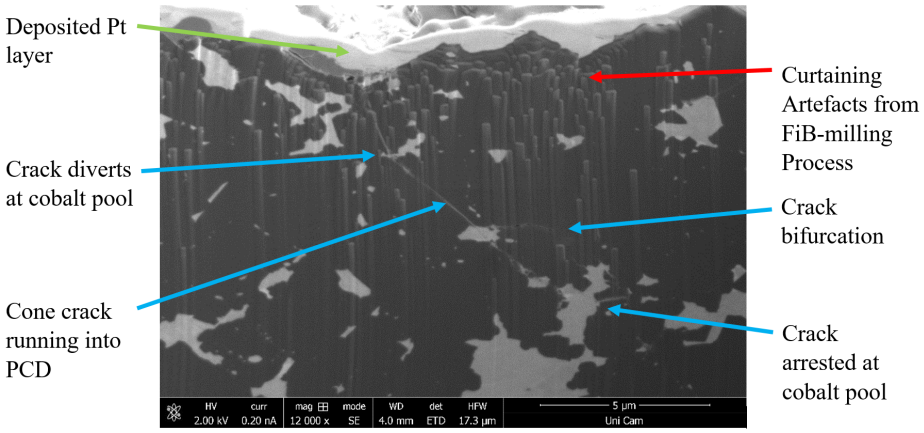

Fig. 4.16 FiB-milled SEM image of a section of G12 PCD eroded at 160 m s^{-1}. The HCC runs into the material, diverts through a cobalt pool, bifurcates in another cobalt region, and then is arrested in a larger pool of cobalt.

Proposed Material Removal Mechanism

The predictive erosion theories in Chapter 3, Section 3.2.4, calculated the quantity of material that would be expected to be removed from either the intersection of Hertzian Cone Cracks or radial median and lateral cracks. SEM analysis of eroded surfaces has shown that the interaction between the erodent and the PCD is more complicated than would be expected from assuming the ideal case used by modellers. The polycrystalline biphasal microstructure of PCD prevents standard radial median and lateral cracks from forming, and diamond's preference to fracture along certain planes may influence the dynamics of crack propagation.

The primary mass loss mechanism in the coarser G30 grade has been determined by stepwise erosion to be sequential microfractures causing microchipping, with a prevalence for exposed edges or protrusions on the surface. Sectioned views of the surface further confirm this method by revealing that the locations of cracks are limited to the region very close to the surface and that regions smaller than the grain size are removed. The fact that very small amounts of erodent could drastically change the view of the surface to the point where it became nearly unrecognisable is a further indication that damage is built up from a large number of smaller fractures. There was evidence found by Hibbs & Lee [68] for

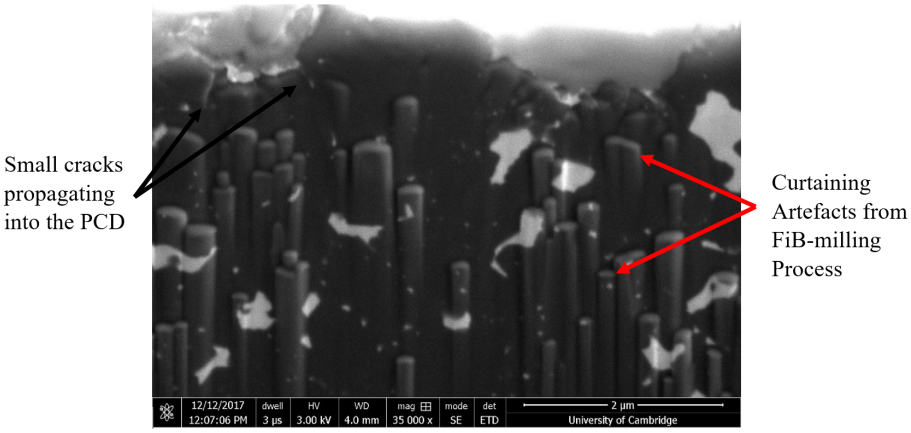

Fig. 4.17 Section of G2 PCD after erosion at 155 $\mathrm{m\,s^{-1}}$. Despite the extensive curtaining artefacts, formed during the FiB-milling process, a small quantity of cracks extending downwards from the surface can be seen. The cracks typically extend less than 1 µm from the surface.

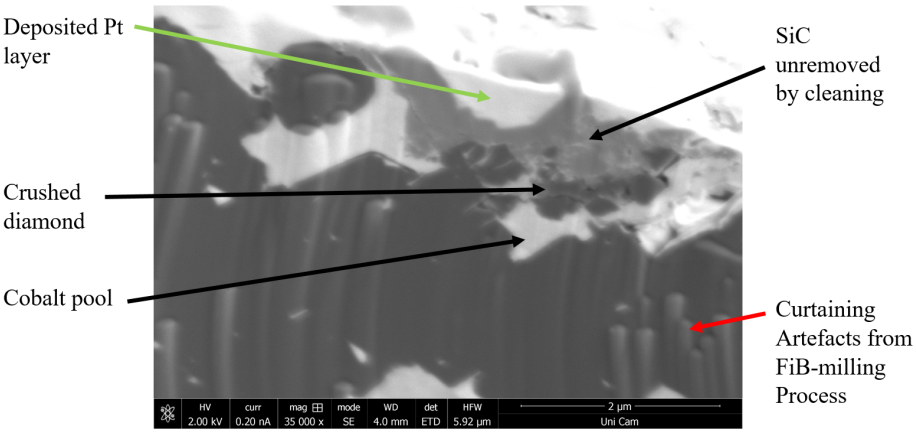

Fig. 4.18 Section of G12 PCD after erosion at 160 $\mathrm{m\,s^{-1}}$. Here, a SiC particle has impacted and crushed diamond, forming lots of small particles. This crushing is prevented from continuing further into the material by the presence of a cobalt pool. The curtaining artefacts are curved due to drift during image collection.

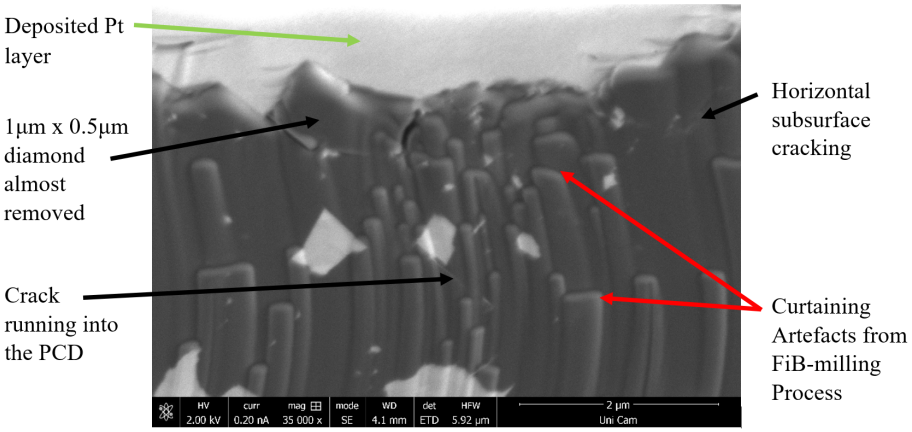

Fig. 4.19 Section of G30 PCD after erosion at 160 m s^{-1}. A crack extends downwards into the surface to a depth of 3 µm. 0.5 µm down, it intersects another crack, showing how material can be removed during erosion.

fractures on a length scale smaller than the grain size of the PCD when milling sandstone with very coarse grained (100 µm) PCD.

The microchipping mechanism can explain why the G12 and G2 samples, where small scale microchipping was also observed, produced lower erosion rates. During crack propagation in PCD, there is a chance that the crack will encounter a region of cobalt at the edge of a diamond grain, with the chance being increased as the grain size decreases. In the smaller grain sized material, a much higher proportion of cracks will be terminated in a cobalt pool, reducing the chances that they will intersect with other cracks and cause material removal. As the typical fracture size is under 2 µm, it is reasonable that the erosion rate of the G12 samples is very similar to the G30, whereas the rate for the G2 is significantly lower.

Using the images presented here, it has not been possible to determine whether there is preferred erosion at grain boundaries, as both the original diamond grains and the bridges between them cannot be distinguished under secondary electron mode SEM.

HCCs were observed in a significantly higher density in the G2 PCD grade, while the radius, arc angle and prominence all increased with erodent velocity. During HCC formation described in Section 3.2.1, it was discussed how the initial stage involves forming a ring crack around the surface, followed by subsequent ‘pop-in’ to form a ring at depth. Very

few complete rings were formed, which is thought to be due to the low energy involved in each erodent impact. However, cracks were seen to propagate to some depth, which is due to incremental increases in size of the crack due to a large number of impacts. Cone crack formation investigated by Marro *et al* [62] found that for the same indentation force, a finer grade of PCD would have a continuous ring crack whereas a coarser grade contained lots of smaller contiguous partial cracks. There is an energy barrier which must be overcome to propagate a cone crack down into a material. Without terminating within a diamond grain, which is unlikely due to the low toughness of diamond, the smallest possible distance that a crack can stably propagate is to the next cobalt pool, wherein the cobalt can plastically deform and absorb further energy. In the G30 grade, a cone crack must propagate of order 30 µm to get to the next cobalt pool, whereas in the G2 grade, it must only propagate across of order 2 µm of diamond, which will be accompanied by a correspondingly smaller energy barrier. During each of the many impacts on any one region over the course of an erosion increment, the chances of HCC propagation in the G2 sample is relatively high, due to the low energy barrier, whereas the chances of HCC propagation in G30 is very low, preventing HCCs being formed at a rate greater than material is removed by the more dominant microchipping mechanism.

The shapes of the HCCs on the surface of the G2 are a consequence of two effects. Firstly, as the HCC propagates downwards into the bulk of the PCD, the material on each side of the crack will rub against each other, widening the crack. Secondly, once a HCC has been formed, it acts like an exposed edge. It is well known that exposed edges are particularly susceptible to fracture on a number of length scales [60]. Preferential erosion at these exposed edges around each crack forms a prominent plateau in the centre which curves away near the crack where more material has been removed and explains the features visible on the eroded surfaces.

To summarise, two separate crack formation mechanisms are present in the diamond network. Small microfractures, typically shorter in length than the size of the grains, propagate down from the surface before intersecting and causing sub-grain sized pieces of diamond to be removed. Larger HCCs span across multiple grains and can penetrate deep into the material. Microfractures are present in both coarse and fine grades of PCD, whereas HCCs are much more prevalent in the finer grade. As the erosion rate is faster in the coarser G30 grade, it can be deduced that the sub-grain sized fractures contribute more significantly to the erosion of PCD, and thus are the dominant mass loss mechanism during erosion.

The erosion mechanisms in the RBPCD samples have not been studied in as much detail as the PCD, primarily due to the difficulty of imaging in an SEM due to the lack of electrical conductivity. However, the mechanisms described above are still applicable to explain the variations in erosion rate. Although not measured, the expected change in residual stresses on reducing the binder phase will decrease compressive stresses in the diamond and help nucleation and propagation of fractures. Reducing the binder phase will remove the toughening role of the cobalt within the microstructure and reduce the likelihood of fracture termination. The ductile cobalt plays a role in energy absorption, without which more energy will be put into the diamond skeleton, increasing the likelihood and size of any fractures forming and helping to explain the higher erosion rates recorded for RBPCD samples in fig. 4.5.

4.9 The Effect of Erodent Size

In order to further probe the erosion of PCD, both a larger (F12 mesh, 1.4 mm to 1.6 mm) and a smaller (F120 mesh, 125 µm to 150 µm) SiC erodent were impacted onto G2 and G30 PCD. Fig. 4.20 shows that the morphologies of the erodents are similar.

To retain sensible erodent flux rates, the particulate feed system required modification. As the larger erodent would become jammed within the hopper, the hopper was replaced by

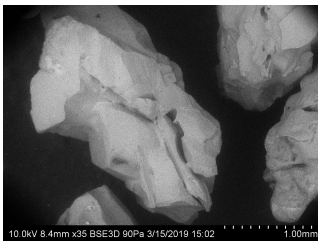

(a) F12 mesh SiC.

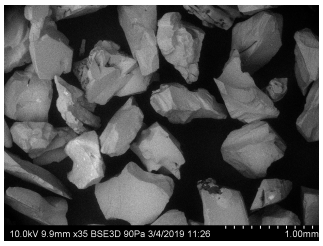

(b) F36 mesh SiC.

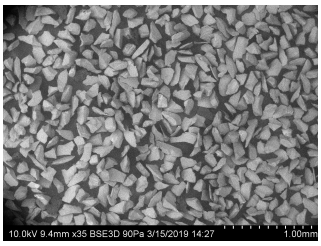

(c) F120 mesh SiC.

Fig. 4.20 Backscattered SEM images taken at the same scale of the three different sized SiC erodents used in this Section.

a flexible tube with a ball valve at each end. The tap nearest the airflow was closed while erodent was added through the open tap at the top. To add erodent to the airflow, the positions of the taps were reversed and SiC dropped into the airflow under gravity. If the erodent were to jam, a small amount of air was released from the top tap providing contraflow which would disturb the erodent and enable flow to be resumed. For the smaller erodent, a constriction was placed between the hopper and the airflow which reduced the flux of the more free-flowing particles.

When impacting the coarse F12 erodent onto G2 PCD discs, it was not possible to find a set of conditions under which steady state erosion would occur due to the catastrophic failure of the sample. After just a handful of impacts (in one case as few as 1000) at a velocity of $(93 \pm 6)\,\mathrm{m\,s^{-1}}$, fractures would propagate through the depth of the PCD disc and break it into more than one piece. From then, exposed edges would preferentially fracture and cause high mass loss and damage to the sample holder behind. Here, the low fracture toughness of the fine grade PCD has been confirmed.

The surface of a G30 grade PCD after experiencing 500 g of the coarse F12 erodent is shown in fig. 4.21. Here, a large crack network has formed in the centre of the erosion spot due to the large impulses present with each of the impacting erodent particles. G30 samples typically survived much longer than G2 samples but also eventually fractured, which was very rare during erosion with the standard F36 erodent.

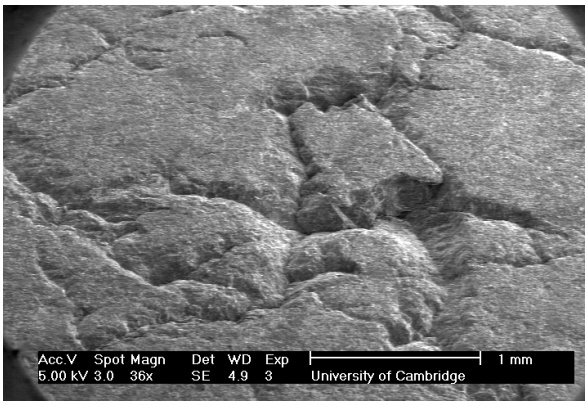

Fig. 4.21 Low magnification image of G30 PCD eroded with 500 g of F12 mesh SiC at $(93 \pm 6)\,\mathrm{m\,s^{-1}}$.

In some regions on the surface of the G30 sample, HCCs were visible. Fig. 4.22 shows the development of a pair of HCCs as more erodent impacts the surface. In alignment with the proposed mechanism of material removal during erosion discussed above, PCD in the regions around the cracks is removed from where there are exposed edges due to the preferential crack formation here, making the HCCs more pronounced. It should not be surprising that the larger erodent which causes a larger impulse can initiate HCCs in the G30 grade where the smaller erodent could not, as its higher energy is more likely to overcome the energy barrier to HCC 'pop-in'.

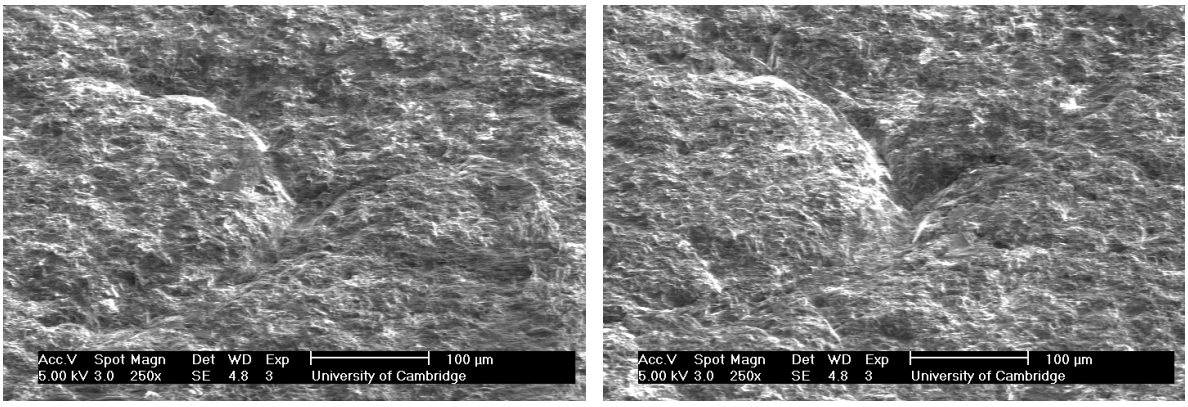

(a) (b)

Fig. 4.22 SEM images of the same region on a G30 surface during erosion taken at an angle of 45°. Image (b) has endured a further 250 g of F12 SiC impacting at $(93 \pm 6)\,\mathrm{m\,s^{-1}}$ over an area of 6 mm in diameter than image (a).

The surfaces after erosion with the finer F120 grade of SiC are also as expected (fig. 4.23). Both are smoother and there is no sign of any HCCs on the G30 surface while small cracks can be seen in the G2.

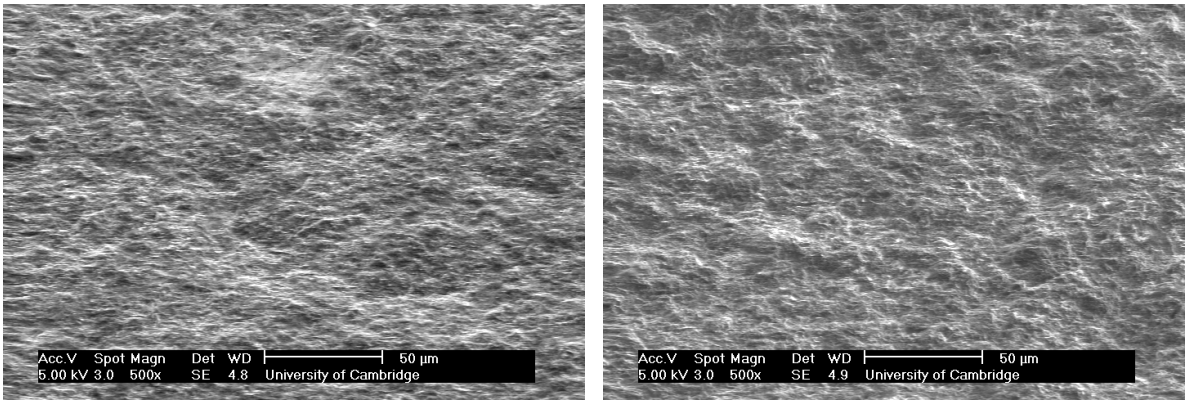

(a) G2 PCD (b) G30 PCD

Fig. 4.23 SEM images of a fine and a coarse grade of PCD after erosion with F120 mesh SiC at $(163 \pm 15)\,\mathrm{m\,s^{-1}}$ taken at an angle of 45°.

Erosion with different sized erodents is consistent with the previously proposed mass removal mechanism and confirmed that the standard F36 SiC erodent is appropriate for erosion testing of PCD.

4.10 Summary and Conclusions

The erosion rate of PCD has been measured under a number of different conditions. Silica sand was found to cause very little erosion, and so SiC was chosen to produce wear rates that could be compared between samples. Decreasing the grain size was found to decrease erosion rate, and the change in velocity exponent implied that different material removal mechanisms may be present in the different grades. Reducing the binder phase was found to severely decrease erosion resistance, while varying the angle of impact showed a typical brittle response in G30 PCD.

A detailed electron microscopy study showed that the primary mechanism of mass loss during erosion was the accumulation of a number of microcracks and the removal of very

small amounts of surface, with a preference for mass loss at exposed edges or protrusions on the surface. HCCs were visible on the surface of the finest G2 grade and a mechanism for why they were not formed in on the G30 surface was put forward. Erosion with larger erodent caused widespread fractures that propagated through the entirety of the PCD discs and caused macroscopic failure, while a smaller erodent resulted in smoother wear and a reduction in HCCs formed.

Chapter 5

Solid Particle Erosion as a Wear Test for PCD

5.1 Introduction

In Chapter 4, the response of three grades of PCD to erosion was studied by varying the erosion parameters. In this chapter, the properties of the PCD targets will be changed and the different responses will be compared under fixed erosion conditions. Here, SPE is used as a method to simulate wear to further understand PCD as a material, and to give information on how to improve PCD's performance in erosive applications.

The chapter contains two sections, the first focuses on how sintering conditions effect erosion rate, while the second conducts a study of how heat treatments affect PCD's response to an erosive environment.

5.2 The Effect of Sintering Conditions on Erosion

5.2.1 Introduction

As described in Section 2.2.1, PCD manufacture involves increasing the pressure and temperature until the constituent materials are in the diamond stable region of the carbon phase diagram and hotter than the cobalt melt line. The process requires complicated apparatus and a significant amount of energy to perform. As the pressures and temperatures become more extreme, the price of each PCD compact increases. Thus, an understanding of how the physical properties are affected by sintering conditions is useful to manufacturers of PCD.

It was found during the literature survey in Section 2.3.1 that sintering conditions are known to affect wear rate during a grinding test and so it is to be expected that the erosion rate may also be affected. Sintering conditions are also known to affect residual stresses, which could further alter erosion behaviour.

5.2.2 The Samples and the Experimental Procedure

In contrast to previous experiments in this thesis, the samples which were tested here were manufactured using a multimodal grain size distribution. The largest grain size in the feed was 22 µm and there were a number of medium sized grains in the 10 µm region with the smallest at 2 µm. The advantages of a multimodal grain size distribution include combining the toughness from the larger grains with some of the abrasion resistance of the smaller ones, and an increased packing density during sintering which results in a larger weight fraction of diamond and less cobalt in the resulting microstructure. To what extent these changes effect the erosion rate and process will be analysed in this Chapter.

The sintering temperatures and pressures of the samples are shown in fig. 5.1. Although pressures are measurable reliably and with minimal error, the temperatures during sintering

are measured by a thermocouple located near to the capsule containing the PCD within the sintering apparatus. Thermal gradients are known to occur during manufacture and as such, the temperature measured by the thermocouple and that experienced by the sintering PCD may indeed be different. It would be safe to assume that the error in the absolute temperature could be as high as 100 °C, however that the errors in the sintering temperatures relative to each other are expected to be lower.

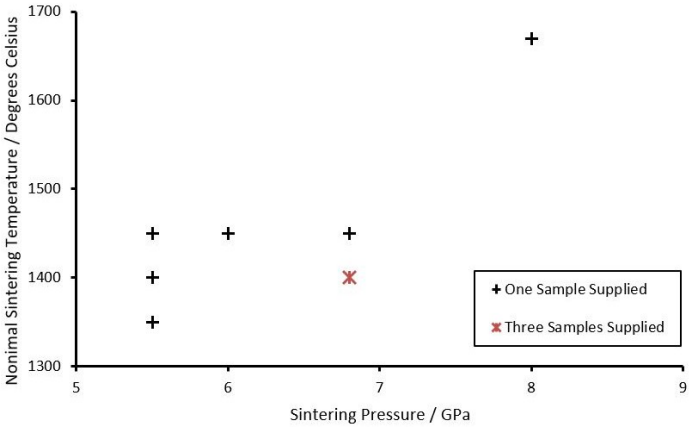

Fig. 5.1 Nominal sintering conditions of the supplied samples.

The samples tested during this experiment had previously been used for a milling wear test whilst still attached to their WC-Co substrates. An example of the damage to one of the PCD discs from this test is visible in fig. 5.2, however the flat front of the disc, where erosion will occur, has not been affected. It is possible, although unlikely, that high temperatures during the milling test have affected the microstructure, which will be investigated on analysis of the results. These damaged areas, and the chamfer around the edge of the discs will be protected by the edge protector discussed in Section 3.3 during erosion, and so will not be exposed to further damage.

Due to the expectation that the samples would have very similar and low erosion rates, the samples were eroded concurrently, such that the first increment was performed on all of the samples before any were subjected to a second interval. The order of erosion was randomised for each increment. Each sample was subjected to 9 x 1 kg increments, and the

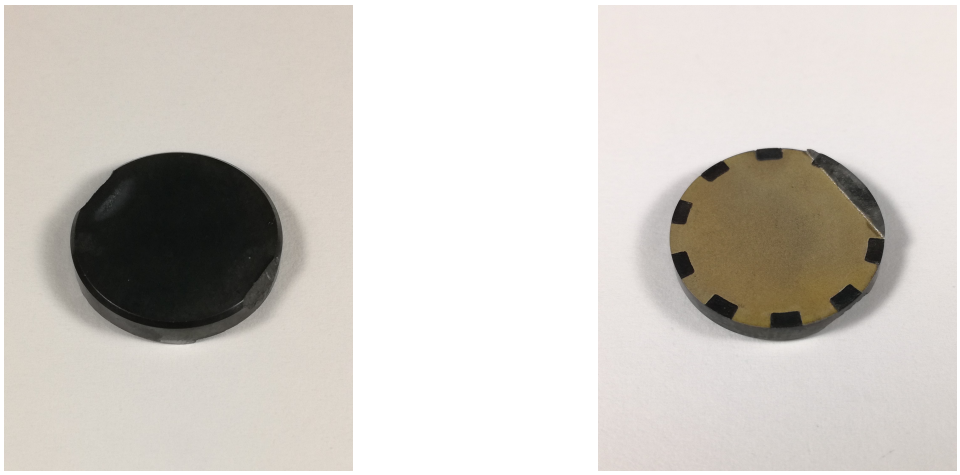

(a) (b)

Fig. 5.2 Images of a typical sample. The left image, (a), of the front PCD face shows that the locations of the wear scars are away from the erosion area in the centre. The image of the underside, (b), reveals information about the bonding pattern used to sinter the PCD layer to the WC-Co layer. The raised area (or lip) in the top right is a consequence of the manufacture process, formed when removing the PCD table from the compact by EDM, and does not interfere with the erosion process.

first increment of erosion was discounted to ensure erosion was measured only in the steady state regime.

5.2.3 Results and Discussion

The results of the erosion test showing the cumulative mass lost for each of the targets are presented in fig. 5.3. In summing over the 8 steady state erosion increments, the erosion process has successfully been able to distinguish between the sintering conditions.

The sample sintered at a nominal 5.5 GPa and 1400 °C suffered extensive damage on the very first erosion increment, to the extent that no further erosion was performed (fig. 5.4). The damage pattern on the surface showed a pair of cracks surrounding the erosion spot, and a symmetrical pattern of damage within the spot. The high erosion susceptibility appears to be due to the sintering process being incomplete. The symmetry of the erosion scar matches that of the undulating PCD/WC-Co interface and areas further from the WC-Co substrate have been preferentially eroded, suggesting that there has been a lack of cobalt flow during

the press run, causing a lack of carbon mobility and an incorrectly formed microstructure. As both of the two other samples sintered at the same pressure but at higher and lower temperatures did not demonstrate any similar susceptibility to erosion, it is likely that in this particular case an error was made during the manufacture process and the issue is not the result of the specific set of conditions sintered under, and so can be disregarded as an anomaly. It is notable that the damage due to the previous wear test has not affected the shape of the erosion pit, which was consistent with the rest of the samples.

For all of the other samples, SPE has proceeded as expected and has recorded different wear rates. Across all of the samples, the erosion rate is seen to decrease with time due to the widening of the barrel during a large quantity of erosion. To enable a fair comparison between samples, the total mass lost during steady state erosion is used to quantify the wear rate. Separating the sintering variables, fig. 5.5 shows that higher sintering pressures yield lower erosion rates. Higher pressures require more expensive manufacturing apparatus to produce, and so in any individual application there will be a trade-off between improved wear resistance and the cost of manufacture. From fig. 5.6, it was found that (over the range studied) sintering at a lower temperature produced more erosion resistant PCD. Although the sample size is small and limited repeats have been performed, both trends are consistent amongst all of the samples, and the temperature relationship holds at both 5.5 GPa and at 6.8 GPa.

It is notable that both increasing the pressure and decreasing the temperature moves further into the diamond stable region and away from the graphite region on the carbon phase diagram (fig. 2.4). Although diamond is the energetically preferred state at all of the sintering conditions studied here, the extent to which sp^2 bonding is prevalent within the samples is unknown. A high temperature should be preferred kinetically due to increased diffusion and is required to melt the cobalt catalyst to provide carbon mobility. It is also known that cubic diamond growth is preferred at lower temperatures whereas octahedral growth is preferred

nearer to the Berman-Simon line [134], which may affect the way in which PCD is sintered. The sintering conditions are also known to alter the residual stresses present [43] which may affect the wear rate. However, removing the majority of the WC-Co substrate from behind the PCD layer is thought to significantly reduce the sizes of any residual stresses present.

When compared with the data of Zhang *et al* [64], who found that wear resistance improved as temperature increased up to 1450 °C, before reducing at higher temperatures, here it was found that over the range 1350 °C to 1450 °C increasing the temperature decreased wear resistance. Due to the unknowns present, especially the distance between any thermocouple that measures sintering temperature and the PCD in the press, it is difficult to directly compare the two sets of data.

The average erosion rate for the multimodal sample was a factor of 1.5 higher than that of a monomodal G12 sample which was eroded concurrently as a reference. The lower cobalt content in these samples would decrease its ability to prevent cracks propagating, and, in accordance with the proposed mass loss mechanism in the previous chapter, increase the average length a crack would propagate before terminating in a cobalt pool.

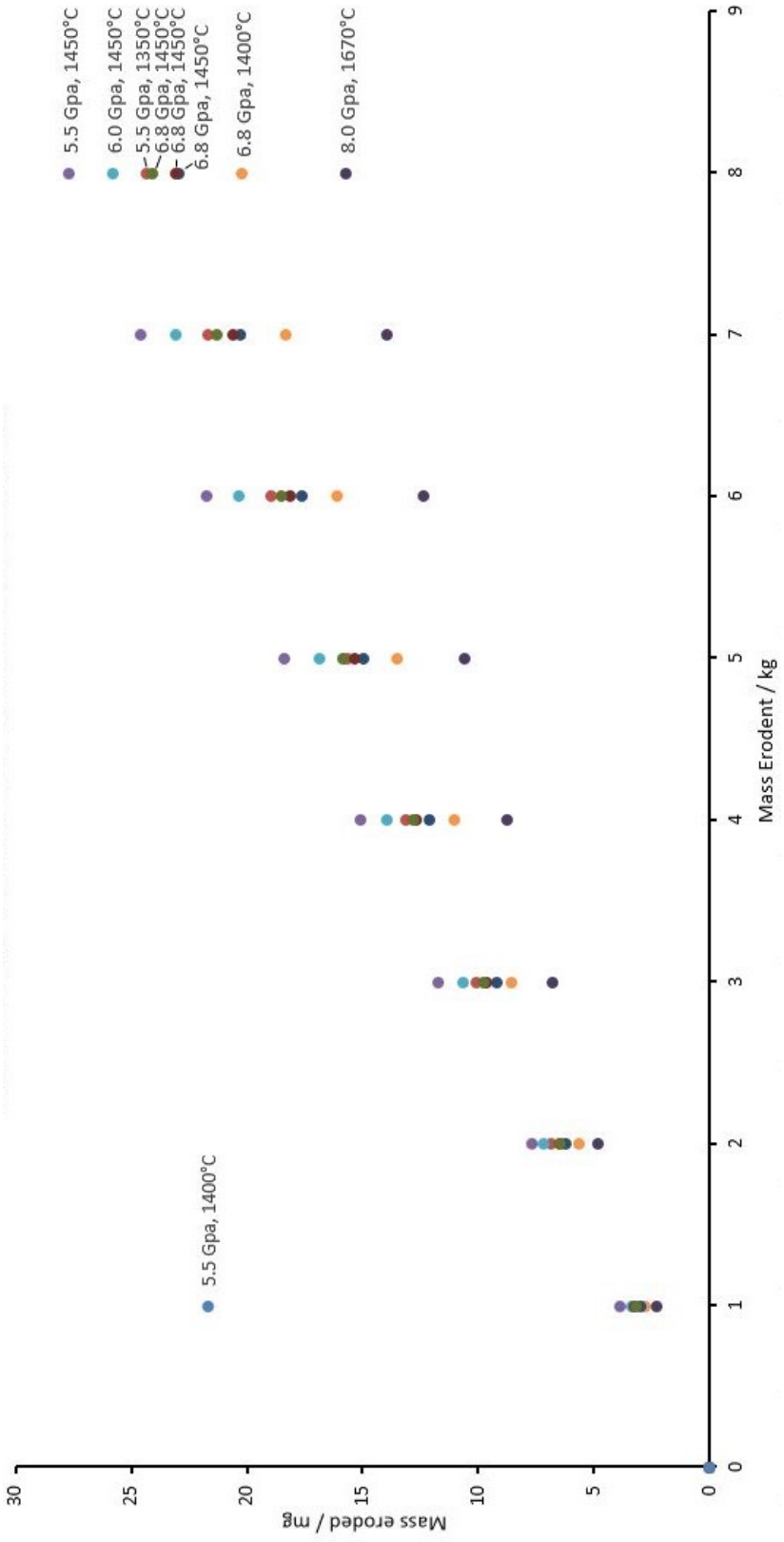

Fig. 5.3 Erosion of multimodal PCD discs with largest grain size of 22 µm, shown only for 'steady state' conditions, after 1 kg of erodent had previously impacted on the sample, except for the sample sintered at 5.5 GPa and 1400 °C for which only one increment was performed.

Fig. 5.4 The sample sintered at 5.5 GPa and a nominal 1450 °C after a single increment of erosion. A large mass loss was removed during the previous abrasive wear test, and erosion has formed cracks in the surface and eroded in a pattern. The 10-fold rotational symmetry of the erosion scar matches that of the PCD/WC-Co interface.

5.2.4 Summary and Conclusions

SPE has successfully been used to measure the differences in wear rate of PCD discs which were sintered under a range of conditions. A single increment could not distinguish the wear rates, but when the small differences in mass loss over 8 increments were summed together, trends could be identified. Erosion has clearly shown that samples sintered at higher pressures and at lower temperatures, both of which push further into the diamond-stable region in the carbon phase diagram, are more erosion resistant. The multimodal grain size distribution did not improve erosion resistance which is thought to be due to the reduced quantity of cobalt which can act to toughen the microstructure.

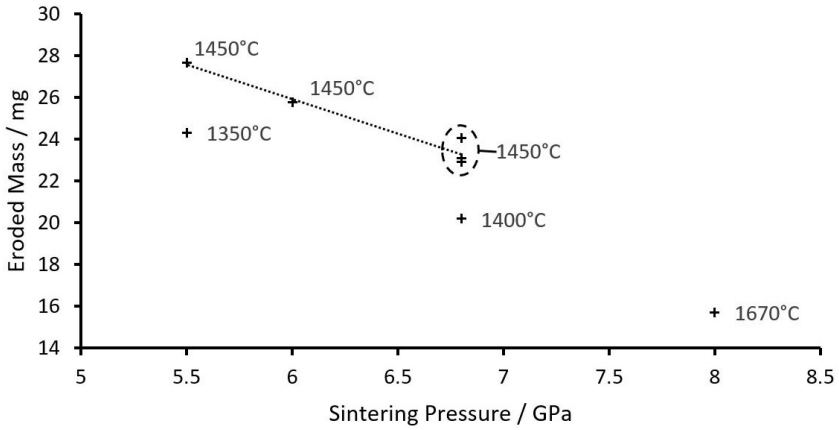

Fig. 5.5 The relationship between the mass eroded over 8 increments and the pressure that each PCD sample was sintered at, with the temperatures sintered at labelled next to each point. A line of constant temperature has been added to show the trend of lower erosion rate at higher sintering pressures.

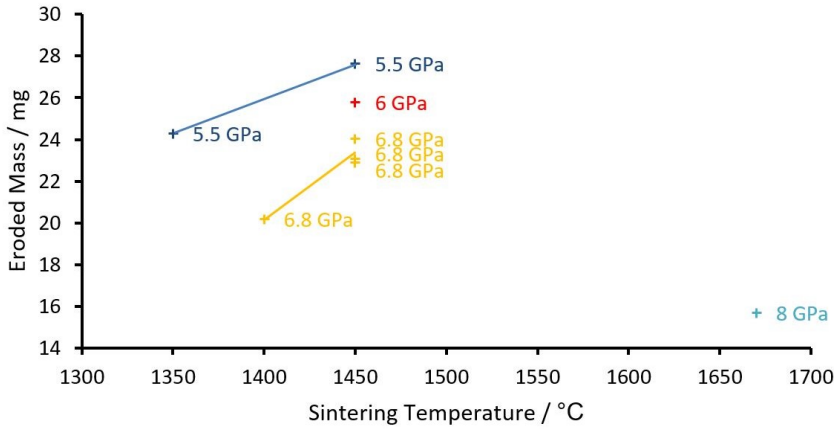

Fig. 5.6 The relationship between total mass eroded and the temperature that each sample was sintered at. Lines of constant pressure are drawn on to show the trend of a lower erosion rate for those samples sintered at lower temperatures.

5.3 The Effect of a Heat Treatment on Erosion

5.3.1 Introduction

Observing how the erosion process and rate varies after a post-manufacture heat treatment could give some insight into how the microstructural changes due to thermal history affect

wear behaviour. PDCs can become hot during drilling, and also can be subjected to intense heat whilst being brazed onto tool holders, which can have downstream effects on wear.

Here, heat treatments were performed in a Carbolite vacuum tube furnace in a vacuum of better than 6×10^{-3} mbar. The heat treatment temperature was measured by a thermocouple located within the work tube, in close proximity (< 5 mm) to the samples.

5.3.2 The Effect of 700 °C for 1 Hour

Two of each of the G30, G12 & G2 discs, one PCD and one RBPCD, were subjected to the vacuum heat treatment at 700 °C for one hour. Fig. 5.7 shows the temperature vs time profile including the warming and cooling phases.

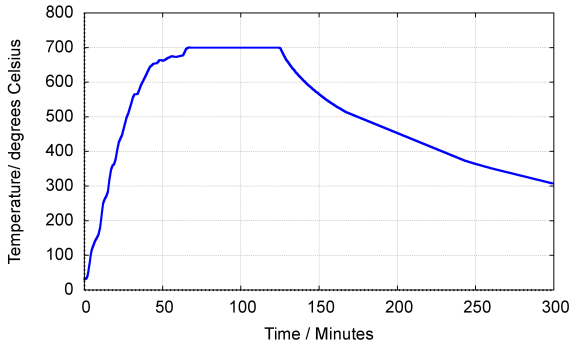

Fig. 5.7 Thermocouple response during 700 °C heat treatment of all six PCD samples, one of each grade G30, G12 & G2 and their RBPCD counterparts.

These PCD discs and a set of untreated discs were eroded concurrently, such that each sample was subjected to the first increment before any were eroded for their second increment. The steady state erosion rates are compared in fig. 5.8. The response of the un-treated samples is as expected and as previously discussed (Chapter 4, Section 4.5). The erosion rate decreases with grain size, but increases on reduction of the binder phase. After the heat treatment, the erosion rate of the G30 and G12 PCD grades undergoes a slight increase, while it decreases for the G2 grade.

There are a number of factors that may influence the structure of PCD as the temperature is increased, including surface oxidation, internal graphitization, and internal cracking caused

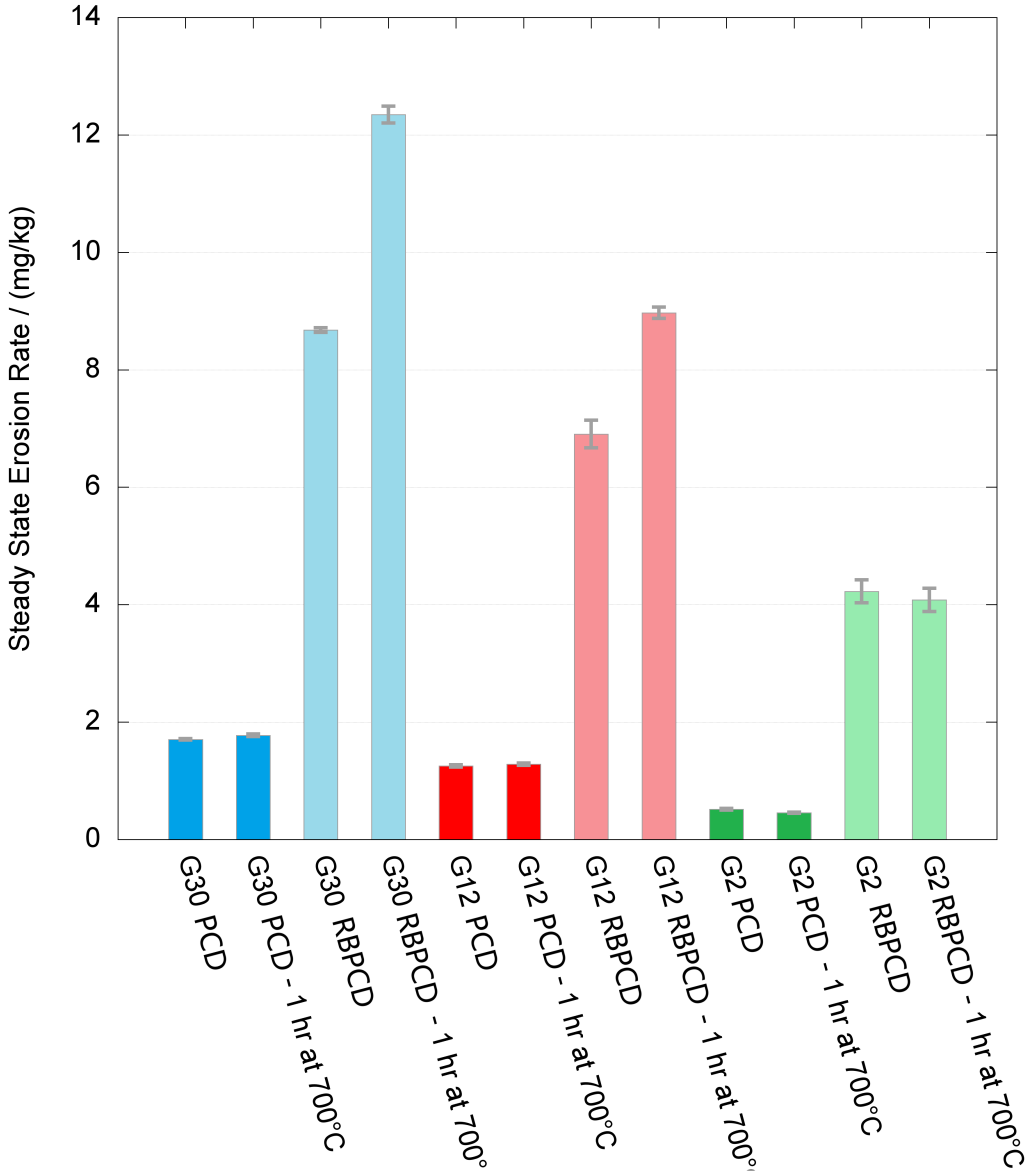

Fig. 5.8 Measured erosion rates for heat treated PCD discs. One disc was used to obtain each point, and the error is given by the variance in erosion rate for each kilogram increment. Rates were measured over 7 increments for PCD and 4 for RBPCD samples, after an initial increment to counter any differences in surface preparation between samples.

by the differential thermal expansion coefficients of diamond and cobalt. All of these factors would be expected to reduce the structural integrity of PCD and increase the wear rate. In the G30 and G12 grades, the wear rate has increased as expected, however in the G2, where the surface area between cobalt and diamond is the greatest, the erosion rate has remained the same to within error. The reasons for this behaviour could be anomalous, only one disc of each was chosen and it is known that sintering conditions can affect wear rate, or due to another factor, such as the heat treatment allowing any residual stresses within the disc to relax.

The RBPCD grades follow a similar pattern, however the change in erosion rate for the coarser grades is much more pronounced. The larger increase is due to the oxygen in air, present in the capillaries between the diamond grains left behind by the binder reduction process. A weak vacuum over a short timescale (1 hour) will not extract all of the air, and hence oxygen, from the centre of the RBPCD discs. The oxygen can help catalyse the degradation of PCD and as it is present well within the bulk of a RBPCD sample, will damage the microstructure throughout the material.

5.3.3 The Effect of Time and Temperature

Both temperature and time at that temperature can be varied during a heat treatment, and both are relevant to determining the tool life of PCD in application. Here, a number of G30 PCD discs were held at a temperature in vacuum for either 1 hour or 6 hours as shown in fig. 5.9. The limitation on the number of discs that can be compared in any one test is the number that can be eroded concurrently, as the erosion barrel will widen during the experiment due to the highly abrasive conditions and reduce the erosion rate or fracture and prevent further erosion.

The disc that was subjected to 850 °C for 1 h developed a crack along its centre, shown in fig. 5.10. Due to the crack, and the expected preferential erosion at exposed edges, this disc was not eroded. It can be assumed that the erosion rate would have been anomalously

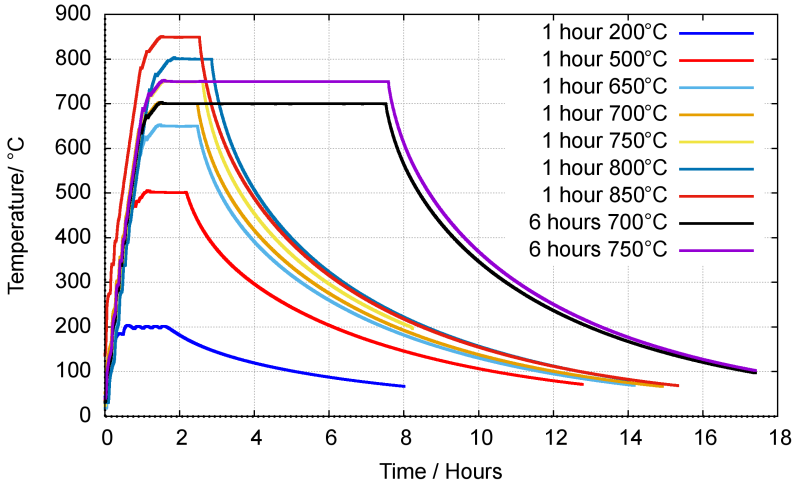

Fig. 5.9 Heat Treatments applied under a vacuum of better than 6×10^{-3} mbar. The temperature was measured by a thermocouple placed inside the vacuum tube in close proximity to the PCD disc.

high and it is likely that the disc would have fractured across its diameter during the first increment.

Fig. 5.10 A G30 PCD disc after a 1 h heat treatment at 850 °C, showing a crack running through the centre of the disc which excluded it from further experiments.

The erosion rates for the rest of the discs, as well as two untreated control samples are presented in fig. 5.11. There is some variance in the erosion rate between the two untreated discs. The error bars in fig. 5.11 show the error in the erosion rate as measured, however, other factors, such as where the PCD compact was placed within the press and so what

temperature and pressure it reached during the sintering, can alter a disc's wear properties which must be accounted for when analysing the results.

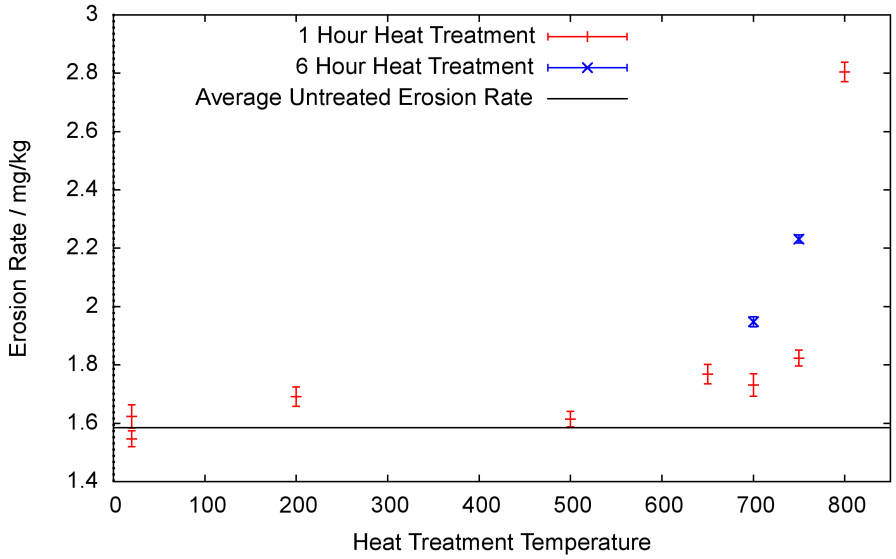

Fig. 5.11 Measured erosion rates for heat treated G30 PCD discs. Rates were measured over 7 increments and the error is given by comparing the erosion rates for each 1 kg increment.

As the heat treatment temperature increases to 500 °C, the erosion rate does not increase significantly above the measured rate at ambient temperature. At thermal treatments of 650 °C to 750 °C, the erosion rate is appreciably higher than that measured at ambient temperature, however the increase is small (10%).

The erosion rate after one hour at 700 °C is consistent with that recorded in the previous test (fig. 5.8) for a G30 PCD, being 10% higher. However, six hours at 700 °C has further damaged the PCD, and increased the wear rate by 25% compared to the untreated discs. The trend for the two discs treated at 750 °C is the same. From these results we can determine that the thermal damage is time-dependent, and so it is thought that time-dependent chemical changes are responsible for the damaged microstructure. Cobalt catalysed graphitization and breakdown of the sp^3 carbon structure, whether nucleating microfractures or increasing expansive stresses in the PCD, is thought to be causing the increased erosion rate with temperature. The degradation of PCD with temperature is consistent with that observed by

Petrovic *et al* [72], however the damage has been more pronounced and been measured with smaller errors in the erosion wear test than the fracture tests used by Petrovic.

5.3.4 The Effect of Atmosphere During Heat Treatments

To test the effect of atmosphere during a heat treatment on the mechanical properties of PCD, a single disc of G30 PCD was heated in a furnace in air, and its erosion rate was compared to that of a disc heated in a vacuum tube furnace at a pressure lower than 6×10^{-3} mbar. The heat treatments followed similar temperature/time profiles (fig. 5.12).

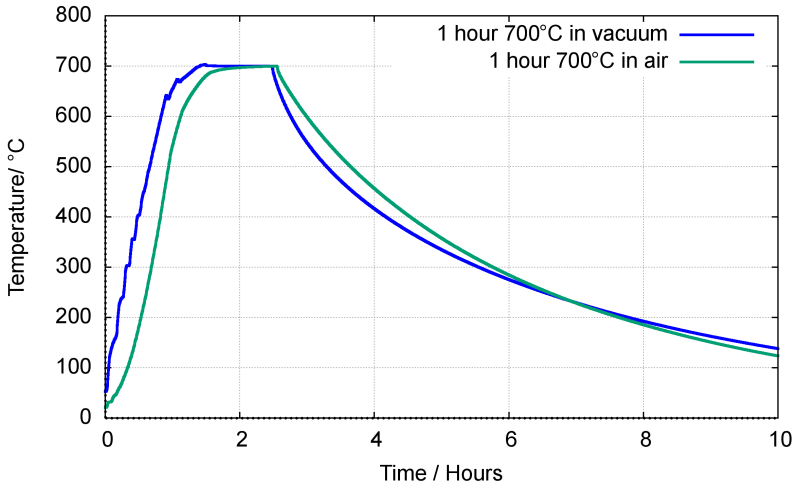

Fig. 5.12 Heat treatments applied to two discs at 700 °C. Both samples spent close to 1 hour at temperature but were subjected to different atmospheres.

The discs were eroded together, as part of the experiment in Section 5.3.3, and the erosion profiles are shown in figs. 5.13 & 5.14. Initially, the disc heated in air has a very fast erosion rate. The presence of oxygen during heating has greatly weakened the material in the volume nearest the surface. As the erosion progresses however, the erosion rate of the disc treated in air reduces, and tends towards that of the vacuum treated disc. This response can be understood because, as the damaged material is removed by erosion, erodent begins to impact on the undamaged material beneath.

By extrapolating the gradients of the erosion profiles in fig. 5.13 (or integrating under fig. 5.14), the mass of damaged material can be calculated and was found to be 19 mg. Knowing the area of erosion (7.5 mm diameter circle), the depth of the damaged material can be estimated to be 126 µm. The value is an upper bound of the damage depth, as it is possible that the cleaning and washing procedures during the weighing process will remove material damaged due to the heat treatment in air from locations other than the central erosion spot. The value is significantly larger than one grain size (30 µm), indicating that during the hour's heat treatment oxygen has diffused into the surface and caused subsurface damage, or that cracks formed due to surface oxidation can propagate many grains deep into the material.

5.3.5 Summary and Conclusions

The erosion process has been used to compare the thermal damage induced by heat treatments. A 1 hour, 700 °C heat treatment under a moderate vacuum has had only a small effect on the erosion rate of PCDs (10% increase for G30 and G12, 5% decrease for G2). However, the erosion rate of RBPCD samples for the G30 and G12 grades increased significantly (40%). For the RBPCD G2 grade, the erosion rate showed no change larger than its error. These changes correlate with the expected difference in mass removal mechanism between the finer G2 and coarser G12 and G30 grades.

A treatment of 500 °C for 1 hour did not affect the erosion rate. Heating in air, as opposed to a mild vacuum, caused an initially very high erosion rate due to surface damage processes, which then tended towards the bulk value as erosion progressed.

More harsh heat treatments above 700 °C, in both time and temperature, were shown to decrease wear resistance. The limitation of this section is the use of single samples for each data point. As there is some variance in the erosion rate of the untreated samples, caution must be exercised when drawing conclusions relating to a single data point. However, the overall trend for decreased wear resistance at temperature and with longer time periods is clear.

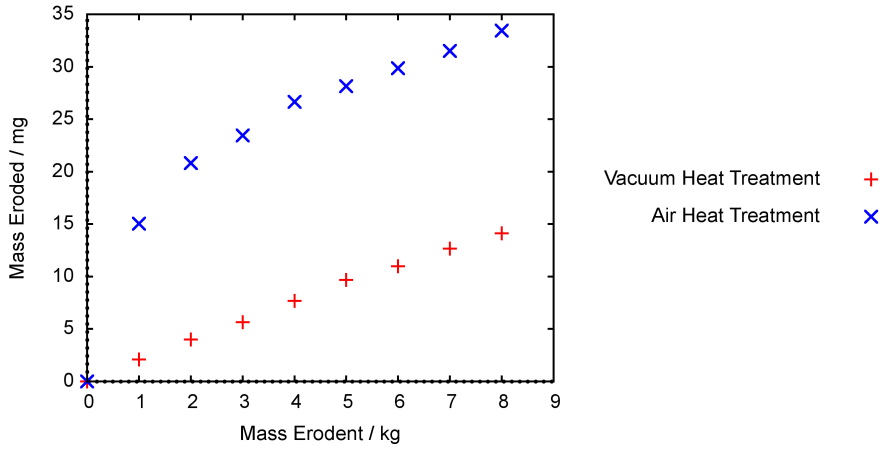

Fig. 5.13 Erosion profile of two G30 PCD discs with a 1 hour 700 °C heat treatment under air and vacuum conditions.

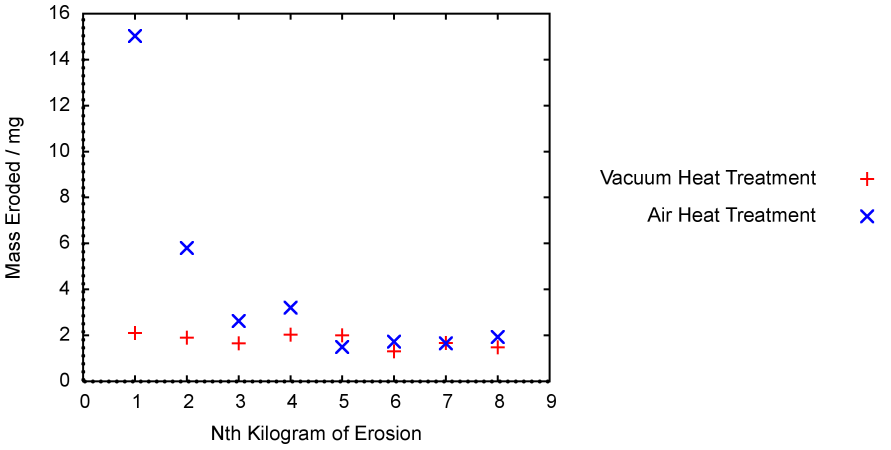

Fig. 5.14 Mass eroded per kilogram of erodent between G30 PCD discs with a 1 hour 700 °C heat treatment under air and vacuum conditions. Each point is the gradient of fig. 5.13 for each erosion increment.

Chapter 6

Solid Particle Erosion at Elevated Temperatures

6.1 Introduction

Previously, the response of PCD to erosion under a range of conditions has been investigated at room temperature. However, during drilling applications, frictional heating will warm the wear surface to significantly higher temperatures than the surroundings. Wear rates of PCD are known to increase at the high temperatures experienced during drilling (Section 2.3.2) and temperatures of up to 500 °C have been measured in the bulk, with even higher temperatures expected at the cutting face [71]. Understanding thermal degradation and the temperatures at which it occurs in detail is important to the design of drilling systems which use PCD tools. In addition, the presence of cobalt is known to participate in the thermal degradation processes, and so the extent to which thermal degradation is reduced on reduction of the binder phase is of importance and will be measured.

To simulate the conditions that PCD is subjected to whilst in application, a combination of thermal and mechanical wear must ideally be simultaneously administered. In this chapter,

high temperature SPE is discussed and its applicability to PCD is reviewed. A new set of apparatus has been developed specifically for high temperature SPE of PCD.

6.2 Previous High Temperature SPE Research

An understanding of how erosion changes with temperature is important to any component that may be subjected to an erosive environment at temperatures above ambient. An example of an application for high temperature SPE testing is for the leading edges of turbine blades in power plants. Higher turbine temperatures result in higher efficiencies, but particulates are introduced into steam turbines during heating cycles and can damage the fast moving alloy blades by erosion, accelerated by corrosion processes at high temperatures [135]. A further example is the erosion caused to turbine blades in the hot regions of jet engines by ash particulates emitted by volcanic eruptions [80].

The concept of performing erosion at elevated temperatures is not new. Interest in the erosion-corrosion of stainless steels developed in the 1980s [136, 137]. High temperature erosion experiments by Levy *et al* [138] in 1986 measured erosion rate of stainless steel at temperatures up to 900 °C and at moderate velocities of up to $30\,\mathrm{m\,s^{-1}}$ by pre-heating the airflow which carries the erodent. The erosion rate was found to be temperature-dependent, with all of the steels recording constant or decreasing erosion rates as the temperature increased, until chemical corrosion-erosion processes rapidly increased the erosion rate above 400 °C.

Research in the 1990s focused on the high temperature erosion of ceramic coatings. For example, experiments by Colclough & Yeomans [139] in 1997, where SiC and SiC-Titanium diboride were eroded with SiC at temperatures up to 1000 °C at $70\,\mathrm{m\,s^{-1}}$. On investigation of the eroded region, surface oxidation at high temperatures was identified as the mechanism by which the erosion rate increased with temperature. Ham *et al* [140] performed further research on biphasal ceramics at temperatures up to 726 °C, with a specific focus on how

the residual stresses due to the mismatch of thermal expansion coefficients may affect the erosion rate on heating.

Alman *et al* [141] measured the high temperature erosion rate of iron-aluminide cermets, however they did not heat the airstream but only the target chamber. As the cool airflow passes over the sample, large temperature gradients are established, and so the temperature of the eroded surface becomes difficult to measure accurately. The authors used very pure 99.999% N_2 gas to drive the erodent at velocities up to $40\,\mathrm{m\,s^{-1}}$ which was used to decouple the erosion rate from the chemical changes caused by the oxygen present in ambient atmospheres.

More recent research by Wang *et al* [142] in 2012 found that in alumina ceramics, the behaviour of erosion rate with angle became more ductile-like at temperatures over 1000 °C and even more so at up to 1400 °C, although SEM analysis of the surfaces was not able to confirm that the mass loss mechanisms were similar to those typical of brittle materials. Li *et al* [143] eroded SiC-Si_3N_4 composites and found that plastic fracture mechanisms were present during erosion at temperatures up to 1400 °C.

High temperature SPE has been performed to a limited extent on a variety of materials with a range of potential applications. Evidence for previous research in which PCD is eroded at high temperatures has not been found.

6.3 Approaches to High Temperature SPE

Two different experimental approaches to high temperature erosion are shown in fig. 6.1. Yang *et al* [144] have heated the substrate but allowed cool air to blow across it, while Wang *et al* [145] contain the sample within a sealed region, which will prevent airflow from mixing down a long thin nozzle, 20 mm in diameter. Both approaches were used to erode hard ceramic coatings at up to 1400 °C, however the approach by Wang *et al* will be able to measure the temperature of the eroded surface more accurately due to the lower thermal gradients caused by the reduced airflow across the sample.

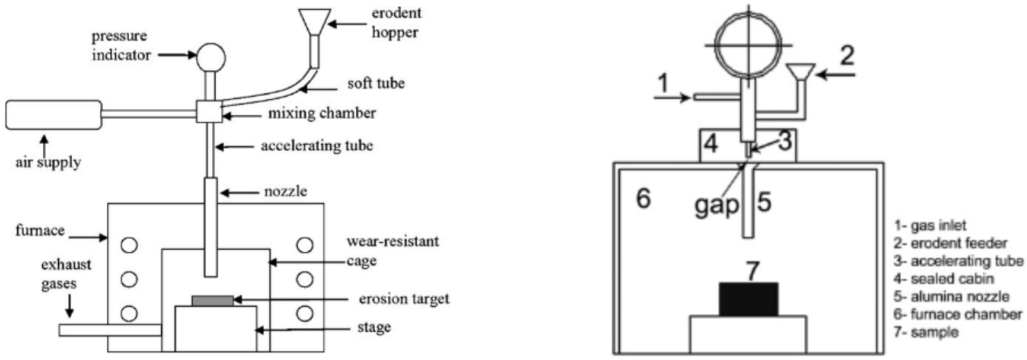

(a) Yang's approach [144]. (b) Wang's approach [145].

Fig. 6.1 Two different schematics showing how high temperature erosion has been performed. Both authors claim to be able to perform erosion at temperatures up to 1400 °C.

A third approach to high temperature erosion, recently employed by Fry *et al* [80] and similar to that used by Levy [138] is to heat both the gas that carries the erodent and the target or an oven surrounding the target. The major advantage of this method is the vastly reduced error in the erosion temperature, however disadvantages include the amount of power required to heat a large quantity of fast-flowing air (of order 20 kW) and the need to remove or vent this heat on extraction. The extent to which oxidation or softening of the erodent is changed with temperature is often unquantified, which becomes a serious problem when comparing high temperature erosion data. The erodent can be introduced either before or after the air is heated, and the length of time that the erodent spends in the hot environment can alter its properties and subsequently the erosion rate.

Swaminathan *et al* [135] performed a survey of known high temperature erosion research facilities in 2013 and found five laboratories with the capability, including commercially available equipment from DUCOM India. In order to develop a standard for high temperature SPE, all of the facilities were asked to perform erosion on type 410 steel at room temperature and at 600 °C and report on their results. A 50 µm alumina erodent was chosen to impact at 200 $\mathrm{m\,s^{-1}}$ with a total of 100 g in five 20 g increments being used. A very high variance in erosion rate was found, with a factor of 1.8 between the lowest and the highest, despite all of the sets of apparatus using the same erodent and nominally the same conditions. The authors

attribute the discrepancy, at least in part, to the use of different velocity calibration methods where both the rotating disc method (a description of which is given by Ruff & Ives [146]) and particle image velocimetry were employed.

The comparative study of high temperature SPE facilities lead to the initiation of the ASTM Standard G211-014 test [147] which used the same conditions as in Swaminathan's study. In a similar manner to the standard for room temperature erosion (G76), this ASTM standard is not appropriate for high temperature erosion of PCD. It requires an alumina erodent, which is known to produce prohibitively low erosion rates in PCD, and the mandated erodent feed rate is also low at $2\,\mathrm{g\,min^{-1}}$. In order to produce 1 µg of mass loss in PCD, even with a SiC erodent, 8 h of exposure time would be required, which is deemed unpractical. Further, although the nozzle size proposed in the standard test is 1.5 mm to 3 mm, the test requires an erosion spot diameter of 14 mm, which is likely to cause damage to the edges of the 16 mm diameter PCD samples.

High temperature SPE of PCD is expected to be challenging due to PCD's very low erosion rate.

6.4 Use of National Physical Laboratory High Temperature Erosion Facility

6.4.1 Introduction

A set of apparatus for performing high temperature solid particle erosion has been developed by the UK's National Physical Laboratory (NPL) [80, 148]. The original purpose of the apparatus was to determine the consequences of volcanic ash impacts on high velocity turbine blades in jet engines, as a response to a volcanic eruption which part-closed European airspace in 2010 and caused widespread disruption [79]. The apparatus is capable of eroding targets with 100 µm to 125 µm sized alumina erodent at velocities of up to $300\,\mathrm{m\,s^{-1}}$ and

at temperatures of up to 900 °C, and has previously been used to erode aluminium and nickel-based superalloys. Here, the apparatus was used to erode G12 PCD.

6.4.2 Apparatus and Calibration

A schematic of the NPL high temperature erosion apparatus is shown in fig. 6.2. Both the inflowing air and the region surrounding the sample are heated, while the erodent is introduced after the airflow has been heated. The velocity was calibrated at room temperature using the standard spinning discs method, a summary of which is given by Hutchings [149]. The minimum erodent velocity was measured at $114\,\mathrm{m\,s^{-1}}$, the mean was $289\,\mathrm{m\,s^{-1}}$, and the maximum was $544\,\mathrm{m\,s^{-1}}$.

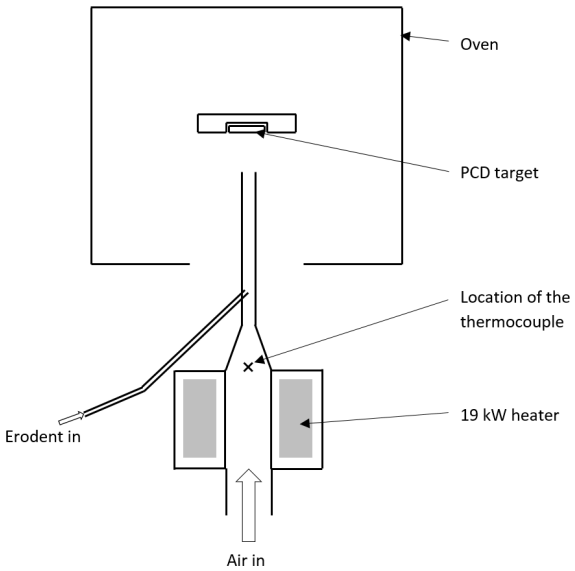

Fig. 6.2 A schematic showing the NPL apparatus and the location of the temperature thermocouple in the air stream immediately after the heater.

The standoff distance between the barrel and the sample at room temperature was 22 mm and the diameter of the barrel was 5 mm. As the barrel heats up, it will expand lengthwise to shorten the standoff distance however this is not expected to be a significant factor affecting the erosion rate [150].

6.4.3 Results

Five discs, all G12 grade, were eroded in 1 kg increments at different temperatures but only experienced either one or two increments due to time constraints. The results are presented in fig. 6.3 and show that the erosion rate decreases with temperature before increasing at much higher temperatures, although high errors are recorded due to the low erosion rates.

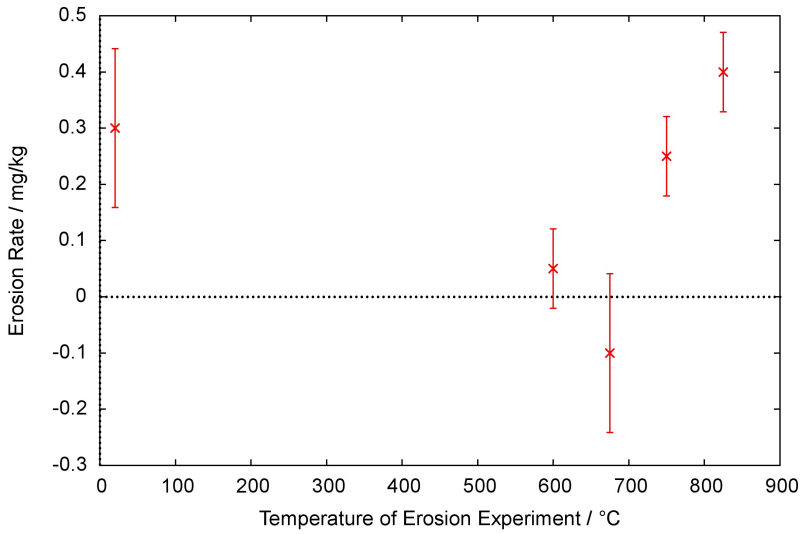

Fig. 6.3 The results of SPE of PCD using the NPL high temperature apparatus. Limited data was obtained due to the unsuitability of the apparatus with two samples only receiving one erosion increment and the three with smaller errors receiving two increments.

Fig. 6.4 shows the sample that was eroded at 675 °C. The negative erosion rate for this sample was caused by alumina embedding onto the surface and not being removed during the ultrasonic bath. The shape of the deposits is in streaks located outside the erosion spot, which implies that the erodent has passed across the surface here at a shallow angle.

The three temperatures for which a second interval was performed (600 °C, 750 °C and 825 °C) can be compared with more confidence however the total mass eroded is still small, so the initial cobalt removal and the state of the surface prior to erosion will dominate the response. There is some evidence for a decreased erosion rate with increasing temperature,

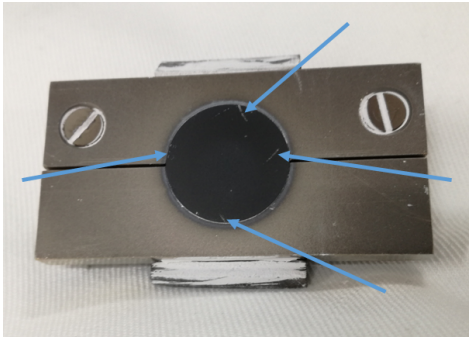

Fig. 6.4 G12 PCD eroded at 675 °C using the NPL high temperature erosion apparatus. The blue arrows point towards Al_2O_3 deposits embedded into the surface.

followed by an increase at higher temperatures (800 °C). The mechanical properties of PCD are expected to break down at 800 °C and above and so it is surprising that the wear rate of PCD should remain moderate at such a high temperature. It is thought that either the wear caused by the impinging alumina is so minimal that long-term erosion rates are not being measured, or that the temperature at the eroded surface is not as high as the nominal 800 °C measured in the air heater.

6.4.4 Summary

The NPL high temperature erosion apparatus was designed for use on less erosion resistant materials than PCD and so it was not possible to erode PCD beyond the initial surface layer. As such, alternative methods for high temperature erosion of PCD must be explored.

6.5 Apparatus Development

The aim of this section is to design a set of apparatus that is able to erode PCD with SiC at temperatures up to 700 °C. Due to the highly abrasive environment that will be required, any materials or heating elements that are used must be erosion resistant and capable of functioning at the desired temperatures. Any parts that are likely to be eroded must be both durable and replaceable.

In order to erode materials at high temperatures, heat must be supplied to either the target, the airflow, or both. If only the target is heated, the cooler airflow will reduce the surface temperature of the sample below that of the sample holder, introducing large thermal gradients and resulting in high uncertainties in the surface temperature. If the airflow is to be heated, high powered heaters are required, with the NPL apparatus utilising a 19 kW heater, for example. The low erosion rate of PCD will lead to long erosion times, and so if the airstream was heated, a significant quantity of thermal energy would be produced which would then need to be absorbed or vented in a safe manner.

A method for performing high temperature SPE without the requirement for a very large energy input is to separate the erodent particles from the airflow, in a similar manner to Wang *et al* [145]. By placing the target and the heating apparatus within a sealed box with a single small opening in front of the barrel, the back pressure built up in the box will limit air mixing and thus cooling of the target. If the stand-off distance between the barrel and the opening of the sealed box is short, the erodent will not have time to be diverted by the airflow and will continue on straight through the stagnant air towards the target. The set of apparatus of which a schematic is shown in fig. 6.5, was designed and built for use in this project on PCD. It was found during testing that there was still some air mixing between the inside and the outside of the sealed box, so a secondary heater, labelled in fig. 6.5, was installed around the opening in order to pre-heat the mixing air. The highest temperature that the apparatus was operated at was 600 °C, although up to 700 °C was possible within the design limits. The maximum power delivered to the sample heater during operation at 600 °C was 350 W and the maximum at the opening was 115 W, which is over an order of magnitude smaller than would be required to heat the airflow.

Images of the high temperature erosion apparatus showing how the sample was held in the heated sample holder and how the box was formed and sealed around it are displayed in fig. 6.6. During operation, a 4 mm diameter barrel was used and the opening to the sealed

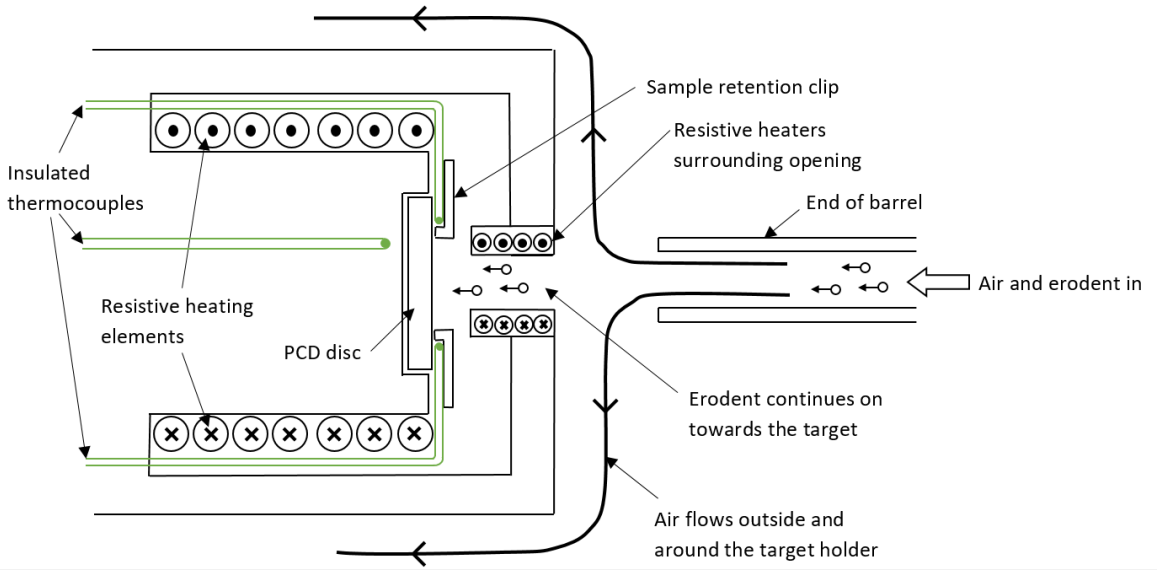

Fig. 6.5 A schematic, not to scale, of the high temperature erosion apparatus showing the erodent and air mixture exiting the barrel, but back pressure from a sealed box surrounding the sample prevents air mixing while the erodent is allowed to continue on towards the target. Both the sample holder and the small opening are surrounded by resistive heating elements to produce the required temperatures. The sample is surrounded by three thermocouples for accurate temperature measurement.

box was protected by a 4.2 mm diameter alumina bush which was replaced regularly when worn. The velocity of the erodent on exit of the barrel was $(83.2 \pm 6.4)\,\mathrm{m\,s^{-1}}$ throughout all of the erosion experiments, although it is expected that the erodent will slow down slightly during its motion through the stagnant air inside the box on approach to the target. The stand off distance between the end of the barrel and the opening was 8 mm.

The erodent was chosen to be the same as the majority of previous experiments, F36 mesh SiC. The maximum quantity of erodent that could be impacted in any one increment was limited at 500 g by the size of the container underneath the sealed box which collects the fractured erodent. During any one increment of erosion at high temperature, the sample is heated up with the air flowing but with no erodent present. After stabilising at the desired temperature for up to 2 min, it is eroded for 5 min before the heater power is turned off and the sample cools, whilst the air remains flowing. On return to ambient temperature, the

sample is then removed, washed in an ultrasonic water bath and weighed in the same manner as with the samples eroded at room temperature.

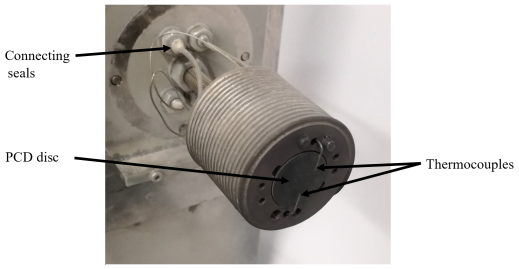

(a) A close up of the sample holder.

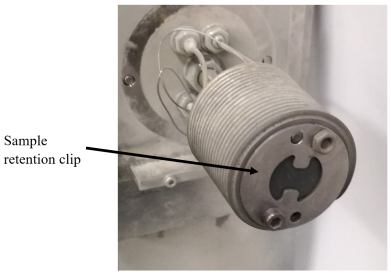

(b) The sample holder with retention clip in place.

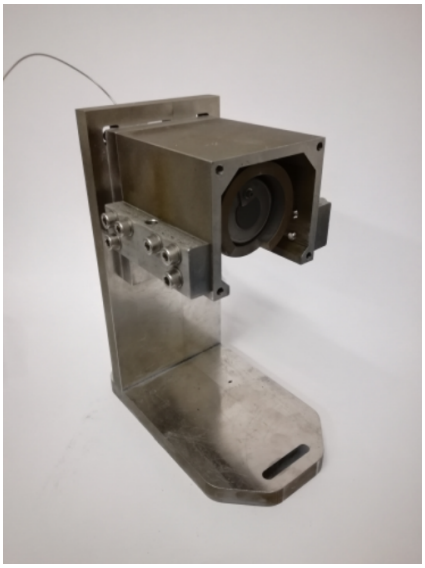

(c) An early version of the sample holder mounted within the box.

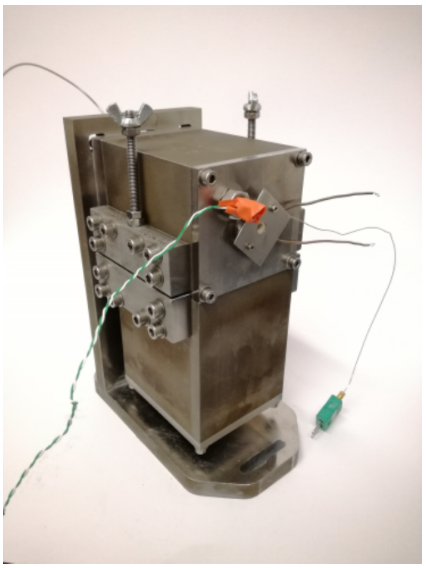

(d) The fully sealed box.

Fig. 6.6 Images of the high temperature SPE apparatus capable of eroding PCD at temperatures up to 600 °C by isolating the sample within a sealed box and separating the fast-moving erodent from the cooling airflow.

6.6 Calibration

Despite best efforts to reduce air mixing through the front opening of the airtight box, some flow is inevitable. Any cooler air passing over the surface of the PCD target will cause thermal gradients which will introduce a difference between the temperatures measured by the thermocouples located around the sample and the actual temperature at the erosion spot.

During erosion, the temperature at the front face cannot be measured directly. A thermocouple placed there would rapidly erode, and pyrometry is inhibited by the highly erosive environment which would damage either the pyrometer itself, or the end of any optical fibre that would link the measurement region to outside of the erosion chamber. Three thermocouples were located around the sample (fig. 6.5) as close as possible to the region which will be eroded, with a further thermocouple present within the heater surrounding the front opening. As such, calibration of the thermocouples to the temperature at the erosion spot is essential.

In order to calibrate the differences between these thermocouples, a test run was performed with the air flowing but without any erodent present, with a very small (0.5 mm diameter) thermocouple bonded onto the front face of a PCD disc with high temperature cement (Omegabond 600). For each front face temperature, the apparatus was allowed to equilibrate for 2 min and the temperature within the sample holder immediately behind the disc was measured. Five repeat calibration runs were performed giving the data shown in fig. 6.7.

During operation, the temperature of the sample holder was chosen to match the intended temperature of the front face, with the thermocouples clamped to the front face used as a further reference. The error in the temperature is obtained by taking the standard deviation in sample holder temperatures from the five calibration runs shown in fig. 6.7. For example, in order to obtain a front face temperature of 500 °C, the sample holder would be held at 630 °C and the random error in the temperature would be ± 9 °C. It is believed that, due to the high thermal conductivity of PCD, the majority of the thermal gradient occurs at the interface between the stainless steel sample holder and the PCD disc. The nearly 1 : 1 ratio between the temperature at the erosion spot and that measured by the thermocouples clamped to the front face of the PCD helps to support this.

When the calibration thermocouple is removed and the apparatus is operated with erodent at a flux rate of $100\,\mathrm{g\,min^{-1}}$, the action of the erodent entering the sealed box and impacting

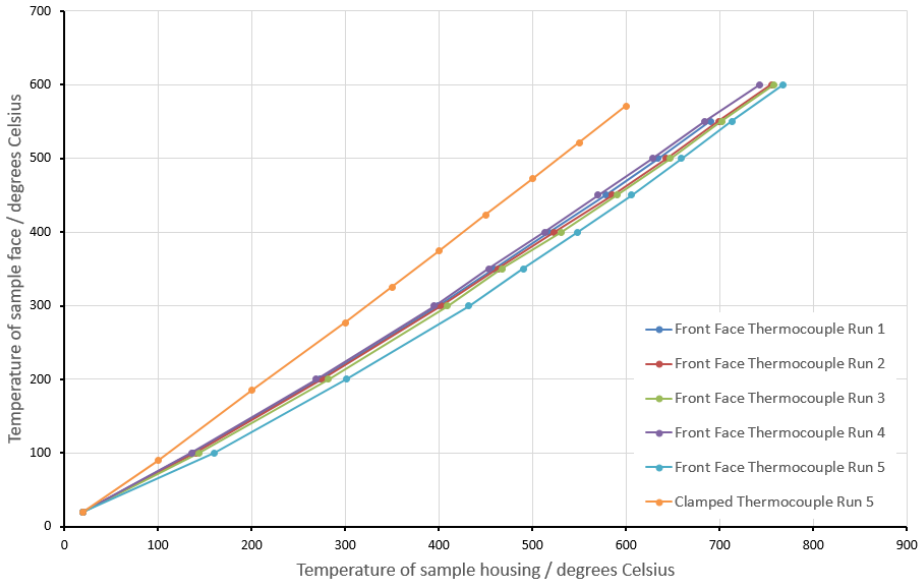

Fig. 6.7 A graph showing the relationship between the temperature at the front face of the PCD disc and that in the sample holder immediately behind it. A single set of data for the temperature of the thermocouple clamped to the front face of the PCD disc is also shown.

on the PCD disc has an effect on the temperature of the eroded surface. At ambient and low temperatures ($< 100\,^{\circ}$C), the temperature of the front face of the PCD disc, as measured by the thermocouples clamped to it, increases. A small proportion of the erodent's kinetic energy is transferred into thermal energy on impact. The extent of the temperature increase was typically less than 5 °C. At higher temperatures, the opposite effect was seen. The cold erodent would, during impact and whilst in the vicinity of the sample, be temporarily in thermal contact with the hot PCD. As such, heat would flow away from the surface and reduce its temperature by up to 20 °C at 500 °C. These temperature fluctuations must be considered when analysing any high temperature SPE data.

6.7 Heating of the SiC Erodent

The erodent spends only a very short period of time (of order 0.2 ms) within the high temperature region before impacting the PCD target. Due to this short timescale, it is not

thought that the erodent will be warmed up by the high temperatures present in the sealed box. Surface oxidation of SiC requires temperatures of over 1000 °C in order to be measurable on practical timescales [151], and so is not believed to be of importance during short-timescale erosion experiments at lower temperatures. The brittle-ductile transition temperature occurs at greater than 1600 °C [152] and so which will not be relevant to the experiments performed in this thesis.

6.8 Summary

High temperature SPE is an active area of research for gas turbine blades and their coatings. It has been performed on steels, nickel alloys and ceramic coatings but not previously on PCD. High temperatures can be achieved by heating either the substrate, the airflow, or both. There are various disadvantages to each heating style, and the stage at which the erodent is introduced to the airflow is a further factor which affects erosive behaviour.

The international standard for high temperature SPE is inappropriate for erosion of PCD due to PCD's very low erosion rate. A test using the apparatus present at the NPL, designed to erode softer materials, confirmed this.

A set of apparatus has been designed, constructed and tested which adapts the current Cavendish Laboratory erosion apparatus to facilitate erosion at temperatures up to more than 600 °C. Calibration was achieved by operating the erosion rig without erodent flowing, but with a very small thermocouple placed at the region which will be eroded.

Chapter 7

High Temperature Erosion of PCD

7.1 Introduction

Previously, an apparatus was developed which can perform high temperature SPE on PCD. In this chapter, the response of PCD to high temperature erosion is measured for the first time. A further test at room temperature on the samples which had previously been eroded at high temperatures is performed in order to help determine the method by which the erosion mechanism changes on heating.

7.2 High Temperature SPE of G30 PCD

Due to the deterioration of critical components such as the resistive heaters and their electrical connections by erosive processes, only a limited number of experiments were able to be performed and so specific tests were chosen carefully to maximise the information that each test would yield. The velocity of the erodent was kept low at $(83.2 \pm 6.4)\,\mathrm{m\,s^{-1}}$ in order to reduce airflow across the sample to limit the error in temperature, and so the erosion rates were also expected to be low. The PCD with the highest erosion rate was the G30 grade, and so G30 samples were used for the majority of high temperature SPE experiments in order to reduce the error in the measured erosion rates.

For the first test, two discs of G30 PCD were eroded initially at room temperature before subsequently being eroded at each higher temperatures. All of the increments performed at any one temperature were completed before the disc was then eroded at a higher temperature. The advantage of this approach is that the erosion rates at different temperatures can be directly compared for a single sample, without encountering the possibility that discs of nominally the same properties may have different erosion rates under the same conditions. The primary disadvantage is that at higher temperatures, any damage from previous increments performed at lower temperatures may be cumulative, and that the any variance of the erosion rate with depth (thought to be minimal from the erosion profile measured in fig. 4.4) could skew measurements.

Fig. 7.1 shows the erosion rate vs temperature for the two G30 discs, with a more detailed view of the data at lower erosion rates given in fig. 7.2. There is a small amount of scatter at room temperature followed by a clear decline in erosion rate as the temperature is initially increased, a result which is consistent over both samples and a large number of increments. At 200 °C, the erosion rate was half the value measured at room temperature, which was unexpected as no significant change in the physical properties of PCD are expected over this temperature range. Potential reasons for the improved erosion resistance include the softening of the cobalt binder, which could improve toughness, and changes in the residual stresses present at the surface. Although, the differential thermal expansion coefficients of diamond and cobalt are expected to increase the likelihood of crack propagation on heating which contradicts the result obtained here.

As the temperature is further increased, a corresponding increase in erosion rate at around 450 °C was measured which increases rapidly with temperature. Erosion was stopped after 550 °C and 500 °C for each sample respectively as with the high erosion rates at these temperatures the sample could fracture and cause subsequent damage to the apparatus. The increased rate of material removal occurs at temperatures well below those expected for

internal graphitization found by Westraadt [71] of 800 °C, and at below the 700 °C found in Chapter 5 to minimally damage the bulk of a PCD disc during from a 1 h heat treatment. Potential mechanisms for the increased wear rate include oxidation of the surface, which promotes crack nucleation, or a change in stress state on the surface due to the differential thermal expansion coefficients of diamond and cobalt. These are distinguished in Section 7.4.

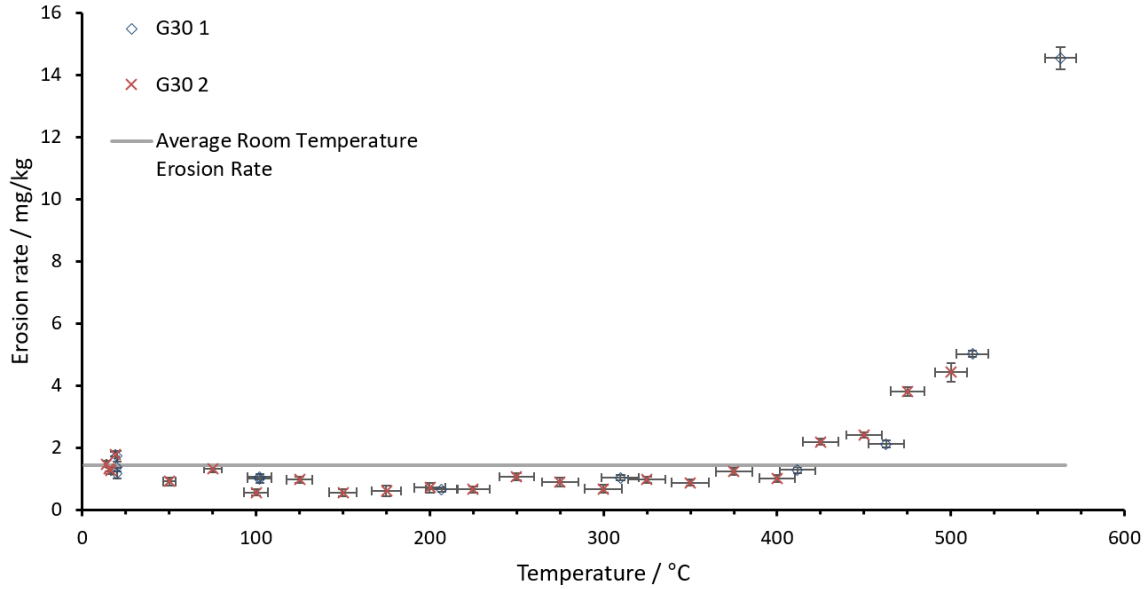

Fig. 7.1 The response of two discs of G30 PCD to high temperature erosion. The discs were eroded at room temperature initially and then each increment was performed at a higher temperature. Increments were 500 g of F36 mesh SiC, except at temperatures over 500 °C when less erodent was used to preserve the apparatus.

An SEM image of a section of PCD near the surface after erosion at 550 °C is shown in fig. 7.3. In contrast to the images presented in Section 4.8, a new phase has appeared across the surface and within the cracks propagating down from the surface. As it was less than 100 nm thick, EDX analysis was not able to give any insight into the constituents of the phase, but it is likely that interaction of diamond with oxygen at the surface at high temperatures in the presence of cobalt has converted the sp^3 diamond into sp^2 amorphous carbon, which may or may not be oxidised. Raman spectroscopy was performed but was not able to confirm this change.

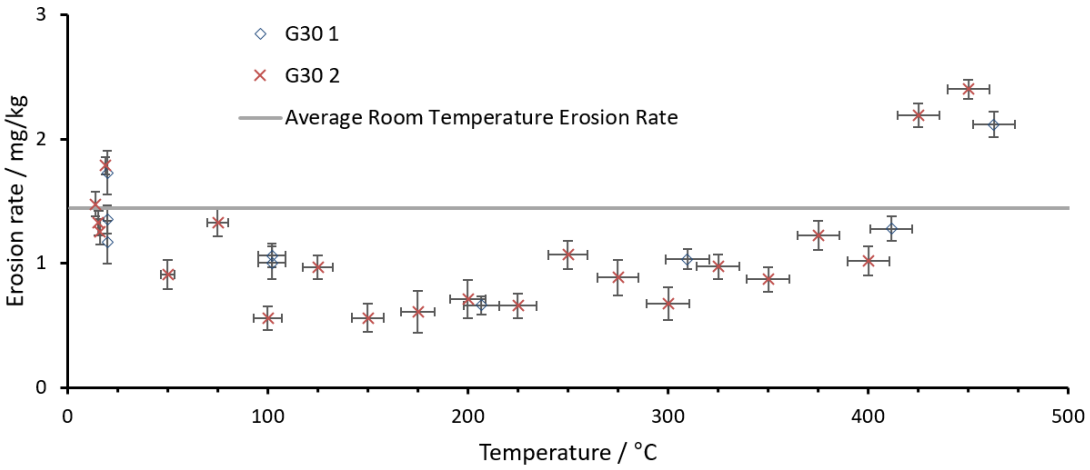

Fig. 7.2 A more detailed view of the data presented in fig. 7.1.

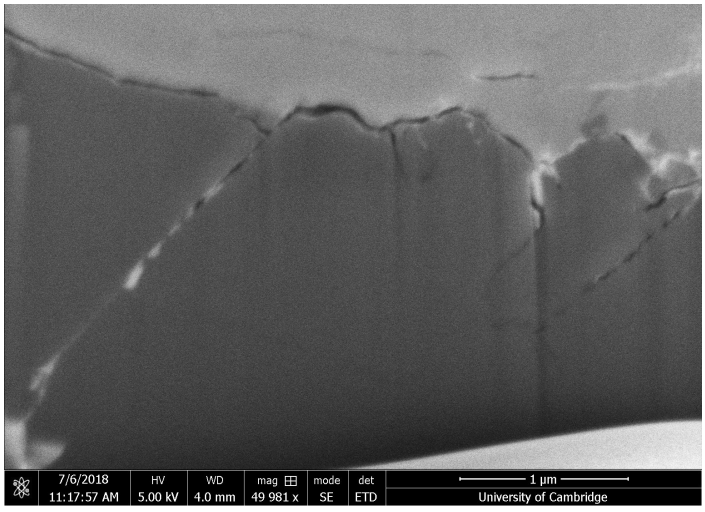

Fig. 7.3 An SEM image of a section of G30 PCD after erosion at 550 °C. Cracks are seen to propagate down from the surface and a thin darkly contrasting layer attributed to amorphous carbon, possibly oxidised, is visible between the diamond and the deposited platinum layer.

A second experiment was performed during which G30 PCD discs were eroded for a number of increments at the same temperature. Fig. 7.4 shows the mass loss of each disc with total erodent impacted. In contrast to the data in fig. 7.1, trends in erosion rates with temperature can be visualised more clearly, however as different discs were used, this adds a small error into the absolute erosion rates of each sample.

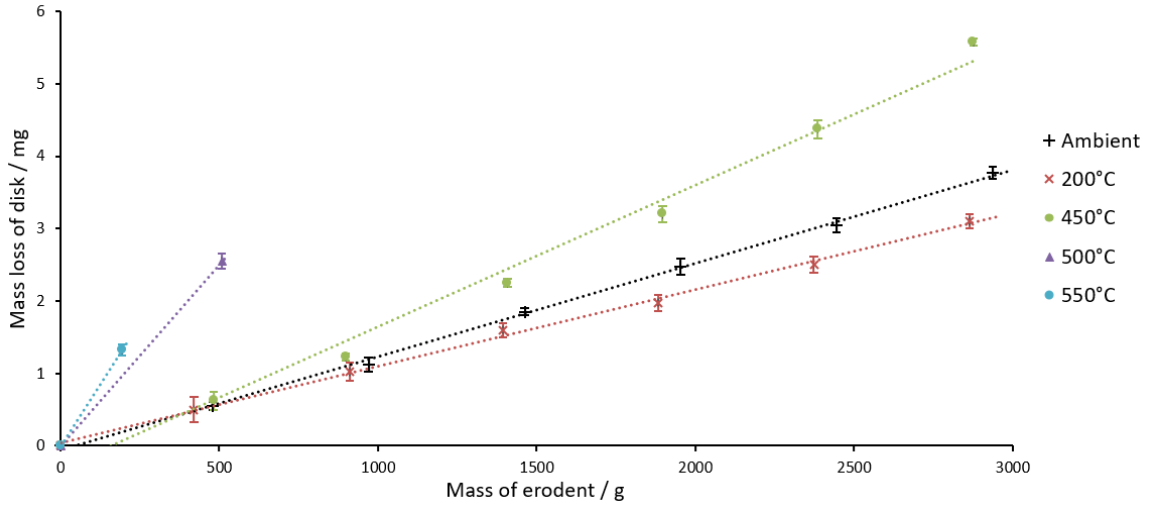

Fig. 7.4 The erosion profiles of separate G30 PCD discs eroded repeatedly at the same temperature. Straight lines have been added to each series as a guide. At higher temperatures, only a single increment was performed in order to protect the apparatus. The error in the temperature is of the order $\pm 10\,^{\circ}\mathrm{C}$.

The decreased erosion rate at 200 °C is also observed in fig. 7.4. The increased erosion rate with temperature is shown by the sample eroded at 450 °C, with far accelerated erosion rates at even higher temperatures. Further increments were not performed on the discs eroded at 500 °C and 550 °C as a precaution to avoid the risk of damage should either disc to have fractured.

The sample eroded at 450 °C has an erosion rate which changes with time. The initial increments produced rates very similar to those at ambient temperature, but on eroding further, the rate increased and the profiles diverged. During each erosion increment, the PCD disc spends 5 min at the designated temperature, and is also heated during the warming up

and cooling down periods. It appears that the cumulative time spent at 450 °C is causing the increased erosion rates, implying that surface damage is time-sensitive and penetrates further than the depth of erosion caused by a single increment (of order 10 µm).

7.3 The Effects of Grain Size and Reducing the Binder Phase

To investigate how the different grades of PCD responded to high temperature erosion, a G12 PCD disc and a RBPCD G30 disc were eroded at high temperatures in the same manner as the G30 discs tested previously. The rate, normalised to the erosion rate of each grade at room temperature, are compared in fig. 7.5. As expected, the room temperature erosion rates vary significantly, with the G12 being the most erosion resistant whilst the RBPCD G30 grade is highly susceptible to erosion.

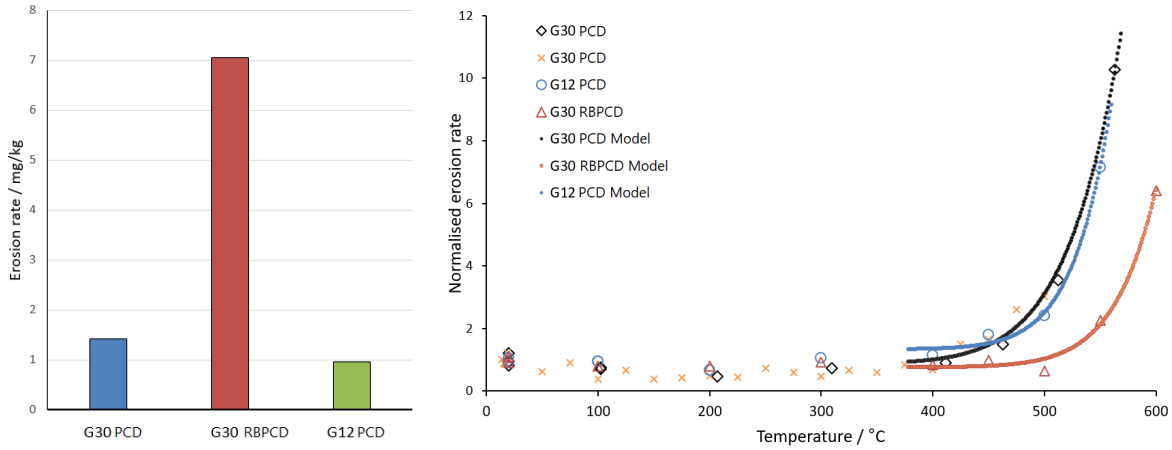

(a) (b)

Fig. 7.5 Fig.(a) shows the room temperature erosion rates of the three grades. Fig.(b) shows the response of the PCD grades to high temperature erosion, but normalised to their room temperature erosion rate. The discs were eroded at room temperature initially and then each increment was performed at a higher temperature. Error bars have been removed for clarity, and an Arrhenius model is fitted to the data for temperatures of 400 °C and above. The Arrhenius activation energies are $(69 \pm 10)\,\mathrm{kJ\,mol^{-1}}$, $(52 \pm 13)\,\mathrm{kJ\,mol^{-1}}$ & $(45 \pm 21)\,\mathrm{kJ\,mol^{-1}}$ for the G30 PCD, the G12 PCD and the G30 RBPCD respectively.

As the temperature increases, the G12 PCD responds in a very similar manner to the G30, with the erosion rate decreasing initially towards 200 °C before increasing at temperatures between 400 °C and 450 °C. The RBPCD grade performs similarly at lower temperatures, with a decrease in erosion rate in the region of 200 °C but the increased erosion rate with temperature occurs at the higher temperature of 550 °C. The reduced cobalt content in the RBPCD sample is reducing chemical damage to the surface. Although the normalised erosion rate at 550 °C is lower, the absolute erosion rates (by weight, the RBPCD sample will be less dense) are very similar. As such, reducing the binder content has not improved the high temperature response except in the extreme of very high temperatures.

7.4 Ambient Temperature Erosion of PCD Previously Eroded at High Temperatures

The way that high temperatures affect erosion rates raises the question of whether or not the effect is reversible. If the thermal soak was causing graphitization within the bulk, thought unlikely due to the moderate erosion rates obtained after a heat treatment in Chapter 5, the effect of a heat treatment would be irreversible and the PCD would be permanently damaged. If the change in erosion rates was caused by temporary changes in residual stresses, the effect would be completely reversible on return to room temperature. However, if the residual stresses were large enough to cause internal cracking, permanent damage would be present. Oxidation would affect only the surface, and so surface damage would be observed without damage to the bulk.

In order to test whether the erosion rates were reversible with temperature, the G30 discs that had previously been eroded at high temperatures in this chapter were eroded on the opposite face at room temperature under identical conditions to each other. The results are presented in fig. 7.6 and show that the initial erosion increment is larger for the disc eroded at the highest temperature, but after that the erosion rates are mostly constant, and consistent

between the discs. Any variation in long term erosion rate can be attributed to the inherent variation in erosion rate between discs which, although small, will be present.

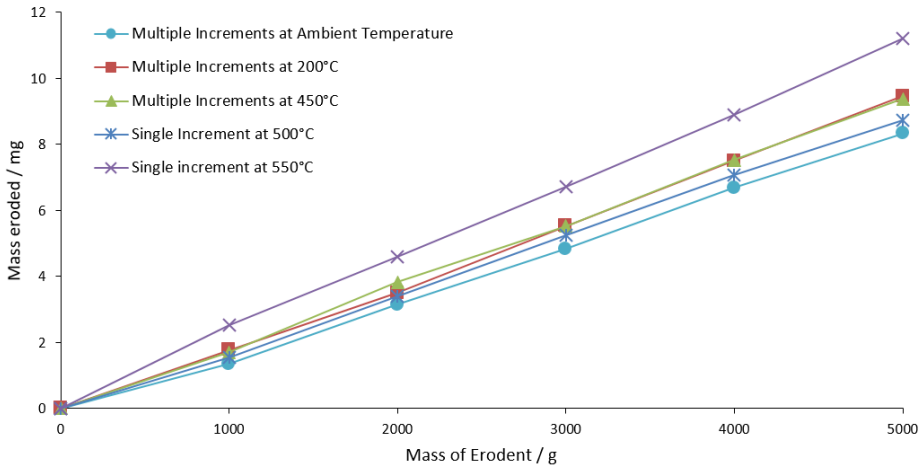

Fig. 7.6 SPE at room temperature has been performed on the rear surface of G30 PCD discs which have previously been eroded at high temperatures on their front faces. The graph shows the mass loss with mass of erodent for these samples and the conditions under which high temperature erosion were performed for each disc are detailed within the key. The erosion rates are mostly constant except for the very first increment of the sample that had previously been eroded at the highest temperature.

The change in erosion rate at high temperatures seems to be reversible in the bulk, but the surface of the sample eroded at 550 °C shows an increased erosion rate in the first increment. The primary mechanism of thermal damage that only affects the surface is oxidation, which has been shown by Jaworska *et al* [8] by DTA-TG to occur on PCD at temperatures above 400 °C. However, oxidation has not been observed as a major degradation process in previous wear tests.

7.5 Discussion and Conclusions

The method for performing high temperature SPE developed in Chapter 6 has been successfully employed at temperatures up to 600 °C. The erosion rate of PCD has been shown to vary with temperature for the first time, with the potential mechanisms including

bulk graphitization, surface oxidation, cobalt softening, and differential thermal expansivities between diamond and cobalt.

On heating freestanding PCD discs to moderate temperatures of 200 °C, the erosion rate was found to reduce from that measured at room temperature consistently across G30 PCD and RBPCD grades, and the G12 PCD grade. The improved wear resistance was unexpected, as it has not previously been observed in literature wear or thermal tests (Chapter 2, Section 2.3.2). The mechanism for the reduced erosion rate has not been determined, however it is possible that either the softening of the cobalt binder on heating, or a change in the residual stress state at the surface of the PCD disc due to the increased temperature and small thermal gradient across the disc are causing the decrease.

The subsequent increase of the erosion rate with temperature is of greater relevance to drilling or cutting applications and is more similar to what might be expected from previous high temperature experiments on PCD. The moderate temperature at which wear increases, of between 400 °C and 450 °C, is well below the expected threshold for graphitization of 650 °C to 700 °C found in Section 5.3, which means that graphitization is an unlikely candidate for the thermal degradation during high temperature SPE. Erosion at room temperature after high temperature erosion showed that the bulk of the PCD was not affected by the short time spent at temperatures of up to 550 °C, in agreement with prior erosion experiments on heat treated samples. However, the surface was damaged by the temperature at 550 °C which indicates that a surface process, most likely oxidation, is responsible for increased erosion rates at high temperatures. A very thin layer of material was observed in an SEM on the surface of the PCD after erosion at high temperature which further supports the hypothesis that surface oxidation is the primary mechanism which accelerates erosion at high temperatures.

Chapter 8

Erosion at Temperatures Below Ambient

8.1 Introduction

SPE performed at high temperatures in the previous two chapters showed that the mechanical properties of PCD can vary across even small temperature ranges. The set of apparatus which had been constructed to perform high temperature SPE could be modified to produce erosion at low temperatures by removing the heating elements and replacing with a cooling mechanism.

The potential importance of cold erosion includes quantifying the erosive damage caused to wind turbine blades in cold climates, and the erosion of extraterrestrial objects on planets such as Mars where temperatures can be as low as $-85\,^{\circ}\mathrm{C}$ and there are regular dust storms with particles of size $50\,\mu\mathrm{m}$. With more relevance to the tooling industry, cryogenic cooling of the PCD cutters which are used to mill Ti-6Al4V stacks has been investigated [15]. Although the PCD cutting face is still expected to reach high temperatures, the liquid nitrogen cooling is used in the body of the tool in order to increase the cutting speed without increasing the tool temperature.

The potential scope for studying materials through low temperature erosion experiments is wide, encompassing the brittle/ductile transition temperature in a range of metals and alloys, and the interesting low temperature properties of polymers.

To the best of the author's knowledge, continuous-stream SPE, as has been performed throughout this thesis, has not previously been performed at temperatures lower than ambient and so the following review spans only similar applications.

8.2 Motivation and Similar Experiments

Extraterrestrial Applications

At the Phoenix lander site on Mars, the wind speed ranges from $4\,\mathrm{m\,s^{-1}}$ at night to between $1\,\mathrm{m\,s^{-1}}$ to $12\,\mathrm{m\,s^{-1}}$ during the daytime [153] and temperatures range from $-30\,^{\circ}\mathrm{C}$ to $-85\,^{\circ}\mathrm{C}$. Dust storms can form which typically contain $50\,\mu\mathrm{m}$ sized particles, often iron oxides. SPE on Mars has been studied for two contrasting reasons, firstly to ensure that sensor components or solar panels on any lander are not eroded by dust storms, and secondly over much longer timescales to study the effect of atmospherically-borne sand on geological features.

Tests simulating the Martian atmosphere have been performed at a cold wind tunnel facility at Aarhus University. The method involves a re-circulating wind tunnel of cross-sectional dimensions $1\,\mathrm{m} \times 2\,\mathrm{m}$, capable of temperatures below $-170\,^{\circ}\mathrm{C}$ and wind speeds in the range $1\,\mathrm{m\,s^{-1}}$ to $25\,\mathrm{m\,s^{-1}}$, into which dust particles can be released [154]. The primary concern of experimenters appears to be calibration of meteorological sensor systems in extreme environments (including terrestrial ones) [155] and often it is sand deposition, not erosion, that was found to cause issues with sensor systems. Were truly erosive conditions to be present, the wind tunnel facility itself would erode and the re-circulating design would re-impact fractured erodent onto any test material, both of which would make for an unreliable test.

In none of the studies referenced in this Section are the material properties or damage to materials at low temperatures studied. Deposition of dust is discussed when discussing sensor performance, which indicates that scientific equipment on Mars is potentially more vulnerable to these processes.

Wind Turbine Applications

A recent review of erosion of the leading edge of wind turbine blades by Slot *et al* [156] discusses temperature only in the context of repeated impacts warming the surface. The potential change in damage mechanism with a reduced temperature is not mentioned. Similarly, a review by Bartolomé *et al* [157] describes rain erosion of wind turbine blades but does not discuss their operation in potentially cold environments, such as power generation in communities near the Earth's poles.

Aerospace Applications

A typical study on the performance of thermoplastics specific to aerospace applications discusses the high temperature properties, such as the stability at certain temperatures, but does not give details of wear rates at low temperatures [158] which may be encountered during operation. Hysteresis heating under repeated impacts can warm the substrate, and so high temperatures are often of more general interest [159]. Low temperature studies seem to focus on the formation of ice on surfaces and how this changes wing profile, and hence lift [160].

Cryogenic wind tunnels exist and are capable of a range of velocities and temperatures as low as 77 K, limited by use of liquid nitrogen. These appear to be used mainly for simulation of flow [161], especially at high Reynold's number and use of these wind tunnels for SPE has not been reported. 'Icing tunnels' use refrigeration devices to cool the air in a wind tunnel and spray water to test the build up of ice on aerospace components, at typical temperatures

of $-30\,^{\circ}\mathrm{C}$, and over a wide range of velocities. Erosion is discussed, but only in the context of removal of the ice deposits [162].

Hail impact is a concern for aircraft manufacturers, and the impact of ice spheres onto aircraft laminates has been tested [163]. In these experiments however, the icy projectile was cooled but the substrate was held at ambient temperature. Similar experiments and modelling of ice impact onto ambient temperature substrates have been performed by Kim & Kedward [164] and Wang, Field *et al* [165]. The effect of cooling the test material is not investigated.

Summary

Evidence for the use of low temperature SPE to measure wear has not been found in the literature, motivating the development of a modified version of the Cavendish apparatus to perform erosion at temperatures below ambient.

8.3 Method and Apparatus

8.3.1 Initial Approach with Peltier Modules

The apparatus which was used to perform high temperature SPE demonstrated that it was possible to separate the erodent and the airflow so that a target can be heated with only a moderate heater power being required. Using the same approach, the same set of apparatus can be used to cool a substrate below ambient temperature. An initial approach employed a water heat exchanger, using water cooled to $10\,^{\circ}\mathrm{C}$, and a series of three stacked Peltier modules each capable of operating at up to 82 W, as shown in fig. 8.1.

Theoretically, if the Peltier modules were to be operating at 50% efficiency, they would be capable of a cooling power of 123 W. However, the combination of the Peltier modules and the water heat exchanger was not able to remove heat from the sample holder at a fast enough rate to enable sufficiently low temperatures for useful cold erosion. With the air flow

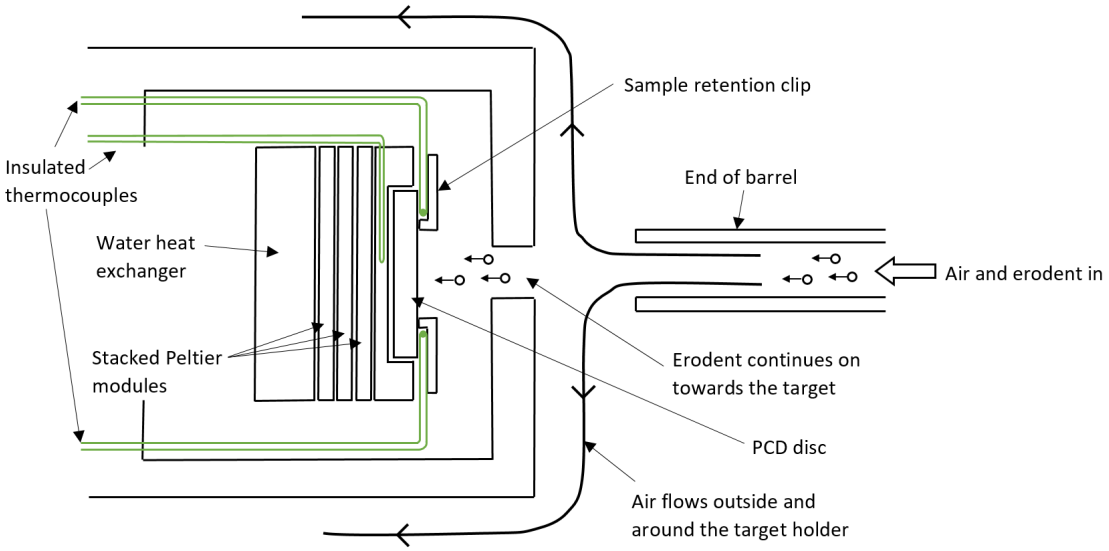

Fig. 8.1 A schematic of how erosion at below ambient temperature can be obtained using a combination of water cooling and stacked Peltier modules. The water was cooled to 10 °C and the Peltiers were capable of a power of up to 82 W.

on, the minimum temperature of a thermocouple glued to the front face of a PCD disc within the sample holder was −18 °C, which was not deemed sufficiently low to perform useful measurements.

8.3.2 Revised Approach with Liquid Nitrogen Cooling

A revised approach was designed which would use liquid nitrogen to cool the substrate. The Peltier modules were replaced with a block of copper with a large thermal mass and a high thermal conductivity. Compressed helium gas was piped through a second heat exchanger placed within a bucket of liquid nitrogen, before flowing into the heat exchanger placed within the sealed box. A schematic of the apparatus is given in fig. 8.2 with an image of the inside of the sealed box in fig. 8.3. The helium left the nitrogen bucket at temperatures near to the boiling point of N_2 (−196 °C) and the degree of cooling was controlled by changing the helium flow rate, with higher flow rates producing lower temperatures.

In the same manner as for erosion at high temperatures, the velocity of the erodent was held at $(80 \pm 6)\,\mathrm{m\,s^{-1}}$ throughout all of the tests at low temperatures.

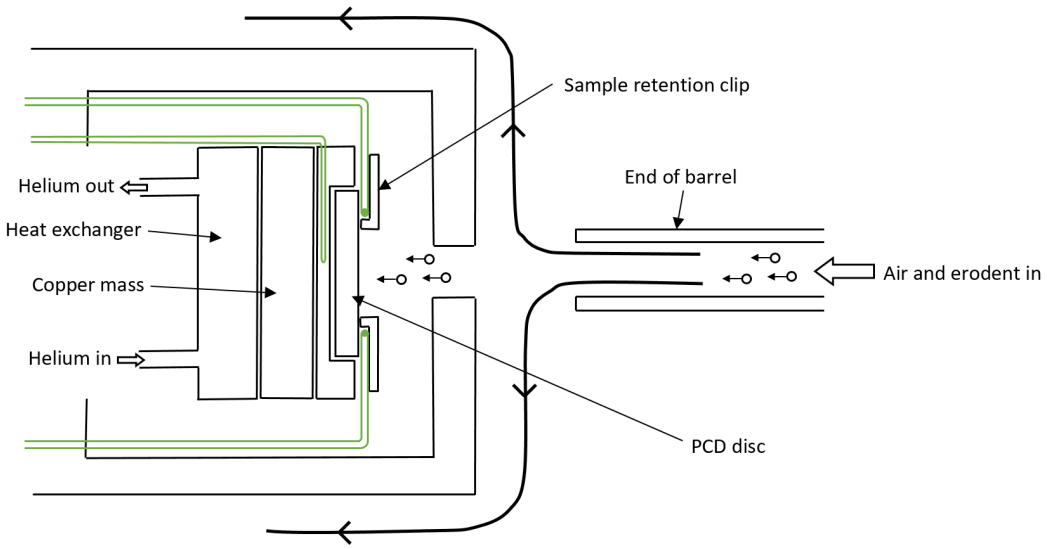

Fig. 8.2 A schematic of the cold erosion apparatus used for subsequent experiments. Helium gas at close to liquid nitrogen temperatures flows through a heat exchanger behind the sample, and is capable of reducing the temperature to −100 °C.

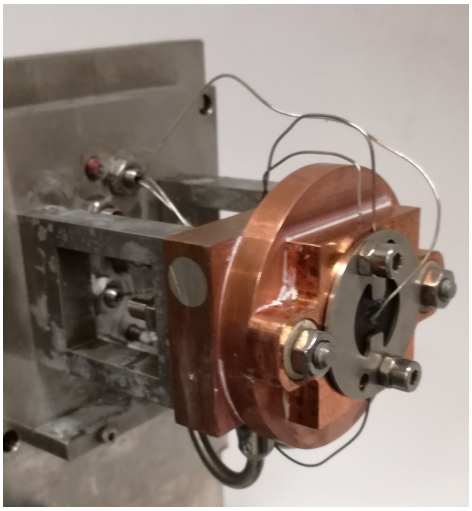

Fig. 8.3 An image of the sample holder and heat exchanger which are located within the high temperature erosion apparatus imaged in fig. 6.6. The apparatus is set up for calibration with a thermocouple glued to the front face of the PCD target, which will be used as a reference for the other thermocouples which surround the sample.

8.4 Tests on 316L Stainless Steel

Due to the limited availability and low erosion rate of PCD, an alternative target of 316L stainless steel was chosen for initial tests using the low temperature SPE apparatus. As the results obtained are also novel, and provide some insight into the temperatures obtained during low temperature SPE, they are included here. AISI 316L stainless steel is austenitic in type, meaning that it has a very low carbon content, and was chosen due to the ease with which it can be procured and machined, and for its medium-range erosivity.

8.4.1 Erosion Properties of Austenitic Stainless Steels

Stainless steels have been subjected to SPE in a number of studies, e.g. [166, 167], with applications varying from turbine blades and valves, to piping and food processing equipment. Wear occurs by a combination of the detachment of large fragments and the action of pitting and cutting, typical for ductile materials. These ductile mechanisms will contrast with the purely brittle mechanisms found during erosion of PCD. The austenitic type of 316L means that on cooling, the impact resistance should not change and a discrete brittle/ductile transition will not be seen [168]. However, as the temperature is reduced, the toughness also reduces and so it is expected that the erosion rate will increase.

8.4.2 Results

Four separate stainless steel discs were each eroded with a single increment of 100 g of F36 mesh Al_2O_3 at temperatures down to $-80\,^{\circ}\mathrm{C}$. The erosion rates at the four different temperatures used are given in fig. 8.4. As the temperature is decreased, the erosion rate was found to increase. The decreased toughness of the steel at lower temperatures is preventing energy absorption and increasing the likelihood of cracks forming and subsequent mass loss at rates higher than for the more ductile mechanisms.

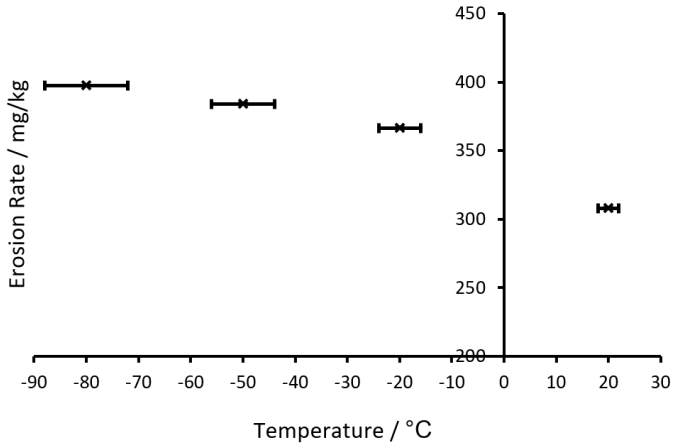

Fig. 8.4 The erosion rates of 4 separate 316L stainless steel discs when subjected to a single increment of erosion using 100 g of F36 mesh Al_2O_3 erodent at a velocity of $(80 \pm 6)\,\mathrm{m\,s^{-1}}$ and at temperatures lower than ambient. The error in the temperature arises from the difference between the values read by the two thermocouples clamped to the sample's surface. The error in the erosion rate is of the order of $1\,\mathrm{mg\,kg^{-1}}$ and so is not displayed on the graph. The discs were eroded in the order: Ambient, $-50\,^{\circ}\mathrm{C}$, $-80\,^{\circ}\mathrm{C}$ and $-20\,^{\circ}\mathrm{C}$, and the alumina erodent did not noticeably damage any of the erosion apparatus.

During this trial erosion, the potential issue of frosting became apparent. Water moisture in the air near the cool sample can condense and form ice on the surface. As the temperature is reduced further, the rate of ice formation increases. However, it can be seen from the erosion of stainless steel at low temperatures that the ice has not protected the surface and so it can be concluded that the ice is rapidly removed by incoming erodent. It is assumed throughout any analysis that the erosion rate of ice is much faster than that of the test material, which can be justified for PCD by the expectation that PCD is significantly more erosion resistant, and so the issues due to frosting can be ignored.

To conclude from this Section, the method for performing SPE at temperatures below ambient is successful and data has been acquired for 316L stainless steel.

8.5 Low Temperature Erosion of PCD

A single G30 sample of PCD was subjected to four 500 g increments of erosion with F36 mesh SiC at ambient temperature, before four further increments at $-50\,^{\circ}\mathrm{C}$, then another

four at −100 °C. Fig. 8.5 displays the temperatures recorded by the thermocouples during erosion increments at the three temperatures. In order to reduce the quantity of helium used as a heat exchanging gas, minimal time was allowed for the sample temperature to equilibrate and so the flow rate of the helium was continuously adjusted in order to maintain a constant erosion temperature.

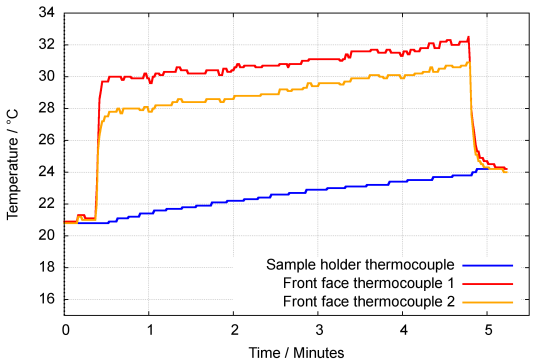

(a) Erosion at ambient temperature.

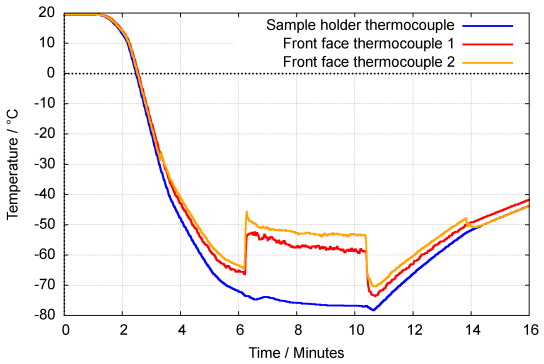

(b) Erosion at −50 °C.

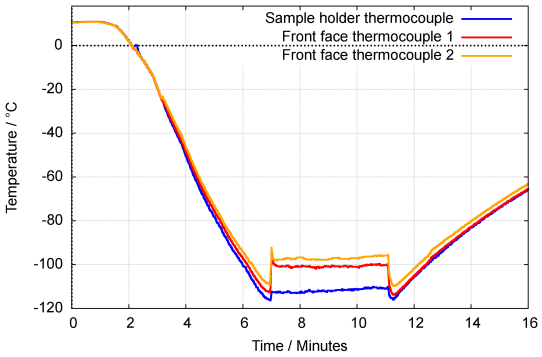

(c) Erosion at −100 °C.

Fig. 8.5 Example temperature vs time profiles for the three thermocouples placed around the sample during low temperature erosion at each of the three temperatures tested. During each test, the temperature increases over the 4 min period that the erodent is impacting the sample. At ambient temperature, no active cooling was employed.

The time during which the erodent is impacting the sample can be clearly seen by the increase in temperature of the thermocouples clamped to the front face of the PCD in fig. 8.5. At ambient temperature, the increase is around 10 °C, but at colder temperatures it is closer to

20 °C. Unlike during the hot erosion in the previous two chapters, the cold erosion apparatus does not contain a mechanism for cooling the small hole through which the erodent enters. The erodent impacts at ambient temperature and warms up the target by being in thermal contact with it, if only briefly, and by the conversion of a small proportion of its kinetic energy into thermal energy on impact. The extent to which warming occurs cannot be quantified precisely, however the thermocouples clamped to the front face of the PCD are used to give an indication of the amount of warming present.

The raw erosion data at the three temperatures are shown in fig. 8.6 and show a large amount of scatter but there is an indication that the erosion rate is increased at −50 °C. Although the differences in erosion rate with temperature can be seen, every third increment produced a significantly lower erosion rate than expected. On re-analysis of the experiment, it was noted that the alumina bush placed at the entrance to the sealed box was worn asymmetrically and that it was replaced after every third increment. A small misalignment between the erosion barrel and the opening through which the erodent passes was causing less erodent to hit the target and a reduced erosion rate for the first increment, after which the bush would widen due to it being eroded and would allow erodent to pass through it again. For the second and third increments using each alumina bush, the bush no-longer prevented direct erosion impacts and so the data can be used with more confidence. The data is re-plotted by temperature in fig. 8.7, without including the compromised increments, and shows that the erosion rate does change as temperature is reduced.

The mass lost per increment at ambient temperature is very similar to the 0.72 mg measured at ambient temperature using the high temperature SPE apparatus. As the geometries of the experiments are the same, the same sealed box is used, and the only difference between the experiments is the material of the sample holder, and so the same erosion rate is expected.

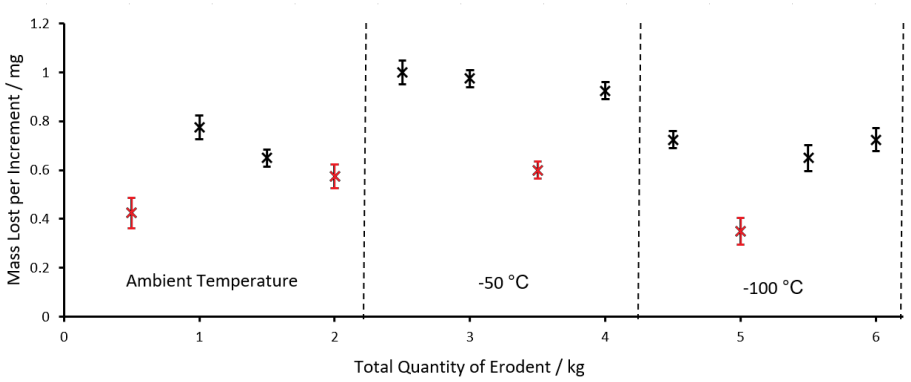

Fig. 8.6 The mass losses for each of the twelve 500 g erodent increments performed a G30 disc at $(80 \pm 6)\,\mathrm{m\,s^{-1}}$ are shown in order. The first four increments were performed at ambient temperature, before four at $-50\,^{\circ}\mathrm{C}$ and four at $-100\,^{\circ}\mathrm{C}$. Every third increment is highlighted in red, as the alumina bush located at the orifice of the sealed box was replaced before each of them and a notably smaller erosion rate is measured.

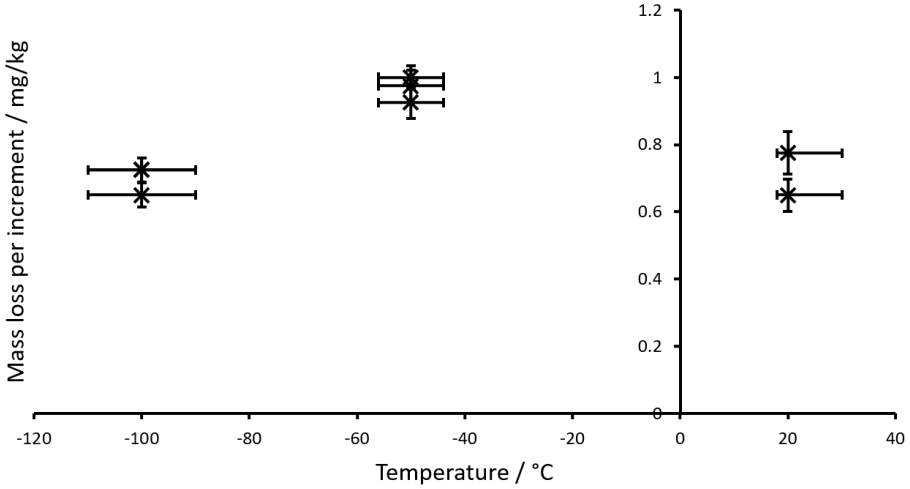

Fig. 8.7 The erosion rate of G30 PCD at temperatures below ambient. A single sample was tested with the mass loss at the highest temperatures being measured before any cooling occurred.

As the temperature is reduced to $-50\,^{\circ}\mathrm{C}$, the erosion rate increases by 33%. The relationship continues the trend observed at temperatures up to $200\,^{\circ}\mathrm{C}$, which was hypothesised to be caused by the properties of the cobalt binder changing. Lower temperatures inhibit dislocation motion, preventing energy absorption and reducing the ability of cobalt to arrest cracks.

At the lowest possible temperature that could be obtained by the apparatus, $-100\,^{\circ}\mathrm{C}$, the erosion rate has reduced as the wear resistance has improved. The reasons for this are unknown but the possibility that ice formation on the surface is preventing direct collisions between the SiC erodent and the PCD cannot be ruled out.

8.6 Summary and Conclusions

A novel method for performing SPE at temperatures lower than ambient has been developed and has successfully eroded stainless steel and PCD at temperatures as low as $-100\,^{\circ}\mathrm{C}$. The properties of both materials were shown to change at lower temperatures. The erosion rate of 316L stainless steel, which could be measured with very low errors, increased as the temperature was reduced, which is a continuation of trends observed at higher temperatures.

Low temperature erosion of PCD showed that on a moderate reduction of temperature, the erosion rate increased. The consequences for cryogenic machining applications are that there is potential for a PCD tool to wear at a faster rate when chilled.

There is scope for using the low temperature SPE developed here to measure the properties of non-PCD materials which are used in other applications. Oil and gas pipelines in cold areas may be subjected to slurry erosion, the rate of which may be temperature dependent. Wind turbines can operate in cold environments and materials that coat them should be tested at the temperatures at which they will be used.

Chapter 9

Conclusions & Further Research

9.1 Summary & Conclusions

In this thesis, a series of SPE experiments were presented, which provided an insight into the fracture and wear mechanisms of PCD in erosive environments. Particular emphasis was given to the effect of high temperatures by heat treating samples before erosion or by heating samples in-situ during SPE experiments. Further experiments were performed at temperatures below ambient to show that the concept was possible and to extend the temperature range over which the erosion rate of PCD has been measured.

Chapter 2 discussed the mechanical properties of diamond and described how the manufacture process of PCD leads to the formation of a material with its unique combination of hardness and toughness. The mechanical and thermal properties which had previously been measured by other researchers were introduced, with a focus on those most pertinent to erosive behaviour and crack formation. During a survey of the responses of PCD to thermal stimuli, the mechanisms by which degradation could occur were identified as graphitization of the bulk, oxidation of exposed surfaces, and the differential thermal expansivities of cobalt and diamond altering the residual stresses on heating. The specific PCD grades used during

this thesis were identified and a discussion of the possibility of reducing the binder phase and how it affects the microstructure of PCD was given.

In Chapter 3, the SPE experiment and the procedure by which a large number of individual erodent particles can be impacted onto a surface in a continuous stream was introduced. The repeated impacts were discussed alongside the principles of Hertzian contact theory, together with the mechanisms of crack formation during both blunt and sharp impacts. Standard erosion theories, derived for homogeneous isotropic materials, would need to be modified to account for the biphasal polycrystalline microstructure present in PCD. Limited previous SPE of PCD had been performed prior to this thesis, with only SiO_2 erodents used, and little information about the wear of PCD was obtained.

Chapter 4 presented the first experimental results of the thesis. The wear rates achieved with three erodents, SiO_2, Al_2O_3 and SiC, were compared. The high hardness of SiC produced the highest erosion rates by far. Here it was shown that SPE of PCD to depths beyond just the surface grains was possible, and that erosion could be used to test wear rates. Eroding three different monomodal grades of PCD found that the erosion rate decreased as the grain size decreased, but also found that reducing the binder phase reduced erosion resistance by a factor of between 5 and 8, which was unexpected. The velocity exponents were measured for the three monomodal grades, and all were lower than the values predicted for brittle materials, which indicated that the microstructure of PCD was affecting the erosion mechanism. Erosion on G30 PCD at angles as small as 30° to the surface confirmed that the dominant failure mode was brittle fracture.

A detailed microstructural study was performed using SEM images taken before and after erosion increments, to identify the mass loss mechanism. Deposition of SiC on the surface during erosion was found to obstruct the view of the PCD in some places, but the technique of step-wise erosion, combined with repeated imaging, was able to observe the mechanism by which the surface changed with time. The cobalt was eroded preferentially and very rapidly,

followed by fractures at the exposed edges of diamond grains. Fractures were typically under 5 μm in length, and the dominant material loss mechanism was sub-grain sized chipping. The features present on the eroded surfaces depended on the grain size of the PCD, with partially developed HCCs visible on the surface of the finest grade, G2, which became more prominent with an increased erodent velocity. HCCs were not present on eroded G30 surfaces unless a significantly larger erodent was used. Sectioned images of both HCCs and microfractures near the surface were consistent with the mass loss mechanisms identified previously, and helped to identify the role of cobalt in arresting cracks by observing crack bifurcation and termination in cobalt pools.

Having developed a model for the erosion of PCD, SPE was employed as a wear test in Chapter 5 to learn more about how the properties of PCD can be altered to increase erosion resistance. By analysis of a set of samples sintered at a range of temperatures and pressures, it was found that both higher pressures, across the range 5.5 GPa to 8 GPa, and lower temperatures, across the range 1350 °C to 1450 °C, were preferred to reduce erosion rates. The use of erosion enabled wear rates from a limited number of samples to be obtained with comparatively small errors and, over the course of 8 erosion increments, trends could be clearly identified.

Erosion of samples that were heat treated for 1 h to 6 h in a vacuum at temperatures up to 850 °C demonstrated the degradation of the bulk of PCD after prolonged exposures to high temperatures. As in previous experiments, the erosion rate was consistent with depth, which demonstrates that the surface is not more greatly affected by a vacuum heat treatment than the bulk. Above 700 °C, the longer the time or the higher the temperature of a heat treatment, the higher the subsequent erosion rate would be. A heat treatment performed in air, or on RBPCD samples where oxygen would remain present in capillaries between the diamond grains, severely degraded the microstructure of the PCD and made the material highly susceptible to erosion. The depth of surface damage was measured by identifying the

point at which the erosion rate reduced from the increased surface rate, to that of the bulk. By changing the atmosphere under which heat treatments were performed, the relative effects of oxidation and graphitization can be determined and it was clear that under the conditions studied here, surface oxidation is the more dominant mechanism for determining changes in erosion rate with temperature. Here, surface oxidation is initiated at lower temperatures than graphitization of the bulk, and the evidence suggests that the greatest factor affecting the erosion resistance of PCD at temperature in Chapter 7 is the deterioration of the surface in the presence of oxygen.

Chapter 6 introduced the concept of performing SPE at high temperatures. No evidence for prior high temperature SPE of PCD has been found, although high temperature SPE has been performed on other materials, including metals and ceramic coatings. Typical high temperature erosion facilities, such as the apparatus present at the NPL, are inappropriate for erosion of PCD due to the highly abrasive conditions that are required and the damage to apparatus that will be caused by such an environment. A new facility was developed, capable of eroding PCD at temperatures up to 600 °C, which only required a fraction of the heating power of some alternative methods.

In Chapter 7, PCD was eroded at high temperatures. Moderate increases in temperature towards 200 °C decreased the erosion rate by a factor of two. The mechanism for this is not well understood as the mechanical properties of PCD measured by other methods were not found by others to change significantly across this temperature range. Further increases of temperature above 400 °C were found to result in increased erosion rates, which was in keeping with previous data showing that surface oxidation can occur at these temperatures. Reducing the binder phase improved the relative performance at high temperatures, delaying the increase in erosion rate with temperature. However, at all but the highest of temperatures the improved thermal resistance of the RBPCD sample did not overcome the inherent susceptibility of the RBPCD to erosion, and so the absolute erosion rate (in $\mathrm{mg\,kg^{-1}}$) was

found to be lower for the PCD. When samples which had previously been eroded at high temperatures were re-eroded at room temperature, the long term erosion rates examining the bulk of the samples were unaffected by the high temperatures that the PCD had previously encountered for short periods. Only the first increment, which tests the integrity of the PCD nearest the surface, deviated from the long term erosion rate, providing the most clear demonstration that the increased erosion rates with temperature were primarily caused by surface oxidation.

Chapter 8 introduced the concept of performing SPE at temperatures lower than ambient, which as far as a detailed literature survey could tell, has not been previously performed. Liquid nitrogen was used to cool helium gas which was then used to cool the sample in-situ. Erosion of 316L stainless steel proved that the concept of low temperature erosion was feasible, and that erosion rates could vary as material properties changed at low temperatures. Erosion of PCD was less clear due to the very low rates involved, but indicated an increased erosion rate at temperatures as low as $-50\,^{\circ}\mathrm{C}$, which would be a continuation of the trend seen at increased temperatures, before a reduction to the room temperature rate as the sample was further cooled to $-100\,^{\circ}\mathrm{C}$.

9.2 Potential Areas for Future Research

Erosion of PCD

During this thesis, a variety of erosion experiments have been performed on PCD. The results at ambient temperature produced a reasonably comprehensive model for the erosion of PCD, which could be improved by identifying diamond grain orientation with respect to fracture and HCC growth, to identify whether fractures propagate preferentially on the (111) planes or whether inter- or intra-granular fractures were more prevalent.

The most interesting results involve the response of erosion rates to thermal stimuli, and the relative importance of surface oxidation over the graphitization of the bulk, which is an

issue often referred to in other studies. Erosion of PCD which has been heat treated in air at temperatures below 700 °C could be used to identify the temperature at which the onset of oxidation occurs. The partial pressure of oxygen during a heat treatment could also be varied.

The decrease in erosion rate during SPE at 200 °C has not been explained in this thesis, although softening of the cobalt binder is a potential reason. A comparison of the erosion rate of single crystal diamond at these temperatures, to the room temperature rate, could eliminate the response of the diamond network as a potential mechanism and would build on the high temperature SPE performed here.

Erosion at Temperatures Below Ambient

The introduction of erosion at temperatures below ambient and applying it to the most erosion resistant material in PCD opens up the possibility of testing many other relevant materials. With applications including wind turbine blades in cold environments, aircraft operating at higher altitudes, and slurry erosion of cool piping, there are many different challenges that can be addressed. An excellent candidate for further tests would be a material with a brittle-ductile transition temperature in the region 0 °C to −50 °C, such as a number of the polymers commonly used for piping liquids that may contain erosive particulates.

References

[1] M W Cook and P K Bossom. Trends and recent developments in the material manufacture and cutting tool application of polycrystalline diamond and polycrystalline cubic boron nitride. *Int. J. Refract. Metals Hard Mater.*, 18:147–152, 2000.

[2] A G Evans and E A Charles. Fracture Toughness Determinations by Indentation. *J. Am. Ceram. Soc.*, 59(8):371–372, 1976.

[3] B Lux and P Renard. Diamond for tooling and abrasives. *Diamond & Related Materials*, 1:1035–1047, 1992.

[4] H P Bovenkerk, F P Bundy, H T Hall, H M Strong, and R H Wentorf Jr. Preparation of Diamond. *Nature*, 184:1094–1098, 1959.

[5] H T Hall. Sintered diamond: a synthetic carbonado. *Science (New York, N.Y.)*, 169(3948):868–9, aug 1970.

[6] R H Wentorf. Diamond Tools for Machining. *US Patent 3745623*, 1973.

[7] Varel International Bellin F., Dourfaye, A., King W., Thigpen M. The current state of PDC bit technology. *World Oil*, October 20:53–58, 2010.

[8] L Jaworska, M Szutkowska, P Klimczyk, M Sitarz, M Bucko, P Rutkowski, P Figiel, and J Lojewska. Oxidation, graphitization and thermal resistance of PCD materials with the various bonding phases of up to 800 °C. *Int. J. Refract. Metals Hard Mater.*, 45:109–116, 2014.

[9] S V Kidalov Shakhov, F M, S V Kidalov, and F M Shakhov. Thermal conductivity of diamond composites. *Materials*, 2:2467–2495, 2009.

[10] M J Neale and M Gee. *Guide to Wear Problems and Testing for Industry*. William Andrew Publishing, New York, NY, USA, 2001.

[11] A Lammer. Mechanical properties of polycrystalline diamond. *Mater. Sci. Technol.*, 4:949–955, 1988.

[12] S. M. Walley and J. E. Field. The contribution of the cavendish laboratory to the understanding of solid particle erosion mechanisms. *Wear*, 258:552–566, 2005.

[13] R Narayan. *Diamond-based materials for biomedical applications*. Woodhead Publishing Limited, Cambridge, 2013.

[14] W P Kang, J.L.Davidson, Q Li, J F Xu, D L Kinser, and D V Kerns. A novel low-field electron-emission polycrystalline diamond microtip array for sensor applications. *Sensors Actuators A: Physical*, 54(1-3):724–727, 1996.

[15] Julius Schoop, Wisley Falco Sales, and I. S. Jawahir. High speed cryogenic finish machining of Ti-6Al4V with polycrystalline diamond tools. *Journal of Materials Processing Technology*, 250:1–8, dec 2017.

[16] J E Field. The mechanical and strength properties of diamond. *Rep. Prog. Phys.*, 75:126505, 2012.

[17] R Berman and F Simon. On the graphite-diamond equilibrium. *Z. Electrochem.*, 59:333–338, 1955.

[18] A R Davies and J E Field. The solid particle erosion of free-standing CVD diamond. *Wear*, 252:96–102, 2002.

[19] J E Field. *The Properties of Diamond*. Academic Press, London, 1979.

[20] H Kanda Yamaoka S. Inhomogeneous distribution of nitrogen impurities in {111} sectors of high pressure synthetic diamond. *Diamond Related Mater.*, 2(11):1420–1423, 1993.

[21] A Bhaumik J. Narayan. Novel Phase of Carbon, Ferromagnetism, and conversion into Diamond. *J. Appl. Phys.*, 118(215303), 2015.

[22] F. P. Bundy, W. A. Bassett, M. S. Weathers, R. J. Hemley, H. K. Mao, and A. F. Goncharov. The pressure-temperature phase and transformation diagram for carbon; updated through 1994. *Carbon*, 34(2):141–153, 1996.

[23] J E Field. Mechanical and physical properties of diamond. *Inst. Phys. Conf. Ser.*, 75:181–205, 1986.

[24] J E Field. *The Properties of Natural and Synthetic Diamond*. Academic Press, London, 1992.

[25] H J McSkimin and P Andreatch. Elastic moduli of diamond as a function of pressure and temperature. *J. Appl. Phys.*, 43:2944–2948, 1972.

[26] M H Grimsditch and A K Ramdas. Brillouin scattering in diamond. *Phys. Rev. B*, 11:3139–3148, 1975.

[27] Y Zhang, J Li, L Zhao, and X Wang. Optimisation of high thermal conductivity aluminum/diamond composites produced by gas pressure infiltration by controlling infiltration temperature and pressure. *J. Mater. Sci.*, 50:688–696, 2015.

[28] R H Telling, C J Pickard, M C Payne, and J E Field. Theoretical strength and cleavage of diamond. *Phys. Rev. Letts*, 84:5160–5163, 2000.

[29] J E Field. General properties of diamond. In J E Field, editor, *The Properties of Diamond*, pages 641–653. Academic, London, 1979.

[30] E J Brookes. *The plasticity of diamond*. PhD thesis, University of Hull, 1992.

[31] C Phall and R P Burnand. Tool Component. *US Patent 4861350*, 1989.

[32] N J Pipkin and W I Wilson. Processes occurring during the synthesis of syndite. In *Proc. 28th Diamond Conference*, pages 125–128, Reading, UK, 1977.

[33] C A Brookes, E J Brookes, V R Howes, S G Roberts, and C P Waddington. A comparison of the plastic deformation and creep of type I, type II and synthetic diamonds at 1100C under conditions of point loading. *J. Hard Mater.*, 1:3–24, 1990.

[34] Xiaohui Yu, Paul Raterron, Jianzhong Zhang, Zhijun Lin, Liping Wang, and Yusheng Zhao. Constitutive Law and Flow Mechanism in Diamond Deformation. *Scientific Reports*, 2(1):876, dec 2012.

[35] K Ishida and T Nishizawa. The C-Co (Carbon-Cobalt) System. *Journal of Phase Equilibria*, 12(4):417–424, 1991.

[36] C Liu, Z Kou, D He, Y Chen, K Wang, B Hui, R Zhang, and Y Wang. Effect of removing internal residual metallic phases on wear resistance of polycrystalline diamond compacts. *Int. J. Refract. Metals Hard Mater.*, 31:187–191, 2012.

[37] J Shamburger. Method and apparatus for selectively leaching portions of PDC cutters already mounted in drill bits. *US Patent 7757792*, 2010.

[38] N D Griffin and P R Hughes. Polycrystalline diamond partially depleted of catalyzing material. *US Patent 6739214*, 2004.

[39] R Riedel R.P. Radtke J. Hanaway. Thermally Stable Polycrystalline Diamond Cutters for Drill Bits. In *SPE Annual Techincal Conference and Exhibition*. Society of Petroleum Engineers, Houston, Texas, 2004.

[40] S A Catledge, Y K Vohra, R Ladi, and G Rai. Micro-Raman stress investigations and X-ray diffraction analysis of polycrystalline diamond (PCD) tools. *Diamond Related Mater.*, 5:1159–1165, 1996.

[41] Declan Mcnamara, Patricia Alveen, Signe Damm, Declan Carolan, James H Rice, Neal Murphy, and Alojz Ivanković. A Raman spectroscopy investigation into the influence of thermal treatments on the residual stress of polycrystalline diamond. *Int. J. Refract. Metals Hard Mater.*, 2015.

[42] Hongsheng Jia, Hongan Ma, and Xiaopeng Jia. Research on polycrystalline diamond compact (PDC) with low residual stress prepared using nickel-based additive. *International Journal of Refractory Metals and Hard Materials*, 29(1):64–67, jan 2011.

[43] V Kanyanta, S Ozbayraktar, and K Maweja. Effect of manufacturing parameters on polycrystalline diamond compact cutting tool stress-state. *Int. J. Refract. Metals Hard Mater.*, 45:147–152, 2014.

[44] V Kanyanta, A Dormer, N Murphy, and A Invankovic. Impact fatigue fracture of polycrystalline diamond compact (PDC) cutters and the effect of microstructure. *Int. J. Refract. Metals Hard Mater.*, 46:150, 2014.

[45] Feng CHEN, Gen XU, Chun-de MA, and Guo-ping XU. Thermal residual stress of polycrystalline diamond compacts. *Transactions of Nonferrous Metals Society of China*, 20(2):227–232, feb 2010.

[46] T-P. Lin, M Hood, G A Cooper, and X Li. Wear and failure mechanisms of polycrystalline diamond compact bits. *Wear*, 156:133–150, 1992.

[47] Liu F Fan W. Guo H. Mechanism of the effect of Interface Structure on the Abrasion Performance of Polycrystalline Diamond Compact. *Adv. Materials Research*, 230-232:669–673, 2011.

[48] A D Krawitz, R Andrew Winholtz, E F Drake, and N D Griffin. Residual stresses in polycrystalline diamond compacts. *Int. J. Refract. Metals Hard Mater.*, 17:117–122, 1999.

[49] J W Pagget, E F Drake, A D Krawitz, R Andrew Winholtz, and N D Griffin. Residual stress and stress gradients in polycrystalline diamond compacts. *Int. J. Refract. Metals Hard Mater.*, 20:187–194, 2002.

[50] R Morrell, R Danzer, P Supancic, W Harrer, S Puchegger, and H Peterlik. Mesoscale mechanical testing methods for diamond composite materials. *Int. J. Refract. Metals Hard Mater.*, 28:508–515, 2010.

[51] A A Griffith. The phenomena of rupture and flow in solids. *Phil. Trans. R. Soc. Lond. A*, 221:163–198, 1920.

[52] G R Irwin. Fracture Dynamics. In *Fracturing of Metals*, pages 147–166. Am. Soc. for Metals, Cleveland, Ohio, 1948.

[53] E Orowan. Fracture and Strength of Solids. *Reports on Progress in Physics*, 12:185, 1949.

[54] R W Rice. Fractographic identification of strength controlling flaws and microstructure. In R C Bradt, D P H Hasselman, and F F Lange, editors, *Fracture Mechanics of Ceramics. 1: Concepts, Flaws, and Fractography*, pages 323–345. Plenum, New York, 1974.

[55] D. McNamara, P. Alveen, D. Carolan, N. Murphy, and A. Ivanković. Fracture toughness evaluation of polycrystalline diamond as a function of microstructure. *Engineering Fracture Mechanics*, 2015.

[56] D. McNamara, P. Alveen, D. Carolan, N. Murphy, and A. Ivanković. Numerical analysis of the strength of polycrystalline diamond as a function of microstructure. *International Journal of Refractory Metals and Hard Materials*, 52:195–202, 2015.

[57] M P Hitchiner, E M Wilks, and J Wilks. The polishing of diamond and diamond composite materials. *Wear*, 94:103–120, 1984.

[58] E A Almond and N J McCormick. Edge flaking of brittle materials. *J. Hard Mater.*, 1:25–51, 1990.

[59] E Zaayman. *The fracture of diamond*. PhD thesis, University of Cambridge, 2007.

[60] E Zaayman, G Morrison, and J E Field. Edge flaking in diamond. *Int. J. Refract. Metals Hard Mater.*, 27:409–416, 2009.

[61] M P D'Eveyln and K Zgonc. Elastic properties of polycrystalline cubic boron nitride and diamond by dynamic resonance measurements. *Diamond & Related Materials*, 6:812–816, 1997.

[62] F.G. Marro, A. Mestra, E. Jiménez-Piqué, S. Ozbayraktar, and L. Llanes. Damage induced by monotonic and cyclic spherical indentation in polycrystalline diamond (PCD). *International Journal of Refractory Metals and Hard Materials*, 49:292–301, mar 2015.

[63] F. García-Marro, A. Mestra, V. Kanyanta, K. Maweja, S. Ozbayraktar, and L. Llanes. Contact damage and residual strength in polycrystalline diamond (PCD). *Diamond and Related Materials*, 65, 2016.

[64] Yongfang Zhang, Zili Kou, Yongjun Li, Jian Zhang, Jiaqian Qin, and Leiming Fang. High pressure and high temperature sintering of fine-grained PCD using bi-layered assembly. *High Pressure Research*, 29(2):325–334, jun 2009.

[65] Amanda McKie, Mathias Herrmann, Iakovos Sigalas, Kerstin Sempf, and Roger Nilen. Suppression of abnormal grain growth in fine grained polycrystalline diamond materials (PCD). *International Journal of Refractory Metals and Hard Materials*, 41:66–72, 2013.

[66] T-J Shin, J-O Oh, K H Oh, and D N Lee. The mechanism of abnormal grain growth in polycrystalline diamond during high pressure-high temperature sintering. *Diamond & Related Materials*, 13:488–494, 2004.

[67] D Belnap and A Griffo. Homogeneous and structured PCD/WC-Co materials for drilling. *Diamond & Related Materials*, 13:1914–1922, 2004.

[68] L E Hibbs Jr. and M Lee. Some aspects of the wear of polycrystalline diamond tools in rock removal processes. *Wear*, 46:141–147, 1978.

[69] P Philbin and S Gordon. Characterisation of the wear behaviour of polycrystalline diamond (PCD) tools when machining wood based composites. *J. Mater. Process. Technol.*, 162-163:665–672, 2005.

[70] Hugo L.S. Monteiro and Marcelo A. Trindade. Performance analysis of proportional-integral feedback control for the reduction of stick-slip-induced torsional vibrations in oil well drillstrings. *Journal of Sound and Vibration*, 398:28–38, 2017.

[71] J E Westraadt, I Sigalas, and J H Neethling. Characterisation of thermally degraded polycrystalline diamond. *Int. J. Refract. Metals Hard Mater.*, 48:286–292, 2015.

[72] M Petrovic, A Ivankovic, and N Murphy. The mechanical properties of polycrystalline diamond as a function of strain rate and temperature. *J. Eur. Ceram. Soc.*, 32:3021–3027, 2012.

[73] F M Shakhov and S V Kidalov. Effect of fullerenes on the activation energy of the graphite-diamond phase transition. *Phys. Solid State*, 56:1622–1625, 2014.

[74] G Zhan, A Patin, R Pillai, R Gilleylen, and M Castagna. In-Situ Analysis of the Microscopic Thermal Fracture Behaviour of PDC Cutters using Environmental Scanning Electron Microscope. In *Paper prepared for IADC/SPE Drilling Conference and Exhibition held in Fort Worth, Texas, USA*. IADC/SPE, 2014.

[75] P F Gigl. The strength of polycrystalline diamond compacts. In K D Timmerhaus and M S Barber, editors, *High-Pressure Science and Technology. 1: Physical Properties and Material Synthesis*, pages 914–922. Plenum Press, New York, 1979.

[76] D R Andrews. *The Erosion of Metals*. PhD thesis, Cambridge University, Cambridge, UK, 1980.

[77] Standard Test Method for Conducting Erosion Tests by Solid Particle Impingement Using Gas Jets, G76-07. *ASTM International*.

[78] R H Telling, G.H. Jilbert, and J E Field. Erosion of aerospace materials by solid-particle impact. In *SPIE 3060*, 1997.

[79] U. Schumann, B. Weinzierl, O. Reitebuch, H. Schlager, A. Minikin, C. Forster, R. Baumann, T. Sailer, K. Graf, H. Mannstein, C. Voigt, S. Rahm, R. Simmet, M. Scheibe, M. Lichtenstern, P. Stock, H. Rüba, D. Schäuble, A. Tafferner, M. Rautenhaus, T. Gerz, H. Ziereis, M. Krautstrunk, C. Mallaun, J.-F. Gayet, K. Lieke, K. Kandler, M. Ebert, S. Weinbruch, A. Stohl, J. Gasteiger, S. Groß, V. Freudenthaler, M. Wiegner, A. Ansmann, M. Tesche, H. Olafsson, and K. Sturm. Airborne observations of the Eyjafjalla volcano ash cloud over Europe during air space closure in April and May 2010. *Atmospheric Chemistry and Physics*, 11(5):2245–2279, mar 2011.

[80] A T Fry, N Lovelock, M Smith, M Gee, and A J Gant. An Innovative High Temperature Solid Particulate Erosion Testing System. *Wear*, 376-377:458–467, 2017.

[81] Stephen M Walley. *Erosion of polyethylene by solid particle impact*. PhD thesis, Cambridge University, 1983.

[82] H Nomoto. Solid particle erosion analysis and protection design for steam turbines. In Tanuma Tadashi, editor, *Advances in Steam Turbines for Modern Power Plants*, chapter 10, pages 219–239. Woodhead Publishing, 2017.

[83] Brian Lawn. *Fracture of Brittle Solids*. Cambridge University Press, Cambridge, UK, second edi edition, 1993.

[84] H H Hertz. *Hertz's Miscellaneous Papers*. Macmillan, London, 1896.

[85] E H Yoffe. Modified Hertz theory for spherical indentation. *Philosophical Magazine A*, 50(6):813–828, 1984.

[86] B R Lawn, S M Wiederhorn, and D E Roberts. Effect of sliding friction forces on the strength of brittle materials. *Journal of Materials Science*, 19:2561–2569, 1984.

[87] M. Munawar Chaudhri and Chen Liangyi. The orientation of the Hertzian cone crack in soda-lime glass formed by oblique dynamic and quasi-static loading with a hard sphere. *Journal of Materials Science*, 24(10):3441–3448, oct 1989.

[88] L. Ceseracciu, M. Anglada, and E. Jiménez-Piqué. Hertzian cone crack propagation on polycrystalline materials: Role of R-curve and residual stresses. *Acta Materialia*, 56(2):265–273, jan 2008.

[89] Bruno A Latella, Brian H O'connor, Nitin P Padture, and Brian R Lawn. Hertzian Contact Damage in Porous Alumina Ceramics. *J. Am. Ceram. Soc*, pages 80–84, 1997.

[90] Brian R Lawn. Indentation of Ceramics with Spheres: A Century after Hertz. *J. Am. Ceram. Soc*, 81(8):1977–94, 1998.

[91] H.C. Meng and K.C. Ludema. Wear models and predictive equations: their form and content. *Wear*, 181-183:443–457, mar 1995.

[92] Etienne Bousser, Ludvik Martinu, and Jolanta E. Klemberg-Sapieha. Solid particle erosion mechanisms of hard protective coatings. *Surface and Coatings Technology*, 235:383–393, nov 2013.

[93] S Johansson, F Ericson, and J Schweitz. Solid Particle Erosion - A Statistical Method for Evaluation of Strength Properties of Semiconducting Materials. *Wear*, 115:107–120, 1987.

[94] S M Wiederhorn and B J Hockey. Effect of material parameters on the erosion resistance of brittle materials. *J. Mater. Sci.*, 18:766–780, 1983.

[95] Iain Finnie. Erosion of surfaces by solid particles. *Wear*, 3:87–103, 1960.

[96] Iain Finnie. Some reflections on the past and future of erosion. *Wear*, 186-187:1–10, jul 1995.

[97] Ya Zhang, Guang Pan, Yonghao Zhang, and Sina Haeri. A multi-physics peridynamics-DEM-IB-CLBM framework for the prediction of erosive impact of solid particles in viscous fluids. *Computer Methods in Applied Mechanics and Engineering*, 352:675–690, aug 2019.

[98] M. S. ElTobgy, E. Ng, and M. A. Elbestawi. Finite element modeling of erosive wear. *International Journal of Machine Tools and Manufacture*, 45(11):1337–1346, 2005.

[99] Yu Fei Wang and Zhen Guo Yang. Finite element model of erosive wear on ductile and brittle materials. *Wear*, 265(5-6):871–878, 2008.

[100] Maksim Antonov, Jüri Pirso, Ahto Vallikivi, Dmitri Goljandin, and Irina Hussainova. The effect of fine erodent retained on the surface during erosion of metals, ceramics, plastic, rubber and hardmetal. *Wear*, 354-355:53–68, 2016.

[101] Vahid Hadavi, Carlos E. Moreno, and Marcello Papini. Numerical and experimental analysis of particle fracture during solid particle erosion, part I: Modeling and experimental verification. *Wear*, 356-357:135–145, 2016.

[102] Vahid Hadavi, Carlos E. Moreno, and Marcello Papini. Numerical and experimental analysis of particle fracture during solid particle erosion, Part II: Effect of incident angle, velocity and abrasive size. *Wear*, 356-357:146–157, 2016.

[103] G W Stachowiak and A W Batchelor. Abrasive, Erosive and Cavitation Wear. In *Engineering Tribology*, pages 501–551. 2005.

[104] Toyohisa Yamamoto, Mikael Olsson, and Sture Hogmark. Three-body abrasive wear of ceramic materials. *Wear*, 174(1-2):21–31, 1994.

[105] J. A. Williams. The laboratory simulation of abrasive wear. *Tribotest*, 3(3):267–306, 1997.

[106] A J Gant and M G Gee. Structure–property relationships in liquid jet erosion of tungsten carbide hardmetals. *International Journal of Refractory Metals and Hard Materials*, 27:332–343.

[107] Ian M. Hutchings. Ductile-brittle transitions and wear maps for the erosion and abrasion of brittle materials. *Journal of Physics D: Applied Physics*, 25(1):A212–A221, 1992.

[108] S. Wada. Effects of Hardness and Fracture Toughness of Target Materials and Impact Particles on Erosion of Ceramic Materials. *Key Engineering Materials*, 71:51–74, 1992.

[109] I P Hayward and J E Field. The solid particle erosion of diamond. *J. Hard Mater.*, 1:53–64, 1990.

[110] R H Telling. *The fracture of natural and synthetic diamond*. PhD thesis, University of Cambridge, 1999.

[111] D W Wheeler and R J K Wood. Erosive wear behaviour of thick chemical vapour deposited diamond coatings. *Wear*, 225-229:523–536, 1999.

[112] D W Wheeler and R J K Wood. The erosion of CVD diamond by diamond particles. *Philos. Mag. Letts*, 85:367–375, 2005.

[113] D.W. Wheeler and R.J.K. Wood. High velocity erosion of CVD diamond coatings by diamond particles. *Diamond and Related Materials*, 84:32–40, apr 2018.

[114] A R Davies. *The Solid Particle Erosion of Free-Standing CVD Diamond*. Phd, University of Cambridge, 2002.

[115] B D Ramsay. MPhil Thesis. *The mechanical properties of single crystal diamond*, 2015.

[116] I P Hayward. *Friction and strength properties of diamond*. PhD thesis, 1987.

[117] Z Feng and J E Field. Solid particle erosion of diamond, a polycrystalline diamond composite and a polycrystalline boron nitride composite. *J. Hard Mater.*, 1:273–287, 1991.

[118] P L Kaye and J E Field. Solid particle erosion of a stainless steel, tungsten carbide and a polycrystalline diamond composite. *J. Hard Mater.*, 4:167–175, 1993.

[119] P L Kaye. *The Erosive Cleaning of Surfaces*. PhD thesis, University of Cambridge, 1995.

[120] I M Scullion. *Erosion by Solid Particle Impact*. Phd thesis, University of Cambridge, 1987.

[121] J K Patterson and A V Levy. Methods for characterization of erosion by gas-entrained solid particles. *Wear*, 91:333–347, 1983.

[122] S Srinivasan and R O Scattergood. Effect of Erodent Hardness on Erosion of Brittle Materials. *Wear*, 128:139–152, 1988.

[123] N Dalili, A Edrisy, and R Carriveau. A Review of Surface Engineering Issues Critical to Wind Turbine Performance. *Renewable and Sustainable Energy Reveiws*, 13:428–438, 2007.

[124] Guangxian Li, Shuang Yi, Shoujin Sun, and Songlin Ding. Wear mechanisms and performance of abrasively ground polycrystalline diamond tools of different diamond grains in machining titanium alloy. *Journal of Manufacturing Processes*, 29:320–331, oct 2017.

[125] K Weinert, D Biermann, and D Meister. Machining of Metal Matrix Composites - Tool Wear and Surface Integrity. In *ICCM-10, Whistler, B.C., Canada*, page 589.

[126] D. Miess and G. Rai. Fracture toughness and thermal resistance of polycrystalline diamond compacts. *Materials Science and Engineering: A*, 209:270–276, 1996.

[127] A R Davies and J E Field. Damage mechanism involved in the solid particle erosion of CVD diamond. *Proc. SPIE*, 4375:171–179, 2001.

[128] H Wensink and M C Elwenspoek. A closer look at the ductile–brittle transition in solid particle erosion. *Wear*, 253:1035–1043, 2002.

[129] G P Tilly. A two-stage mechanism of ductile erosion. *Wear*, 23:87–96, 1973.

[130] L Lapides and A Levy. The halo effect in jet impingement solid particle erosion testing of ductile materials. *Wear*, 58:301–311, 1980.

[131] D B Marshall, A G Evans, M E Gulden, J L Routbort, and R O Scattergood. Particle size distribution effects on the solid particle erosion of brittle materials. *Wear*, 71:363–373, 1981.

[132] A J Gant and M G Gee. Wear modes in slurry jet erosion of tungsten carbide hardmetals: Their relationship with microstructure and mechanical properties. *International Journal of Refractory Metals and Hard Materials*, 49(1):192–202, mar 2015.

[133] R Mark Bradley and James M E Harper. Theory of ripple topography induced by ion bombardment. *Citation: Journal of Vacuum Science & Technology A*, 6:2390, 1988.

[134] I Sunagawa. Morphology of natural and synthetic diamond crystals. In I Sunagawa, editor, *Materials Science of the Earth's Interior*, pages 303–330. Terra Scientific Publishing Co, Tokyo, 1984.

[135] V P Swaminathan, J S Smith, and D W Gandy. High Temperature Solid Particle Erosion Testing Standard for Advanced Power Plant Materials and Coatings. In D Gandy and J Shingledecker, editors, *Advances in Materials Technology for Fossil Power Plants*, pages 382–399, Waikoloa, Hawaii, USA, 2013.

[136] S Agarwal and A H Howes. Erosion/corrosion of materials in high-temperature environments. In *Proc. AIME Conf. on High Temperature Corrosion in Energy Systmes*, Detroit, MI, 1984. Metallurgical Society of AIME, Warrendale, PA, 1985.

[137] V Nagarajan and I G Wright. Influcence of oxide scales on high temperature corrosion-erosion behaviour of alloys. In *Proc. NACE Conf. On High tempreature corrosion*, pages 398–405, San Diego, CA, 1981. National Association of Corrosion Engineers, Houston, TX, 1983.

[138] Alan V. Levy, Johnny Yan, and Jennifer Patterson. Elevated temperature erosion of steels. *Wear*, 108:43–60, 1986.

[139] A.F. Colclough and J.A. Yeomans. Hard particle erosion of silicon carbide and silicon carbide-titanium diboride from room temperature to 1000 °C. *Wear*, 209(1-2):229–236, aug 1997.

[140] A.L Ham, J.A Yeomans, and J.F Watts. Effect of temperature and particle velocity on the erosion of a silicon carbide continuous fibre reinforced calcium aluminosilicate glass–ceramic matrix composite. *Wear*, 233-235:237–245, dec 1999.

[141] D.E. Alman, J.H. Tylczak, J.A. Hawk, and J.H. Schneibel. An assessment of the erosion resistance of iron-aluminide cermets at room and elevated temperatures. *Materials Science and Engineering: A*, 329-331:602–609, jun 2002.

[142] C-B. Wang, J Shi, Z-R. Geng, and J-Y. Zhang. Role of surface hydrogen bonds in determing the friction behaviors of hydrogenated diamond-like carbon films. *Chinese Phys. Letts*, 29:56201, 2012.

[143] X Li, H Ding, Z Huang, M Fang, B Liu, Y Liu, X Wu, and S Chen. Solid particle erosion-wear behavior of SiC–Si3N4 composite ceramic at elevated temperature. *Ceramics International*, 40(10):16201–16207, dec 2014.

[144] Jing Zhou Yang, Ming Hao Fang, Zhao Hui Huang, Xiao Zhi Hu, Yan Gai Liu, Hao Ran Sun, Jun Tong Huang, and Xiao Chao Li. Solid particle impact erosion of alumina-based refractories at elevated temperatures. *Journal of the European Ceramic Society*, 2012.

[145] Xiaojun Wang, Minghao Fang, Lai Chang Zhang, Hao Ding, Yan Gai Liu, Zhaohui Huang, Shaoping Huang, and Jingzhou Yang. Solid particle erosion of alumina ceramics at elevated temperature. *Materials Chemistry and Physics*, 2013.

[146] A. W. Ruff and L. K. Ives. Measurement of solid particle velocity in erosive wear. *Wear*, 35(1):195–199, 1975.

[147] Standard Test Method for Conducting Elevated Temperature Erosion Tests by Solid Particle Impingement Using Gas Jets, G211 - 14. *ASTM International*, 2014.

[148] A T Fry, M G Gee, S Clausen, U Neuschaefer-Rube, M Bartscher, D Spaltmann, M Woydt, S Radek, F Cernuschi, J R Nicholls, and T W Rose. Metrology to Enable High Temperature Erosion Testing - A New European Initiative. In *Advances in Materials Technology for Fossil Power Plants2*, pages 400–411, 2013.

[149] I M Hutchings. Solid Particle Erosive Wear Testing. *ASTM Handbook*, 8:338–345, 2000.

[150] N. A.S. Smith, A. T. Fry, L. E. Crocker, F. Cernuschi, and L. Lorenzoni. Design and optimisation of the nozzle of an innovative high temperature solid particulate erosion testing system using finite element modelling. *Applied Mathematics and Computation*, 301:60–69, may 2017.

[151] J J Kopanski. Oxidation of SiC. In G L Harris, editor, *Properties of Silicon Carbide*, pages 121–129. INSPEC, the Institution of Electrical Engineers, London, 1995.

[152] Geoffrey H. Campbell, Brian J. Dalgleish, and Anthony G. Evans. Brittle-to-Ductile Transition in Silicon Carbide. *Journal of the American Ceramic Society*, 72(8):1402–1408, aug 1989.

[153] C Holstein-Rathlou, H.P.Gunnlaugsson, J Merrison, P.Taylor, C Lange, J Davis, and M Lemmon. Winds at the Mars Phoenix landing site. In *40th Lunar and Planetary Science Conference*, pages 3–4, 2009.

[154] Jonathan Merrison, Line Drube, Haraldur Gunnlaugsson, Christina Holstein-Rathlou, Svend Knak Jensen, Jon Mason, Morten Bo Madsen, Per Nørnberg, and Manish Patel. Research Using the European Mars Simulation Wind Tunnel Facility. In *Geophysical Research Abstracts*, volume 13, page 2972, 2011.

[155] C Holstein-Rathlou, J Merrison, J J Iversen, A B Jakobsen, R Nicolajsen, P Nørnberg, K Rasmussen, A Merlone, G Lopardo, T Hudson, D Banfield, and G Portyankina. An Environmental Wind Tunnel Facility for Testing Meteorological Sensor Systems. *Journal of Atmospheric and Oceanic Technology*, 31(February):447–457, 2014.

[156] H.M. Slot, E.R.M. Gelinck, C. Rentrop, and E. van der Heide. Leading edge erosion of coated wind turbine blades: Review of coating life models. *Renewable Energy*, 80:837–848, aug 2015.

[157] L Bartolome and J Teuwen. Prospective challenges in the experimentation of the rain erosion on the leading edge of wind turbine blades. *Wind Energy*, 22:140–151, 2019.

[158] Yuanxin Zhou, Vijay Rangari, Hassan Mahfuz, Shaik Jeelani, and P K Mallick. Experimental study on thermal and mechanical behavior of polypropylene, talc/polypropylene and polypropylene/clay nanocomposites. *Materials Science and Engineering A*, 402:109–117, 2005.

[159] J. A. Sauer and G. C. Richardson. Fatigue of polymers. *International Journal of Fracture*, 16(6):499–532, dec 1980.

[160] Christopher Swarctz, Elias Aljallis, Scott Hunter, John Simpson, and Chang-Hwan Choi. Characterization of Superhydrophobic Surfaces for Anti-Icing in a Low-Temperature Wind Tunnel. In *Volume 7: Fluid Flow, Heat Transfer and Thermal Systems, Parts A and B*, pages 303–306. ASME, jan 2010.

[161] Robert M Hall and Edward J Ray. Investigation of Minimum Operating Temperatures for Cryogenic Wind Tunnels. *J. AIRCRAFT*, 14(6), 1977.

[162] Kamel Al-Khalil, Eddie Irani, and Dean Miller. Mixed-Phase Icing Simulation and Testing at the Cox Icing Wind Tunnel. In *41st Aerospace Sciences Meeting and Exhibit*, Reno, Nevada, 2003.

[163] J Pernas-Sánchez, J A Artero-Guerrero, and J A Varas. Experimental analysis of ice sphere impacts on unidirectional carbon/epoxy laminates. *International Journal of Impact Engineering*, 96:1–10, 2016.

[164] Hyonny Kim and Keith T Kedward. Modeling Hail Ice Impacts and Predicting Impact Damage Initiation in Composite Structures. *AIAA JOURNAL*, 38(7):1278–1288, 2000.

[165] Li-Lih Wang, J E Field, Q Sun, and J Liu. Surface damage of polymethylmethacrylate plates by ice and nylon ball impacts Surface damage of polyniethylmethacrylate plates by ice and nylon ball impacts. *Journal of Applied Physics*, 78:1643, 1995.

[166] J. R. Laguna-Camacho, A. Marquina-Chávez, J. V. Méndez-Méndez, M. Vite-Torres, and E. A. Gallardo-Hernández. Solid particle erosion of AISI 304, 316 and 420 stainless steels. *Wear*, 301(1-2):398–405, apr 2013.

[167] C. T. Morrison, R. O. Scattergood, and J. L. Routbort. Erosion of 304 stainless steel. *Wear*, 111(1):1–13, aug 1986.

[168] H. I. McHenry. The Properties of Austenitic Stainless Steel at Cryogenic Temperatures. In R P Reed, editor, *Austenitic Steels at Low Temperatures*, pages 1–27. Plenum Press, New York, 1983.